Selective Transport of Functional Polymer-Hybrid Vesicles into Cell Nuclei

Inauguraldissertation

zur

Erlangung der Würde eines Doktors der Philosophie

vorgelegt der

Philosophisch-Naturwissenschaftlichen Fakultät

der Universität Basel

von

Christina Zelmer

aus Magdeburg, Deutschland

Basel, 2021

Genehmigt von der Philosophisch-Naturwissenschaftlichen Fakultät

auf Antrag von

Prof. Dr. Roderick Lim

Prof. Dr. Cornelia Palivan

Prof. Dr. Birthe Fahrenkrog

Basel, den 19. November 2019

Prof. Dr. Martin Spiess

Dekan

Acknowledgements

First, I want to thank my supervisors Prof. Lim and Prof. Palivan for this very interesting and interdisciplinary PhD topic. Also, Prof. Fahrenkrog was part of the dissertation defense committee and I want to thank Prof. Spiess for hosting the defense.

I am very grateful to Dr. Larisa Kapinos-Schneider for her steady motivations, all her brilliant scientific insights and her support in the wet-lab. Especially, I want to thank Dr. Ludovit Zweifel for his support during the preparation of this Thesis and for many discussions that have been essential for the results of this work. Dr. Adrian Dinu I want to thank for patiently teaching me the triblock copolymer synthesis. Also, I thank my former master student Nathalia Münch for her great work and nice collaboration.

Moreover, I am very thankful to Dr. Timothy Sharp for spending his valuable time proofreading the Thesis. His input has been important to shape and specify this work. In this light, I would like to thank Dr. Ludovit Zweifel, Dr. Elena Kassianidou and Dr. Ioana Craciun for proofreading.

I am grateful to the former and the present group members of the Lim and the Palivan Lab, namely to Dr. Suncica Barbato, Dr. Ludovit Zweifel, Viktoria Mikhalevich, Myrto Kyropoulou, Joanna Kalita and Dr. Elena Kassianidou, to mention here only a few. Thanks for a fantastic work atmosphere, countless coffee breaks and great help and discussions over the past years.

For the supply with state-of-the-art analytical instruments and excellent apprenticing of those I would like to thank Dr. Kai Schleicher, Dr. Wolf Heusermann

and Nikolaus Ehrenfeuchter from the Imaging Core Facility, Dr. Timothy Sharp and Dr. Ludovit Zweifel from the Biophysics Facility and Dr. Markus Dürrenberger and Susanne Erpel from the Nano Imaging Lab.

I further want to thank the Swiss Nanoscience Institute (SNI) for the PhD fellowship I was privileged to hold for four years of my PhD. The SNI annual meetings in Lenzerheide and the annual `Nano in the Snow` winter schools have been highlights during my affiliation to the SNI doctoral school.

Last but most important, I want to thank my family and friends for their support and patience. Especially I want to thank my parents Sylvia and Michael, my sister Conny, my partner and best friend Lajko and our little daughter Lena Victoria.

Table of Contents

List of Figures

List of Tables

Abstract

The cell nucleus is the ultimate target for many therapeutic treatments including cancer, brain disorders and heart dysfunction. Therefore, organelle-specific nanocarriers (NCs) are highly sought after for delivering sufficient concentrations of the active therapeutic agent *in situ.* This requires the NCs to interact with the nucleocytoplasmic transport (NCT) to enter nuclear pore complexes (NPCs). Yet, little is known as to how NCs infiltrate this vital intracellular barrier to enter the nuclear interior. Furthermore, it is poorly understood how the physico-chemical NC properties influence this process.

Here, ~50 nm-sized synthetic NCs were developed based on polymer-hybrid vesicles, known as polymersomes. Following a bottom-up approach, biocompatible and amphiphilic PMOXA-PDMS-PMOXA triblock copolymers were self-assembled into NCs and surface-conjugated with nuclear localization sequences (NLS). Those NLS-NCs represent ideal candidates to study NCT, as they remain structurally intact during nuclear import due to the enhanced polymersome membrane stability and strength as compared to liposomes [1, 2]. Moreover, the NLS surface tags authenticate NCs as nucleus specific and enable the NCT mediated import. Applying a so-called film rehydration method permits encapsulating the hydrophilic model drug Ruthenium Red inside the aqueous vesicle cavity and post-treatment with Bodipy 630/650 allows intercalating a lipophilic model drug into the membrane of the same NC (see Abstract Figure). The encapsulated drugs are consequently protected against premature degradation and carried together to the nucleus.

In addition, NLS-NCs were used as large cargoes to study NCT mechanisms. Detailed chemical, biophysical and cellular analysis show that karyopherin receptors (Kaps) are required to bind and escort NLS-NCs through NPCs while Ran

guanosine triphosphate (RanGTP) promotes their release from NPCs into the nuclear interior. Ultrastructural analysis by transmission electron microscopy further resolves NLS-NCs on transit in NPCs and inside the nucleus. By elucidating their ability to utilize NCT, these findings demonstrate the efficacy of polymersomes to deliver encapsulated payloads directly into cell nuclei.

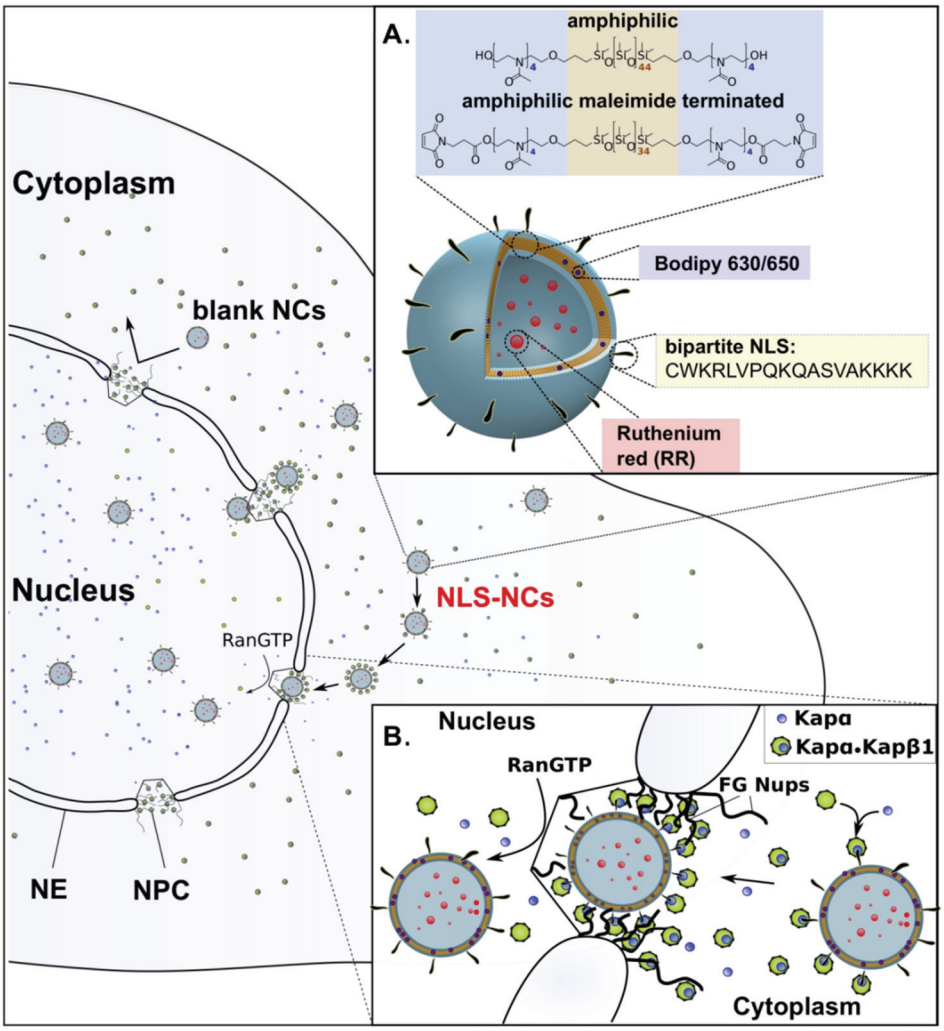

Abstract Figure. Targeting polymersome nanocarriers (NCs) into the cell nucleus. A. NLS-NCs self-assemble from amphiphilic PMOXA-PDMS-PMOXA triblock copolymers. Two model compounds are used to test nuclear delivery; Ruthenium Red (RR) is encapsulated within the NLS-NC lumen, and Bodipy 630/650 is inserted into the membrane. **B.** The nuclear transport mechanism involves Kapα•Kapβ1 that (i) authenticates NLS-NCs for selective NPC transport, (ii) binds to FG Nups, and (iii) releases NLS-NCs into the nucleus upon binding RanGTP.

Chapter 1

Introduction

Parts of this chapter have been published as

Vujica, S., Zelmer, C., Panatala R., Lim, R. Y. H. Nucleocytoplasmic transport: a paradigm for molecular logistics in artificial systems. *CHIMIA International Journal for Chemistry* **70** (6), 413-417 (2016) [3].

Mikhalevich, V., Zelmer, C., Car, A., Palivan, C. G. Bio-inspired Polymer Membranes, in Bio-inspired Polymers. *Royal Society of Chemistry,* 221-258 (2016) [4].

1 Introduction

1.1 Nucleocytoplasmic transport (partially reproduced from [3])

The cell nucleus is the largest organelle in eukaryotic cells. It contains most of the genetic material and isolates it from the cytoplasm by two bilayer lipid membranes, known as the nuclear envelope (NE) [5]. Due to this spatial segregation, genome transcription, which proceeds in the cell nucleus, is protected against exogenous causes like premature chemical modification or enzymatic degradation. Complementary gene translation takes place in the cytoplasm containing ribosomes [6]. Both compartments, the cytoplasm and the nucleoplasm, are essentially connected with one another by proteinaceous NPCs [7]. These pores mediate the NCT of various cargoes such as transcription factors or mRNAs [8, 9]. The NCT through 50 – 100 nm wide NPC channels [10, 11] is bidirectional [12]. It permits the diffusion of ions, metabolites and proteins smaller than ∼5 nm in size or ∼40 kDa in weight [13]. However, nuclei specific cargoes larger than that use active NCT mechanisms and recruit nuclear transport receptors (NTRs or Kaps) to cross the NPC [14, 15]. This process is based on multivalent biochemical binding interactions and results in cargo dwell times of ∼5 ms [16] and translocation rates of ∼1 kHz [17]. NPCs are thereby capable of simultaneously accommodating and translocating multiple cargoes through a single pore based on highly parallelized NCT mechanisms. Hence, specific cargoes accumulate orders of magnitude faster in the nucleus than passively diffusing molecules and do so even against prevailing concentration gradients [18].

In the cellular milieu, nuclear import specificity is granted to cargo compounds through highly positively charged peptide NLSs (NLS-cargo). In this regard, specific cargoes are being recognized by their complementary Kaps and

sorted from unspecific compounds for subsequent delivery to the desired spatial location [12, 19, 20].

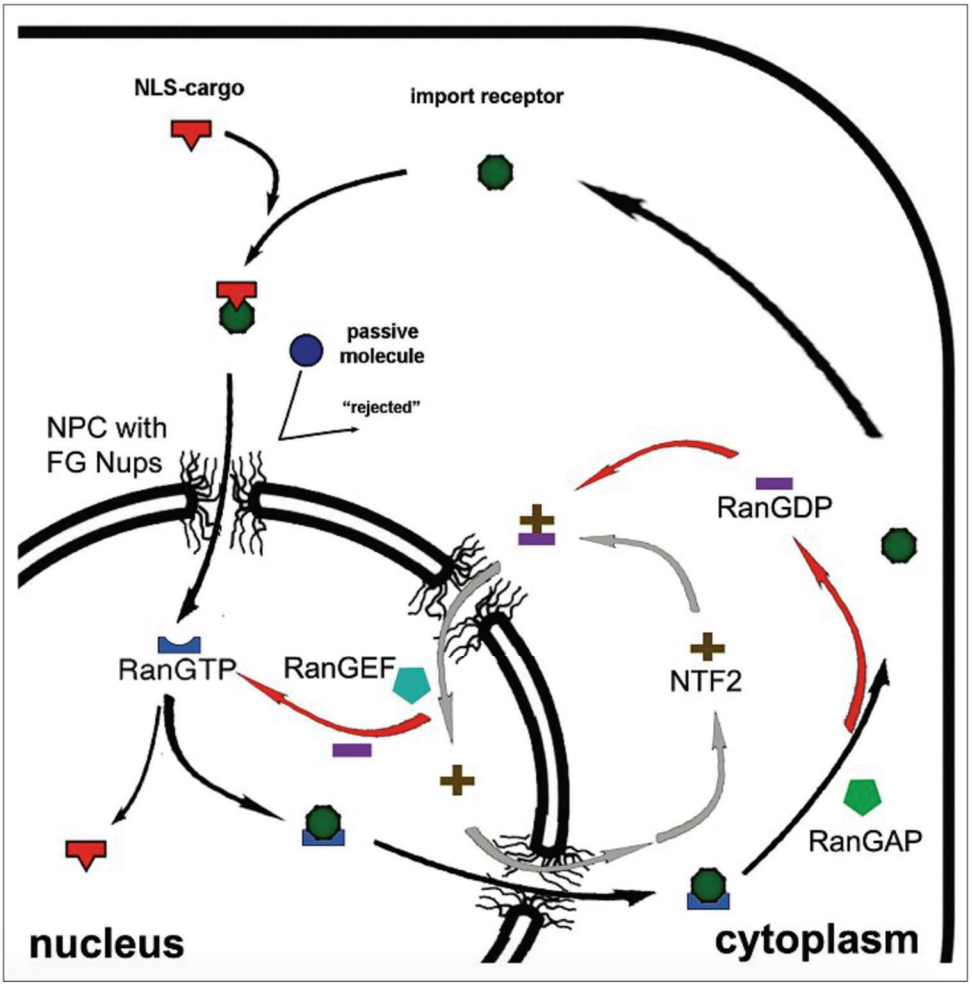

Figure 1.1 Schematic overview of the nucleocytoplasmic transport. NLS-cargoes are recognized by specific import receptors and shuttled from the cytoplasm into nuclear pore complexes (NPCs). At the nucleoplasmic NPC side, RanGTP disassembles the transient cargo•receptor complex and releases the cargo irreversibly into the nucleus. A parallel Ran cycle regenerates the import receptor for the next round of import. Reproduced from Vujica, Zelmer and Lim (2016) [3].

Loaded Kaps ferry their specific cargo across the central NPC channel in an energy-independent equilibrium [21-23]. This process however requires an energy supply beyond k_BT in order to impart transport directionality and to terminate cargo import [24]. Here, the final nuclear uptake is regulated by the small Ras-related nuclear protein Ran. In the GTP on-bound form, RanGTP binds with

high avidity to the NPC transient cargo•Kap complexes to dissociate them irreversibly. By doing so, the cargo is released into the nucleus and a new RanGTP•Kap complex formed (see

Figure **1.1**).

In the same manner as nuclei destined biomacromolecules, it is assumed that the synthetic NCs developed in this Thesis work are employing NCT mechanisms for their nuclear import. Towards this end, biochemical details about the NCT mechanistic steps and *modi operandi* underlying the nuclear import of large cargoes are outlined in the following sections:

- Cargo recognition by specific Kaps (Thesis section 1.1.1)
- Cargo translocation across NPCs (Thesis section 1.1.2)
- RanGTP catalyzed cargo release into cell nuclei (Thesis section 1.1.3)
- Kap regeneration (Thesis section 1.1.4)

1.1.1 Kaps and cargo recognition mechanisms

Several transport mechanisms have been identified to facilitate the nucleocytoplasmic exchange of biomacromolecules [12]. Central to these processes are Kaps (soluble transport receptors also termed as importins and exportins), that are mediating the nuclear import and export of cargo proteins [6] and the nuclear export of cargo ribonucleic acid (RNA) or ribonucleoprotein particles (RNPs) [25].

Kap receptors are categorized into a discrete family of evolutionary conserved proteins. Despite their low sequence identity (~ 20 %), all Kaps are characterized by similar molecular weights (95 - 145 kDa), isoelectric points (4 – 5) and commonly consist of ~ 20 helix-loop-helix-motives (HEAT repeats) [26-28]. So far, 14 different Kaps have been identified in yeast and 20 different ones in mammalian cells [29, 30]. Given the limited number of Kaps and the vast number of biomacromolecules that are trafficked across NPC channels, it is expected that most Kaps function as transporters for various cargoes.

The best characterized NCT mechanism is the nuclear import of NLS-cargoes by their specific receptor Karyopherinβ1 (Kapβ1; also known as Importinβ1 or Impβ1, 98 kDa). Kapβ1 transports a broad range of NLS-conjugated proteins and binds them either directly or extends the library of importable NLS-cargoes by the usage of the adaptor molecule Karyopherinα (Kapα, Importinα or Impα, 58 kDa) [28, 31]. Biochemical details of Kapα/β1 heterodimer binding to cargo molecules have been investigated based on selected transport complex crystal structures [32, 33]. Specifically, Kapα was determined to encode a short N-terminal importin-β-binding (IBB) domain and a longer NLS-binding domain, both connected by a flexible linker [34]. The basic IBB domain functions as nuclear targeting signal and exerts a strong binding affinity towards Kapβ1 (K_D = 210 nM equilibrium dissociation constant as determined by isothermal titration calorimetry [35, 36]). Moreover, the IBB domain exhibits an autoinhibitory activity by folding back and masking the NLS binding domain to prevent premature cargo association. Structural investigations of Kapβ1 revealed a characteristic alpha-solenoid fold composed of 19 HEAT repeats. The apparent configuration stems from the ability of Kapβ1 to adopt its interaction interface according to the transported cargo compound.

One of the possible structural conformation that Kapβ1 can take up is depicted in Figure 1.2 A for the heterodimer complex with Kapα . The IBB binding pocket is located at the C-terminus of Kapβ1 and the HEAT repeats are intimately wrapped around the Kapα binding site. Here, 13 of the 19 HEATs are involved in the Kapα/β1 formation [28]. Once complexed, Kapα exerts amplified binding towards NLS-cargoes ($K_D \approx 10^{-8}$ M) [28]. The so formed NLS-cargo•Kapα/β1 transport complex is eventually able to cross the NE by multivalent interactions of Kapβ1 with the NPC.

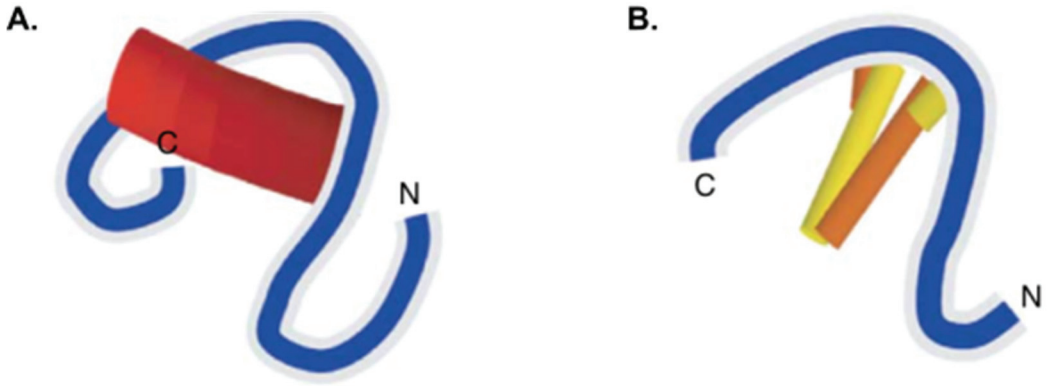

Figure 1.2 Kapβ1 bends its global structure to firmly accommodate different cargo molecules. Selected examples of transport complexes are shown for **A.** Kapβ1 (dark blue) bound to the IBB fragment of Kapα (red) and **B.** Kapβ1 bound to SREBP-2 (orange and yellow). Figure reproduced and modified from Mosammaparast and Pemberton (2004) [26].

In another example, Kapβ1 binds selectively to the transcription factor SREBP-2 (sterol regulatory element-binding protein 2, see Figure 1.2 B). SREBP-2 is a nucleus-destined cargo that is transported by means of direct Kapβ1 binding. Upon cargo recognition, Kapβ1 changes its conformation to a pseudo-twofold symmetry that firmly accommodates the symmetric SREBP-2 dimer between HEAT repeat 7 and 17 [33]. This requires however a structural transition from open and flexible to closed and more rigid [37, 38]. Several more complex crystal structures have been reported, emphasizing the conformational plasticity of Kapβ1 [32].

That Kap receptors can recognize different cargo molecules based on adaptable biochemical binding interactions and transport complex configurations, implies that their function goes beyond being simple NCT vehicles. Indeed, Kaps are essential factors for the up- and downregulation of transport rates of competing cargo entities [5]. The regulatory function of Kaps is further supported by its ability to selectively bind Ran, IBB and FG Nups. This permits cargo•Kap complex translocation across the NPCs and warrants nuclear import termination by transport complex dissociation *via* RanGTP. Both steps are outlined in more detail in the following subchapters.

1.1.2 The nuclear pore complex

The extraordinary challenge of mediating the bidirectional NCT of essential biomacromolecules is accomplished through NPCs [7, 39]. A dense net of NPCs is scattered across the NE (*e.g.* one *Xenopus laevis* nucleus counts on average ~3500 NPCs [40], Figure 1.3 A and C [41]) and connect the cytoplasm with the nucleoplasm through their inner aqueous channels.

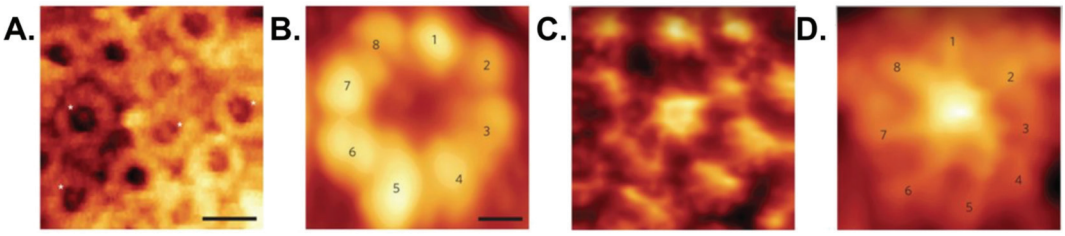

Figure 1.3 The nuclear pore complex morphology. Atomic force microscopy was used to resolve in *Xenopus laevis*:**A.** densely scattered NPCs as to see from the outer cytoplasmic NE side, **B.** an average projection of one vacant NPC composing of eight cytoplasmic filaments (numbered), **C.** a distal projection of NPCs scattered across the nucleoplasmic NE side and **D.** an average NPC structure showing the eight nuclear filaments (numbered) that fuse to the distal nuclear basket. Scale bar in A and C is 100 nm and in B and D 25 nm. Image reproduced from Sakiyama, Mazur, Kapinos and Lim (2016) [41].

NPCs are arguably the largest protein assemblies in vertebrates [42] and exhibit a considerably conserved structure and supramolecular architecture from

yeast to human. With an overall mass of app. 60 MDa in yeast or app. 120 MDa in metazoans, the NPC inner channel diameter ranges from 50 to 100 nm [10, 11, 43, 44]. Circa 30 different kinds of proteins, known as nucleoporins or short Nups, are involved in the NPC formation [45, 46]. These proteins are categorized in: 1. membrane Nups that are anchoring the NPC to the NE, 2. structural scaffold Nups and 3. intrinsically disordered Phenylalanine-Glycine rich Nups, or short FG Nups (Figure 1.4). Moreover, these Nups are arranged into three ring moieties that are forming the NPC scaffold: 1. the cytoplasmic ring and the cytoplasmic filaments, 2. the spoke ring and 3. the nucleoplasmic ring and the nuclear basket. The NPC scaffold is configured in an eight-fold rotational symmetry along the nucleocytoplasmic transport axis (see in Figure 1.3 B and D [41]) [47, 48].

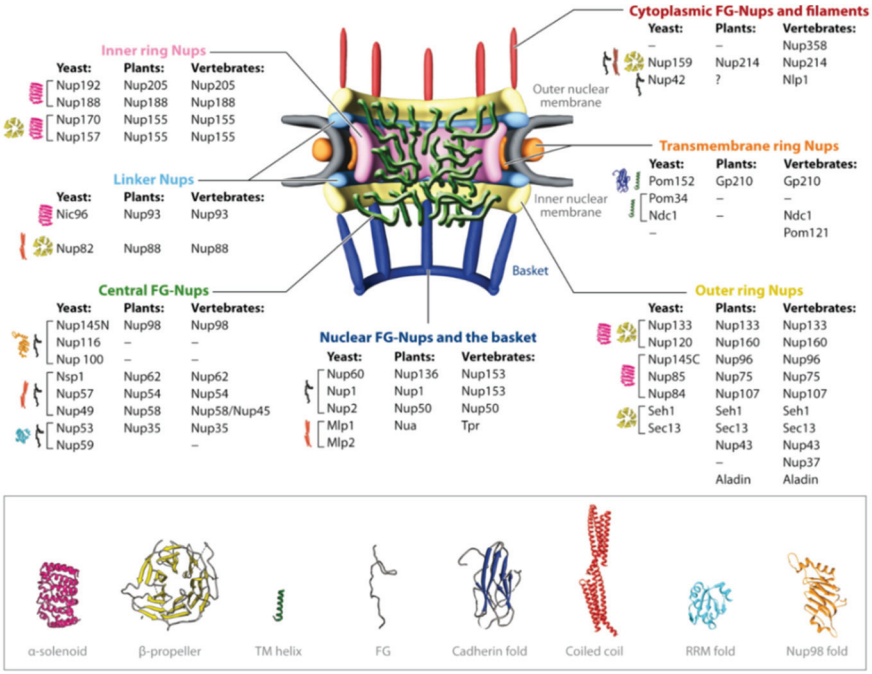

Figure 1.4 Structural arrangements and folds of nucleoporins in the NPCs. As shown on the examples of yeast, plants and vertebrates,he central FG Nups, outer ring Nups, linker Nups, inner ring Nups and transmembrane Nups form a symmetric array whereas the cytoplasmic Nups and filaments as well as the nuclear FG Nups and the basket contribute to the asymmetric parts of the NPC. Protein folds are depicted next to the Nups for yeast and described in the legend. Reproduced from Grossman, Medalia and Zwerger (2012) [49].

The overall NCT selectivity towards nucleus specific cargoes is manifested by FG Nup chains that are tethered in ~200 fold copies along the inner NPC walls [50]. Due to the absence of secondary structure, FG Nups are postulated to arrange within the pores into supramolecular hydrogel meshworks [51, 52], molecular brushes [53] or a combination thereof [54]. Based on principle size-exclusion axioms, purely diffusional NCT of molecules smaller than about 5 nm in diameter are permitted across the inner NPC channel. In contrast, the FG Nup network functions as an entropic barrier toward molecules larger than that. This barrier can only be overcome by cargo `hitchhiking` through the NPC *via* Kaps. The Kap association authenticates the cargo as nucleus specific and grants passage by numerous low-affinity interactions with the FG domains [14, 15, 55]. More specifically, single FG Nups can bind ~20 Kaps in a multispecific manner and *vice versa* Kaps themselves can bind multiple FG Nups [56]. In addition, a single transient Kap is able to bind to several FG repeats within one or multiple different Nups, resulting in highly multivalent interactions imparted with strong binding avidity [57]. Although the Kap facilitated cargo-complex movement along the NPC channel is non-directional and happens in a subdiffusional manner [58], ~100 – 500 parallel translocation events manifest to a molecular flux of up to ~80 MDa per NPC per second [17, 59].

Such high transport rates paired with the exceptional selectivity towards specific cargoes have motivated various *in vitro* studies to identify underlying NCT barrier mechanisms [17, 45, 54, 60, 61]. In brief, several models have been introduced that assume that FG Nups form a virtual gating [45, 62] or a polymer brush [53, 60]. In these scenarios, FG Nups are arranged in such a way that incoming macromolecules encounter a rapidly fluctuating entropic Nup barrier that extends away from the anchoring side due to crowding within the confined NPC channels.

The selective phase model further claims that the presence of a tightly crosslinked Nup meshwork leads to cohesive hydrophobic π-π-interactions between FG repeats that are contributing to the barrier function [51, 52]. Finally, the Forest model predicts both, cohesive and non-cohesive FG Nup regions that lead to the assembly of NPC incorporated structures [54] known as `central plugs` or `transporters` [44, 63, 64].

Despite the progress that has been made in identifying the NPC structural components and functions, it is still not completely understood how large cargoes like mRNA biomacromolecules translocate through the confined channel. It is hypothesized that NPCs behave in a diaphragm-like manner to form an entropic barrier whilst being closed and to accommodate large objects in their open configuration [11, 65]. Furthermore, large mRNA is believed to deform structurally and to translocate the NPC as a `string of beads` [66]. Cargo deformation in combination with transport mediating changes in the NPC structure is yet another possible mode of cargo transportation.

1.1.3 RanGTP mediated nuclear cargo release

NCT is unprecedented in its speed and selectivity. The overall rate of nuclear import is however limited by the NCT mechanistic cargo exit step [12]. NLS-cargo•Kapα/β1 complexes cross the NPC channels in a random walk manner [67].Yet, directionality is administered to the NCT by RanGTP. At the nucleoplasmic NPC side, RanGTP binds the transient complex and induces a conformational change that dissociates Kapβ1•RanGTP from the Kapα•NLS-cargo complex [68]. The autoinhibitory activity of the so freed IBB domain drives the dissociation of Kapα and the NLS-cargo such that both are subsequently released into the cell nucleus. In some occasions, dissociation and nuclear NLS-cargo release is additionally catalyzed by Nup50 (Figure 1.5 A) [69]. The so nuclear uptaken NLS-cargoes are irreversibly entrapped due to the exceeding NPC cut-off size unless

they are explicitly tagged for the reversing nuclear export by a nuclear export sequence (NES or NES-cargo). As consequence, NLS-cargoes can accumulate in the nucleus even against prevailing concentration gradients [70].

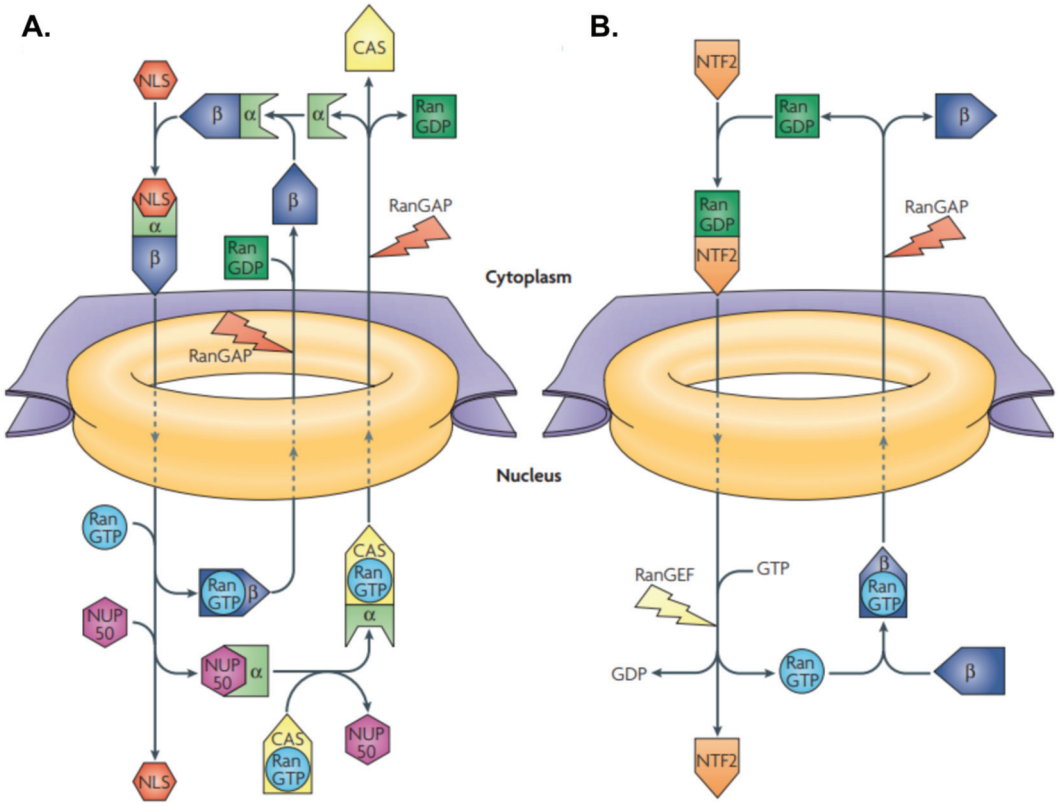

Figure 1.5 Biochemistry of nuclear import and export mechanistic steps.A. Kaps together with RanGTP are mediating a selective cargo import whilst **B**. NTF2 utilizes the parallel Ran cycle. In detail, NLS-cargo binding occurs upon Kapα complexation with Kapβ1. The resulting NLS-cargo•Kapα/β1 complex translocates through the NPC *via* Kapβ1 specific binding to FG Nups. In the nucleus, RanGTP dissociates the Kapα/β1 heterodimer and Nup50 triggers the nuclear NLS-cargo release from Kapα. The newly formed Kapβ1•RanGTP diffuses back into the cytoplasm. Meanwhile Kapα employs the nuclear export factor CAS for its export. Located within the cytoplasm, the GTPase activation protein RanGAP catalyzes the RanGTP hydrolysis to RanGDP which subsequently dissociates from Kapβ1. The RanGDP specific NTR NTF2 shuttles the protein back to the nucleus where the chromatin-bound nucleotide exchange factor RanGEF recharges it to the GTP on-bound RanGTP. Figure reproduced from Stewart (2007) [12].

1.1.4 Nuclear transport cycle and Kap regeneration

Nuclear NLS-cargo release and NES-cargo export are both dependent on a steep RanGTP gradient across the NE [70, 71]. On average, two RanGTPs are

consumed per nuclear import of one NLS-cargo and one RanGTP per nuclear export of one NES-cargo. Therefore, an efficient and continuous nuclear import and export cycle is required to maintain high RanGTP concentration in the nucleoplasm.

As discussed before, RanGTP dissociates the NLS-cargo•Kapα/β1 by outcompeting the Kapα IBB domain. The newly formed Kapβ1•RanGTP shuttles back to the cytoplasm where RanGTP is hydrolyzed, releasing thereby Kapβ1. Meanwhile, nuclear Kapα recruits the nuclear export factor CAS (standing for cellular apoptosis susceptibility gene) for its back cycling [72]. However, this complex formation can only occur in the presence of RanGTP. The so formed CAS•RanGTP•Kapα complex can then transit through the NPC back in the cytoplasm [73]. Hence, the CAS to NES-cargo (Kapα) binding exerts an intrinsic regulatory function for nuclear RanGTP export.

Located in the cytoplasmic filaments of the NPC, the GTPase-activating RanGAP hydrolyses RanGTP irreversibly to RanGDP ($\Delta G \approx -33$ kJmol^{-1}). This causes both, the CAS•RanGTP•Kapα complex to disassemble into Kapα, CAS and RanGDP as well as the RanGTP•Kapβ1 complex to disassemble into RanGDP and Kapβ1 [74, 75]. The released Kapα and Kapβ1 moieties are available again for the next import cycle. Additionally, RanGDP is actively transported back in the nucleus by its specific transport factor NTF2 [76, 77]. Once in the nucleus, the GDP-precursor is recharged to RanGTP by the chromatin-bound guanine exchange factor RanGEF (Figure 1.5 B) [78].

Given the asymmetric distribution of RanGAP and RanGEF, a ~200x – 1000x higher concentration of RanGTP is established in the nucleoplasm as compared to the cytoplasm, even though RanGTP and RanGDP (~27 kDa) are both small enough to diffuse passively through the NPC barrier structure [79].

1.2 Nucleus specific nanocarriers

1.2.1 Viruses and viral delivery systems

Owing largely to highly specific, evolutionary adapted biochemical interactions, viruses are able to bind to the cell surface, cross the plasma membrane, hijack intracellular transport systems and escape the endosomal pathway [80]. Due to their inability to autonomously reproduce, viruses are required to deliver their genome to an exact spatial location (*e.g.* cytoplasm or nucleoplasm) where they hijack the cellular machinery to perform genome replication. The mechanistic details of the underlying growth cycle may vary amongst viruses. In case of the app. 90 – 100 nm large adenovirus [81], the surface of the genome enclosing capsid is covered with multiple copies of specific proteins that are acting as cell-targeting signals. These proteins mediate the cell entry by receptor-induced endocytosis and simultaneously determine the range of infectable host cells. The infectious process begins with the endosomal release, *i.e.* the entry of the viral capsid into the cytoplasm. The internalized virus starts migrating along microtubules until it reaches the cell nucleus where the capsids docks to an NPC port and partially breaks open. Subsequent nuclear transport is promoted by its linear genome structure [82]. To do so, parts of the hexon protein based capsid bind to nuclear histones H1 such that in the formed complex, the adenovirus can import its DNA into the nucleus *via* NPC channels [83]. The viral DNA interacts then with the host-cell machinery and facilitates its reproduction.

Disassembly of the enclosing capsid followed by nuclear genome translocation across NPC channels were long assumed to be the general mechanistic steps leading to viral entry into the nucleus. Here, size exclusion manifested by the NPC networks was believed to prohibit the intact capsid import. Contrary to this idea, Panté *et al.* in 2002 showed that phosphorylated Hepatitis B viruses with core diameter of 32- and 36 nm are indeed able to cross the nuclear

pores in *Xenopus oocytes* while maintaining full structural integrity (Figure 1.6 [84]).

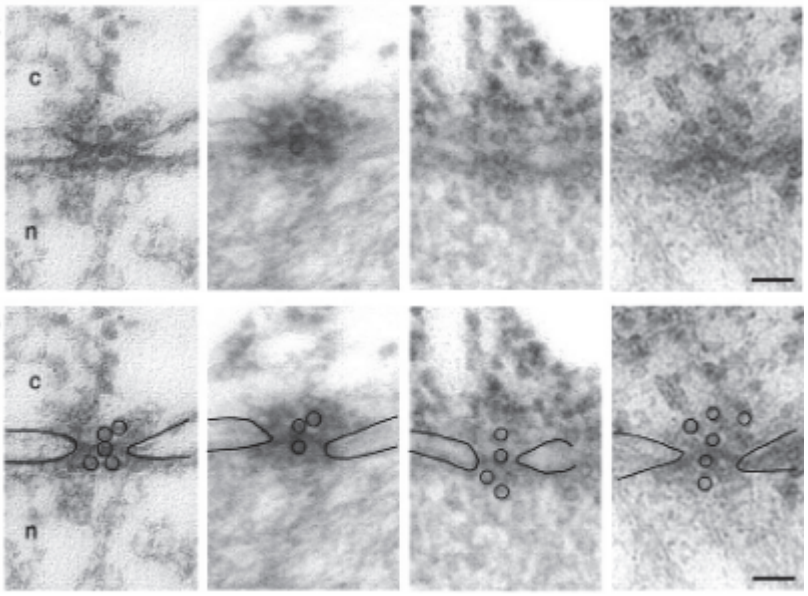

Figure 1.6 Hepatitis B viruses of 32 or 36 nm-diameter can transit NPCs. Representative cross-sections *via* transmission electron microscopy of *Xenopus oocyte* are showing the NE including an NPC. The bottom raw depicts the same micrographs as the top but with highlighted NE boundaries and virus cores. Figure reproduced from Panté and Kann (2002) [84].

Retroviruses employ a different strategy to gain access into cell nuclei. They wait in the cytosol until the nuclear envelope breaks open during mitosis and upon rupture, translocate non-specifically into the cell nucleus. Yet, a drawback of this strategy is that retroviruses can only replicate in dividing cells [82, 85].

Overall, viruses are highly potent in entering cells and therefore, appear to be excellent candidates for gene delivery applications. So far, the retrovirus murine leukemia and the Adenovirus type 2 (AD-2) have been used in > 90 % of all gene therapy trials. Current attempts, however, are proceeding slowly since it is challenging to find the appropriate viral dosage and AD-2 vectors have an extremely narrow viral host range leading to inefficient infections in certain cells. To overcome low infection rates, retroviruses can be used as they exhibit a high

infection rate to a wide variety of cells [86]. An additional constraint is the potential activation of an anti-vector immune response that becomes more likely with the use of AD-2 vectors [87].

Certain major restrictions are fundamental to all viral vectors. First, their limited capsid size decreases the capacity for therapeutic gene payloads and second, safety issues are integral to viruses due to a lack of target-cell specificity, immunogenicity and, for some viral vectors, induced mutagenesis. These drawbacks have tremendously limited the usage of recombinant viruses in clinical settings [87]. Nevertheless, the highly evolved structural and biological functions of viruses have inspired the development of smart synthetic non-viral delivery systems.

1.2.2 Non-viral delivery systems

For more than two decades, biofunctional NCs have gained increasing importance in bio-medical applications *e.g.* for the development of advanced diagnostic or drug delivery systems [88, 89]. Here, synthetic vectors are a valuable alternative to viral therapy forms as they can serve as very effective delivery vehicles but are safe to use. Long blood circulation times and superior bioactivities increase the NCs specificity and targeting efficacy as compared to small molecular drugs. While encapsulated in a NC structure, bio-active substances (*e.g.* genes, enzymes, antibodies, or small drugs) are more likely to reach the foreseen site of action in an active form and attain a sufficient therapeutic concentration *in situ.* Consequently, targeted drug delivery minimizes the therapeutic drug dose and reduces the therapeutic risk of overdose side effects [90-92]. In addition, the development of synthetic NCs allows for versatile medical conditions that can be targeted. Appropriate NC design and conjugation with biological functions (*i.e.* ligands, enzymes or antibodies) is however required to successfully target a

diseased organ, tissue, cell or even sub-cellular organelle [93, 94]. Nonetheless, to exert an organelle-specificity, NCs must bypass several cellular barriers.

Following the internalization of nucleus specific NCs, the first physical barrier encounted is the plasma membrane. While it is impermeable to molecules > 1 kDa, complexes and NCs larger than 25 nm are capable of utilizing specific mechanisms to internalize [95]. Cell surface approaching NCs are typically uptaken by some form of endocytosis (Figure 1.7). Encapsulated into primary endosomal vesicles, NCs are then either directly exocytosed or continue their cellular internalization through the transportation to early endosomes that are located at the cell membrane periphery. Endosomes then migrate along the microtubules to the perinuclear region where they are converted to late endosomes. Fusion with lysosomes generate so called endolysosomes in which active digestion takes place [96]. Survival of the lysosomal degradation is hence the most critical internalization mechanistic step. Therefore, NCs are required to maintain their structural integrity even at low pH and to escape the lysosomes before being degraded. To this end, NCs can employ different mechanisms to rupture the endosomal membrane. Inspired by viruses and bacteria, endosomal release may be induced by pore formation in the membrane [97], the photon sponge effect (or pH buffering effect [98-100]) or a photochemical membrane disruption [101].

NCs that are freed from the endosomal pathway transport through the cytoplasm and eventually reach the cell nucleus as their ultimate target. The NE is ultimately the last cellular barrier. To overcome it and to enter the nucleus, NCs are believed to largely employ the traditional molecular NCT mechanisms that were described in Thesis section 1.1.

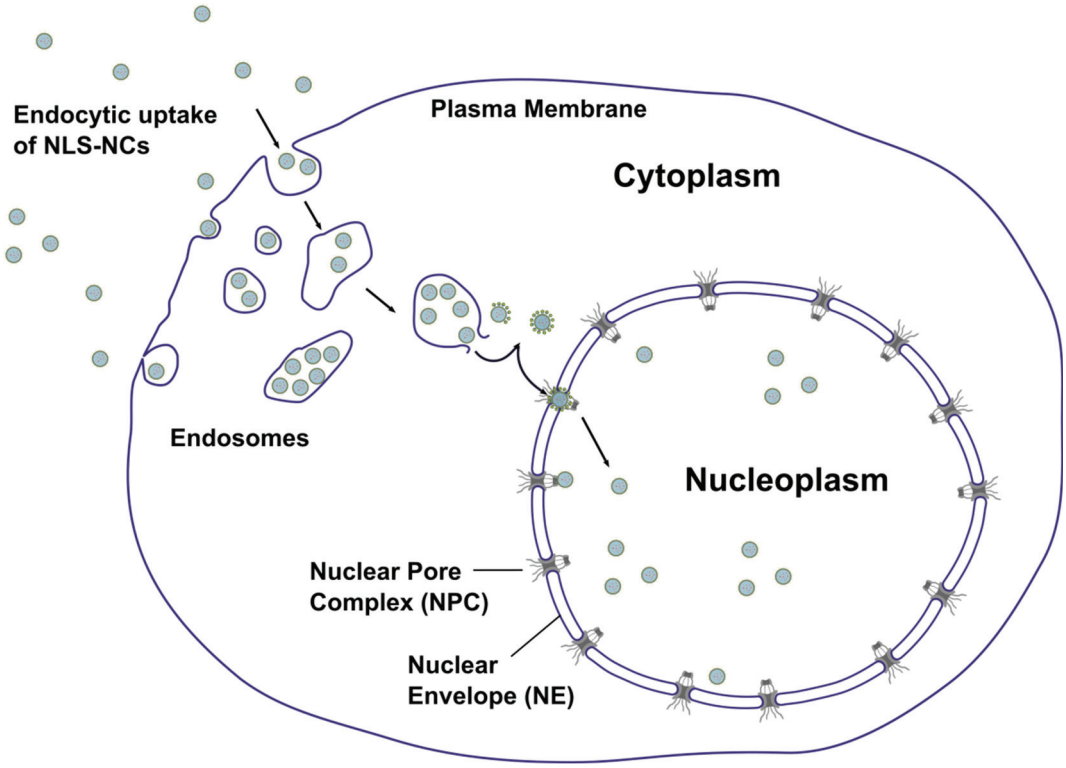

Figure 1.7 Schematic cellular internalization pathway of nucleus specific nanocarriers.

Several cell internalizing NCs have been reported yet. Here, cytoplasmic releasing carriers have proven their efficiency, particularly in DNA/RNA delivery [102]. Even so, additional tagging of NCs with NLS has further improved results [103, 104]. NLS-functional NCs have been identified in surface-binding Kapα/β1 receptors onto chitosan nanoparticles [105], gold beads [84] or polymersomes [106]. Also surface conjugation with the short IBB domain has proven to mediate nuclear entry by direct binding of standalone Kapβ1 to functional quantum dots [58].

1.3 Bioinspired nanocompartments based on synthetic polymersomes (partially reproduced from [4])

Molecular self-assembly is a self-driven process essential to various systems in nature such as formation of cell membranes, protein folding and DNA hybridization. Internal organization of self-assembled systems is governed by inter- (van der Waals, dipole-dipole, and hydrogen bonding) and intra-molecular (hydrophobic) forces that drive the molecules into a low energy stable state [107]. Here, cell membranes are compartment enclosing phospholipid bilayers that are separating different biological environments and contain embedded proteins responsible for biological communication and molecular transport [108, 109]. Phospholipids provide structural stability for membranes, and high lateral fluidity, which enables the functionality of embedded membrane proteins. One of the most important functions of a biomembrane is its selective permeability which allows only selected moieties to cross the barrier. Although biomembranes are composed of similar phospholipids, their functionalities are mostly determined by the specificity of their associated proteins: there are over 300 types of ion channel in a living cell [110].

The structural and functional complexity of biomembranes has challenged researchers to develop simpler artificial models to mimic their properties. Amphiphilic block copolymers are of particular interest because of the dual environmental affinity that is associated with covalently bound hydrophobic and hydrophilic blocks. These blocks strive to minimize their contact, and therefore drive self-assembly into varying architectures [111]. Based on their chemical specificity, such as the hydrophilic-to-hydrophobic ratio, amphiphilic block copolymers can self-assemble in dilute aqueous solutions into micelles, polymersomes, tubes, wire-like structures, nanoparticles, or planar membranes at a water-air interface [112, 113]. Polymersomes are of significant interest, because

of their unique architecture which involves a membrane enclosing central aqueous compartment, similar to that of biocompartments [114]. The internal cavity of polymersomes serves as a container for payloads, either by acting as a drug delivery system, or as a nano-space for reactions in so-called nanoreactors. A key parameter for *in situ* catalytic reactions is permeability of polymersome membranes to allow exchange of substrates/products with the environment. Therefore, selection of the amphiphilic copolymer and the type of the corresponding supramolecular assembly must match both the selected biomolecule and the intended application. Biomimetic strategies have since been used to produce synthetic membranes (polymersomes but also planar membranes) that can be combined with biomolecules for developing novel functional materials and systems (Figure 1.8).

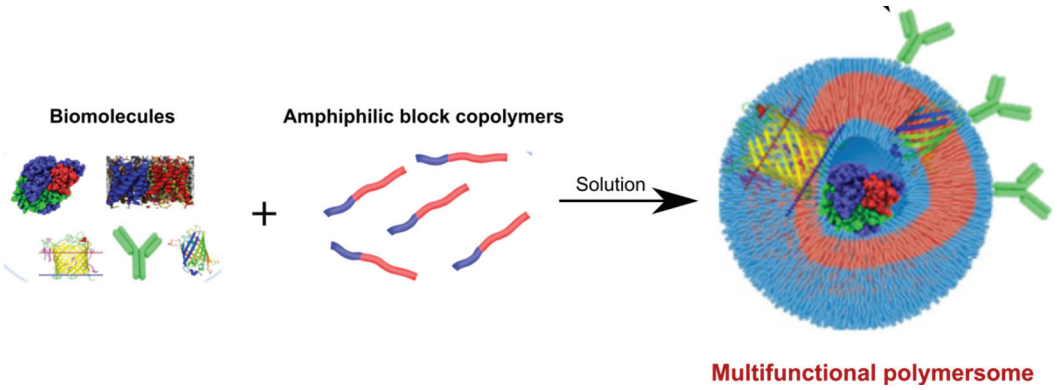

Figure 1.8 Conceptual overview for the preparation of bioinspired polymersomes. Figure reproduced and modified from Mikhalevich, Zelmer, Car and Palivan (2016) [4].

Polymersomes are ideal candidates for a large variety of applications, such as (i) drug delivery-containers, [115] (ii) compartments for contrast agents, [116] (iii) nanoreactors to serve as confined nano-spaces for transport phenomena and chemical transformation, [117-122] and (iv) artificial organelles or simple mimics of cells [123].

1.3.1 Proposed nucleus specific polymersome-NCs

Initial considerations for the NC design involved the choice of the constructing nanomaterial, the molecular carrier composition, the structural architecture, and the structural incorporation of therapeutic agents. On this account, vesicular structures (like polymersomes) hold great potential to function as nanocarriers. Given their unique architecture that segregates a central aqueous compartment by an enclosing membrane, polymersomes are suitable for the transport of bioactive compounds either by encapsulating them inside the aqueous cavities (hydrophilic compounds), by intercalating them in the membrane (hydrophobic compounds) or by attaching them to the vesicle's surface (*e.g.* by functionalizing bioactive moieties for targeting purposes).

Here, the vesicular membrane is prepared from synthetic poly(2-methyl-2-oxazoline)-*block*-poly-(dimethylsiloxane)-*block*-poly(2-methyl-2-oxazoline) ($PMOXA_4$-$PDMS_{44}$-$PMOXA_4$) triblock copolymer as well as a maleimide chain termini functionalized derivative. The amphiphilic nature of the polymers drives their spontaneous molecular self-assembly. Here, a block-ratio of 35 % ± 10 % hydrophilic to total molecular mass ratio [124] results in polymersome structures. Because of the higher molecular weight, polymersomes exhibit an enhanced membrane strength and stability as well as membrane thickness and stiffness as compared to their natural analogues, liposomes [1, 2]. Furthermore, the inert chemical nature renders the triblock copolymer biocompatible.

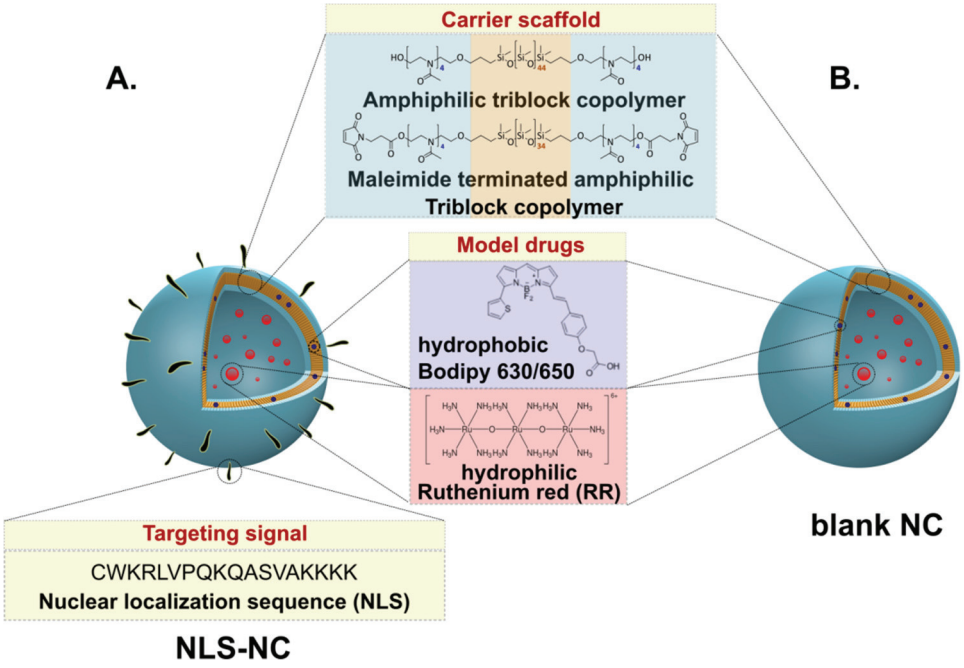

Figure 1.9 Illustration of multifunctional NCs based on amphiphilic triblock copolymers. The polymersome scaffold allows for structural integration with hydrophilic and/or hydrophobic drugs. **A.** NLS-NCs are designed to deliver their cargo directly into cell nuclei *via* covalent surface attachment of NLS signals. **B.** Non-specific blank NCs are lacking the nuclear targeting signals and deliver their cargo into the cell cytoplasm.

Also, the NC size is an important parameter to conceptualize. Here, a NC diameter of about 50 nm is desired to accommodate cargo compounds in sufficient concentration and is further recommended to not force polymers to self-assemble into micelle structures. Such large NCs however, require an active nuclear import *via* NPCs [84]

The selective nuclear delivery is enabled by NC conjugation with the naturally occurring NLS bipartite (see the NLS-NC in Figure 1.9 A). To demonstrate the generality of the NLS-NCs biofunctionality, an unspecific cargo was developed that was self-assembled from the $PMOXA_4$-$PDMS_{44}$-$PMOXA_4$ block-copolymer only. Such blank nanocarriers (see the blank NC in Figure 1.9 B) lack the NLS uptake trigger and exceed the NPC cut-off (> 5 nm and > 40 kDa). Thus, they are unlikely to get imported into cell nuclei. In addition, NLS-NCs are used as vehicles for nuclear cargo delivery and therefore two model drugs encapsulated.

1.4 Aim of the Thesis

Motivation for this PhD work was to develop nucleus specific NCs that: First, can actively and efficiently deliver therapeutic entities in an organelle-specific manner and second, can be applied to study NCT on a single event level. This motivation results from the fact that previously developed nuclear targeting nanoparticles (NPs) were used either for drug delivery purposes or to study the mechanism underlying to the NCT of large cargoes. To be more precise, none of the reported NPs had yet the potential to serve both, delivery, and diagnostic applications. However, identifying the NCT mechanistic steps and discriminating the proportion of nuclear imported NCs is a prerequisite to further optimize the NCs import efficacy based on their NCT selectivity. It is therefore the main objective of this Thesis work to investigate the relationship between the NCs structure and their functionality to enter the nucleus *via* NCT.

The previously literature reported NPs can be classified into inorganics (*e.g.* mesoporous silica NPs [125], gold beads [126], quantum dots [58]) or into soft matter NPs (*e.g.* chitosan NPs [105] or polymersomes [106]). Although inorganic NPs are formidable to study their nuclear import trajectories by the means of EM or other optical methods [126], they are often cytotoxic and offer only limited drug encapsulation capacity. Opposed to that, soft matter objects exert high biocompatibility and are excellent carriers for various therapeutic entities. Nevertheless, the chemical similarity to cellular components (soft matter NPs and cells are composed of similar and/or equal elements: C, H, N & O) hampers high resolution analytics by EM and so, to date, there is little evidence on how mechanistically up to 150 nm large drug-carriers are targeting the cell nucleus [105].

To overcome those limitations, Chapter 2 of this work describes a bottom-up strategy for the nanoengineering of polymersomes that can take up cellular

NCT mechanisms and that allow following their nuclear internalization by EM. To this end, the syntheses of the NCs scaffold material PMOXA-*block*-PDMS-*block*-PMOXA and its derivates is deduced. Furthermore, the catalyst- and solvent free linking-reaction applied for NC conjugation with NLS is described. Also included are the physico-chemical characteristics of the assembled NLS-NCs with respect to their size, shape, surface charge, molecular composition, and functional NLS-degree per vesicle. All following structure–functionality correlations have been drawn based on those NC characteristics.

Chapter 3 aims to reconstitute the three key NCT mechanistical steps leading to successful nuclear NLS-NC import. For this purpose, different *in vitro* assays were employed to analyze each of the subsequent steps individually. Specifically, first binding of NLS-NCs to recombinant Kaps was investigated using a titration assay and detected by fluorescence cross-correlation spectroscopy (FCCS). This step is followed by the molecular recognition of the Kap•NLS-NC complexes by FG-Nups, which was analyzed using again a titration assay but surface plasmon resonance (SPR) spectroscopy for detection. The NCT terminating step of Kaps and NLS-NC dissociation by RanGTP was examined with SPR and additionally with a permeabilized HeLa cell assay.

Chapter 4 focuses on the actual nuclear import of NLS-NCs in live cell studies. Here, the visualization of NLS-NCs in NPC transit was particularly important to verify import specificity and was carried out by EM in combination with a therefore adapted staining protocol. In addition, nuclear uptake-kinetics and biodistributions of cell internalized NLS-NCs were evaluated using fluorescence microscopy for their detection.

At the end, Chapter 5 aims to identify ways to open the NLS-NCs and to release the encapsulated cargo `on-demand`.

Chapter 2

Engineering Nuclei-Targeting NCs

Thesis chapter contributions

Dr. A. L. Dinu (Postdoctoral researcher at University of Basel): Supervision and advisory support with the PMOXA-PDMS-PMOXA triblock copolymer synthesis.
P. Z. Güven (PhD student at EPFL Lausanne): Cryo-EM imaging of NLS-functional and blank polymersomes.

2 Engineering nuclei-targeting NCs

2.1 Introduction

Cell nuclei targeting NCs make use of intracellular trafficking pathways and cross several successive cellular barriers before they reach the cell nucleus as their destination [127-129]. Previously, it has been shown that the success of nuclear NC import is highly dependent on the intrinsic structural and physico-chemical properties of the applied NCs [126, 130-132]. Amongst other things, it is influenced by the NCs size, shape, surface charge, morphology, type, and degree of functionalization with nuclear targeting signals, as well as the cell type that is targeted. All those parameters can bias biochemical interactions with cellular components, and it is thus not surprising that appropriate nanoengineering of the NC structure is key to enable their successful nuclear administration.

In the present work, a novel nuclear targeting NC system was developed based on polymer vesicles called polymersomes. More specifically, polymersomes with controllable size and morphology were prepared from the amphiphilic triblock copolymer poly(2-methyl-2-oxazoline)-*block*-poly-(dimethylsiloxane)-*block*-poly(2-methyl-2-oxazoline) (PMOXA-PDMS-PMOXA) (Figure 2.1 A). These synthetic constructs are essentially biocompatible [133] and have proven to be ideal candidates for receptor-based cell targeting applications [134]. As a further step forward, these polymersomes were given even more complex targeting functionality that is required for their translocation into the cell nucleus. The targeting specificity is granted to the overall NC structures by co-assembling a maleimide functional PMOXA-PDMS-PMOXA derivate into the polymersome membrane and subsequently functionalizing cysteine conjugated nuclear localization sequences (NLSs) extraluminally with a spontaneous thiol-ene 'click' reaction (Figure 2.1 B) [135, 136]. In addition, this work uses two model payloads

(RR and Bodipy) that were structurally integrated into the NCs to expand their scope towards nuclear site-specific drug-delivery applications.

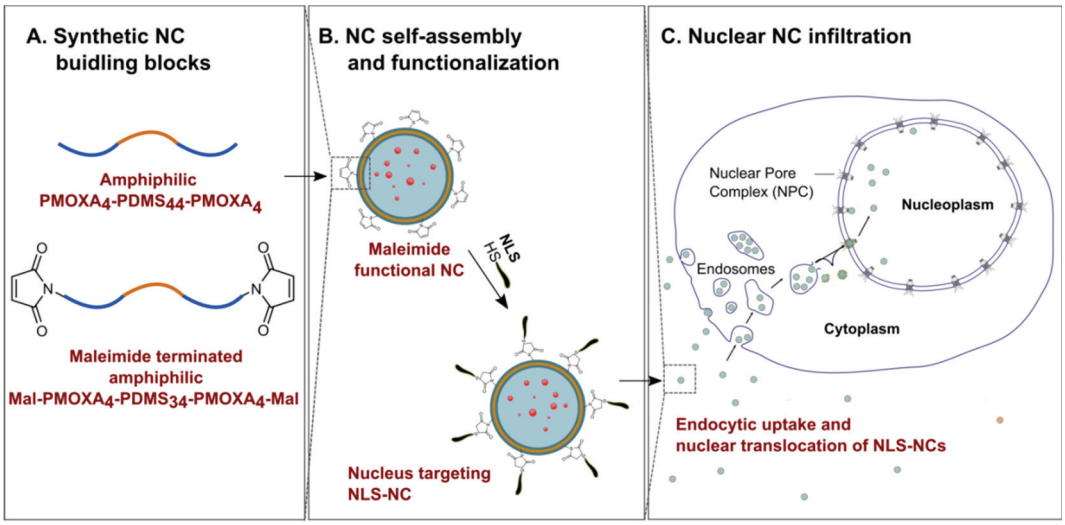

Figure 2.1 Polymersome-NCs are nanoengineered to translocate into cell nuclei. A. The NCs are prepared from amphiphilic $PMOXA_4$-$PDMS_{44}$-$PMOXA_4$ mixed with a maleimide end-group functionalized polymer derivative. **B**. The amphiphilic polymer character drives their self-assembly into polymersomes with exposed maleimide groups that extraluminally react to form covalent bonds with cysteine-terminated nuclear localization sequences (NLSs) **C**. NLS-NCs are recognized as authentic nucleus-destined cargoes and translocate selectively into cell nuclei.

NLS-NCs can be internalized into eukaryotes and - upon their identification as authentic nucleus-destined cargoes - to be selectively imported into cell nuclei (Figure 2.1 C). This chapter will provide details about the synthetic (Thesis section 2.2) and preparative strategies (Thesis section 2.3) used to manufacture the nuclear targeting NLS-NCs. In addition, the NCs physico-chemical properties are addressed (Thesis section 2.4) with special focus on the NCs size, morphology, molecular composition, surface charge and the substitution with nuclei-destined model payloads.

2.2 Synthesis of the NC constituents

As a building block for cell nuclei targeting polymersomes, a high molecular weight $PMOXA_4$-$PDMS_{44}$-$PMOXA_4$ copolymer was synthesized. This polymer is essentially an amphiphile that undergoes a self-directed assembly process into stable and closed vesicles once added in aqueous media [137]. The amphiphilic character of the linear PMOXA-PDMS-PMOXA copolymer is the result of a block-like monomer arrangement, segregating here the hydrophilic MOXA repeats from the hydrophobic DMS ones. This physical segregation is achieved synthetically and therefore a commercially presynthesized PDMS homopolymer used as inner hydrophobic block. In a cationic ring-opening polymerization reaction, MOXA monomer is polymerized onto PDMS both ends (Figure 2.2 A) and yielded the essential hydrophobic-hydrophilic-hydrophilic polymer character. The final architecture of PMOXA-PDMS-PMOXA after self-assembly (*e.g.* micelles, worms, vesicles, tubes, etc.) is however highly dependent on the relative mass or volume fractions f within the individual polymer blocks. Only macromolecules with a hydrophilic fraction $f_{hydrophilic}$ of > 25 % and < 45 % are expected to self-assemble into two-dimensional membranes that can subsequently bend to form three-dimensional vesicles [138]. It is thus indispensable to isolate the vesicle-forming polymer fraction from the crude polymer mixture by purification using extraction and/or filtration. Accordingly, in this work the triblock copolymer $PMOXA_4$-$PDMS_{44}$-$PMOXA_4$ **1** with a number average molecular weight of M_n = 4000 Da and an $f_{hydrophilic}$ of 29 % was synthesized and yielded here the desired scaffold material for the proposed nuclear targeting NLS-NCs (see Thesis section 2.2.1 for synthesis details).

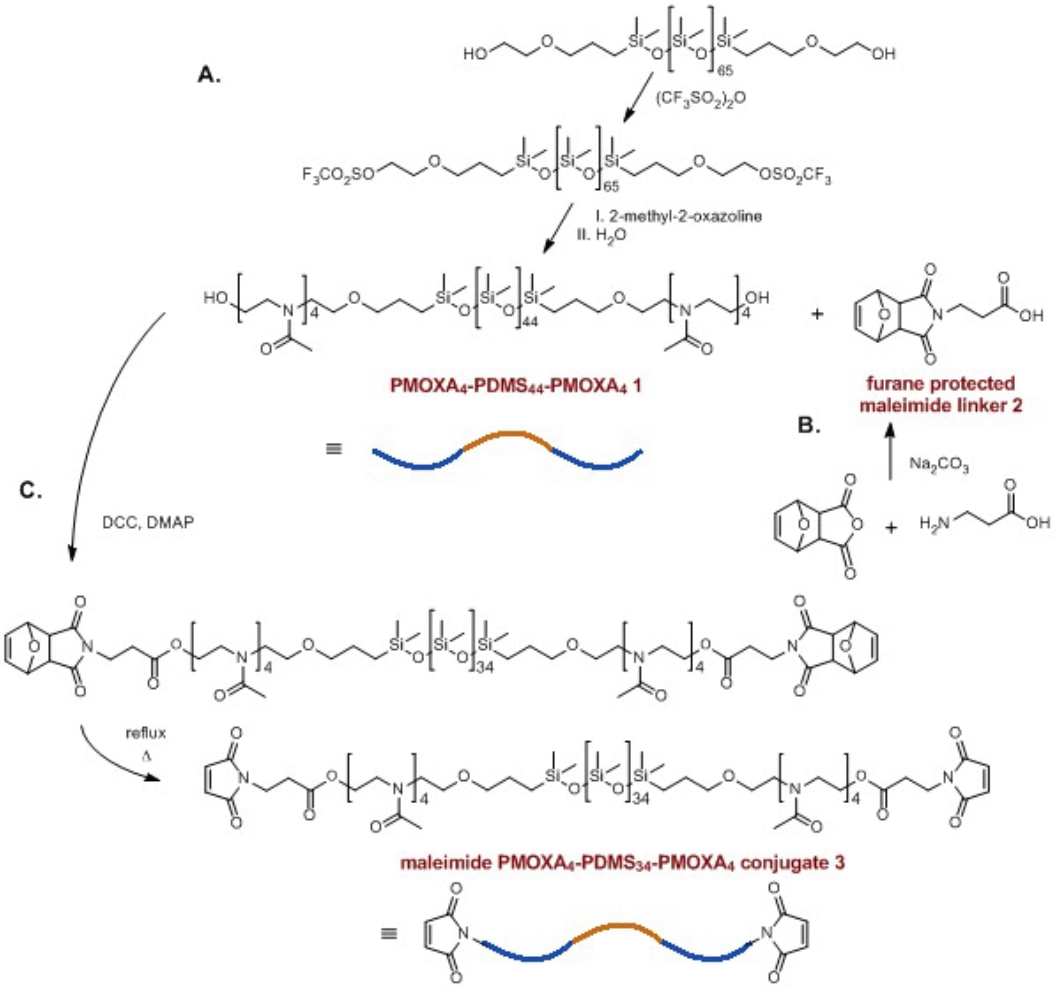

Figure 2.2 The NC constituting polymers and linker were synthesized: **A**. *via* cationic ring-opening polymerization of 2-methyl-2-oxazoline (MOXA) to both ends of bitriflate-activated poly(dimethyl siloxane) (PDMS), resulting the amphiphilic $PMOXA_4$-$PDMS_{44}$-$PMOXA_4$ **1** and **B**. from β-alanine that reacts with the furan-maleic anhydride Diels-Alder (DA) adduct to the furan protected maleimide linker (FMal) 2. **C**. Subsequent condensation of **2** to the polymer **1** gives a maleimide functional $PMOXA_4$-$PDMS_{34}$-$PMOXA_4$ conjugate **3** after thermal furan deprotection.

As a second building block for nuclear targeting NLS-NCs, a maleimide conjugated $PMOXA_4$-$PDMS_{44}$-$PMOXA_4$ derivative **3** was synthesized by a specially developed three-step synthesis protocol. This required first the separate synthesis of the maleimide linker **2** (see Figure 2.2 B and Thesis section 2.2.2 for synthesis procedure). Condensation of a furan-maleic anhydride Diels-Alter (DA) adduct to β-alanine yielded a furan protected linker that prevented maleimide hydrolysis throughout ensuing synthesis and purification steps.

The linker's carboxyl functionality enabled its conjugation to hydroxyl terminated $PMOXA_4$-$PDMS_{44}$-$PMOXA_4$ **1** in a second esterification step (Figure 2.2 C). The furan protecting-group is eventually cleaved off by a thermally-induced retro-DA reaction giving the maleimide $PMOXA_4$-$PDMS_{34}$-$PMOXA_4$ conjugate **3**, with an M_n of 3800 Da and an $f_{hydrophilic}$ of 32 % (see Thesis section 2.2.3 for details).

2.2.1 Amphiphilic triblock copolymer $PMOXA_4$-$PDMS_{44}$-$PMOXA_4$

PMOXA-PDMS-PMOXA (poly(2-methyl-2-oxazoline)-*block*-poly(dimethyl-siloxane)-*block*-poly(2-methyl-2-oxazoline)) triblock copolymer was synthesized according to previously published protocols [137, 139] with slight modifications. In the first synthesis step, bifunctional carbinol-terminated poly(dimethylsiloxane) (PDMS) was dissolved in hexane, cooled to -10 °C and reacted with triflic acid anhydride (see Figure 2.2 A). Triethylamine (TEA) was added to the mixture to neutralize the triflic acid formed as a by-product. The precipitated organic salt was removed by filtration through an ice-cooled G4 filter funnel. Afterwards, the filtrate was removed *in vacuo* and a mixture of anhydrous acetonitrile/ dichloromethane (1:1, v/v) was applied to dissolve the bitriflate-activated PDMS for ensuing reaction steps. Freshly distilled 2-methyl-2-oxazoline (MOXA) was added in one shot and initiated the polymerization onto PDMS both ends. The reaction was stirred for 60 hours at room temperature before it was quenched with a TEA/water mixture (1:4, v/v). Finally, the crude polymer mixture was worked up by ultrafiltration using a water/EtOH mixture (1:2, v/v) followed by extraction with a MeOH/hexane solvent combination (1:1, v/v). The final product was obtained with an isolated yield of 28 % and was characterized by ^{1}H NMR (Figure 2.3) and GPC.

The final triblock copolymer composition was determined to be $PMOXA_4$-$PDMS_{44}$-$PMOXA_4$ (NMR) and corresponds to a calculated number average

molecular mass M_n of 4000 Da and a hydrophilic to total molecular mass ratio *f* of 29 %. The overall polymer dispersity is 1.7 (GPC).

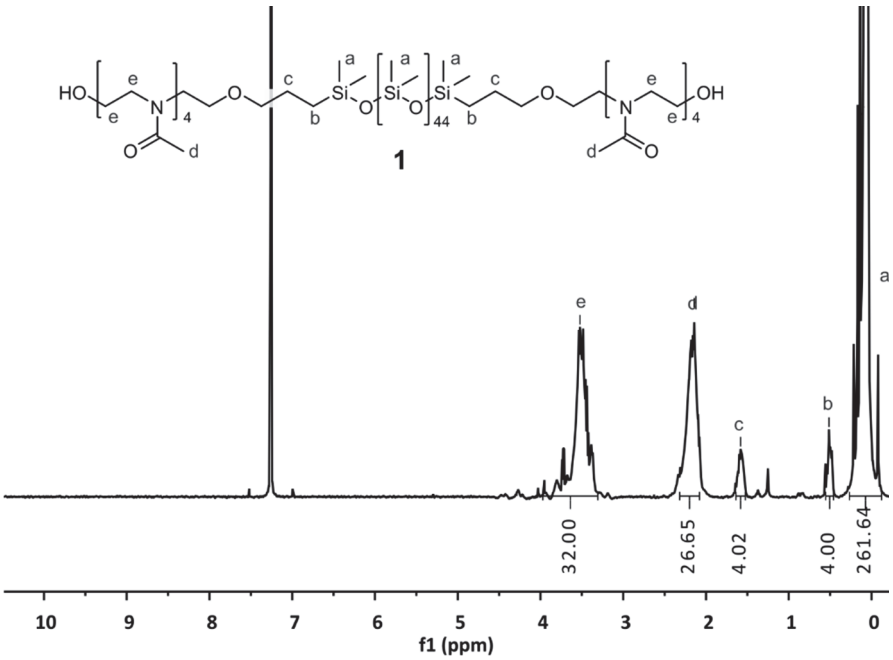

Figure 2.3 ^{1}H NMR spectrum of PMOXA$_4$-PDMS$_{44}$-PMOXA$_4$ 1. The spectrum was recorded at 400 MHz in $CDCl_3$ and contains all structure specific peaks at δ/ppm: a, 0.28 – (- 0.13) (bs, 6H, $SiCH_3$) b, 0.56 – 0.45 (bm, 4H, $SiCH_2$) c, 1.65 – 1.53 (bm, 4H, $CH_2CH_2CH_2$) d, 2.32 – 2.07 (bs, 6H, $C(O)CH_3$) e, 3.97 – 3.31 (bm, 8H, CH_2NCH_2).

2.2.2 Furan protected maleimide linker

The synthesis of the furan protected maleimide linker (FMal-linker, 3-(1,3-dioxo-1,3,3a,4,7,7a-hexahydro-2H-4,7-epoxyisoindol-2-yl)propanoic acid) **2** followed procedures described in [140] and [141]. Specifically, the furan-maleic anhydride DA adduct 3a,4,7,7a-tetrahydro-4,7-epoxysobenzofuran-1,3-dione (4.5 g, 27.1 mmol) and Na_2CO_3 (2.87 g, 27.1 mmol) were dissolved in 100 ml MeOH and a solution of β-alanine (2.41 g, 27.1 mmol) in 100 ml MeOH was slowly added (Figure 2.2 B). The reaction mixture was stirred for 6 days at 56 °C before the solvent was removed and the resulted white residue re-dissolved in 100 ml CH_2Cl_2. The solution was extracted 4 times with 80 ml of 0.6 M aqueous HCl and the collected organic phase dried over anhydrous $MgSO_4$ and filtered.

Removal of CH_2Cl_2 under reduced pressure furnished the FMal-linker as white crystalline powder. The final product was obtained with an isolated yield of 52 % and was structurally identified as the FMal-linker **2** using ^1H NMR analysis (Figure 2.4).

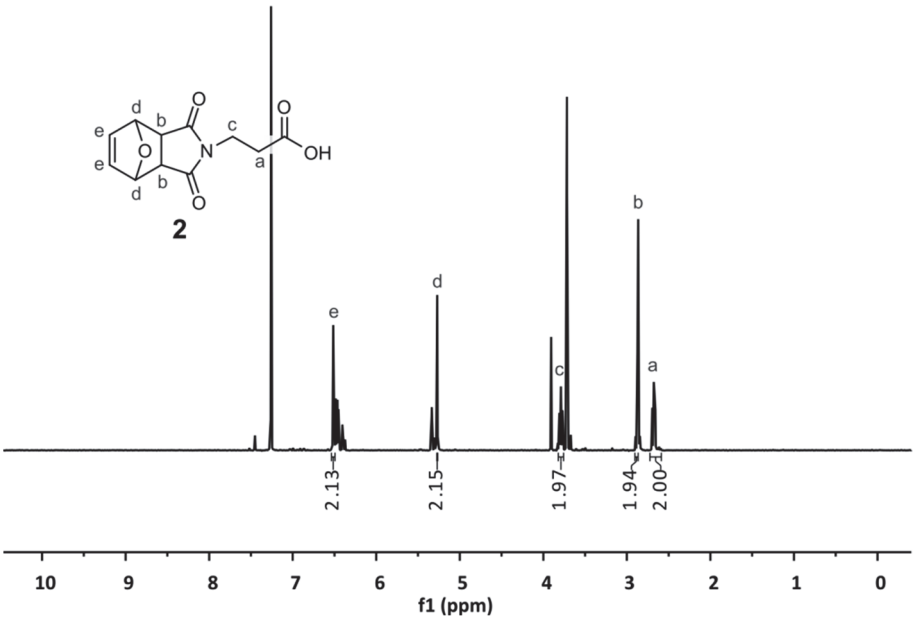

Figure 2.4 ^1H NMR spectrum of the furan protected maleimide linker FMal 2. The spectrum was recorded at 400 MHz in $CDCl_3$, and the inset peaks assigned to δ/ppm: a, 2.68 (t, 2H, CH_2COOH) b, 2.87 (d, 2H, CHC(O)N) c, 3.79 (t, 2H, $NCH_2CH_2(O)O$) d, 5.27 (t, 2H, CHOCH) e, 6.51 (t, 2H, CH=CH).

2.2.3 Maleimide linker end-group functionalized $PMOXA_4$-$PDMS_{44}$-$PMOXA_4$

For the synthesis of maleimide end-group functionalized PMOXA-PDMS-PMOXA, procedures reported in [142], [141] and [143] were employed. In detail, a two-step synthesis route was developed that first requires the esterification of the triblock copolymer $PMOXA_4$-$PDMS_{44}$-$PMOXA_4$ **1** with the protected FMal **2** (see Figure 2.2 C). Therefore, the linker **2** (23 mg, 97.2 μmol) was dissolved in 3 ml anhydrous CH_2Cl_2 and under rigorous stirring DMAP (11.9 mg, 97.2 μmol) and **1** (100 mg, 24.3 μmol) added. The reaction mixture was cooled to 0 °C, charged with DCC (20 mg, 97.2 μmol) and stirred for 5 minutes. The cooling was removed

afterwards, and the solution continuously stirred for 10 hours. The precipitated by-product dicyclohexylurea (DCU) was filtered out before CH_2Cl_2 was removed from the filtrate *in vacuo*. The remaining residue was taken up in EtOH and purified using dialysis tubing with molecular mass cut-off 3.5 kDa, once for 2 hours against EtOH/H_2O (1:1, v/v) and twice for 2 hours against deionized water.

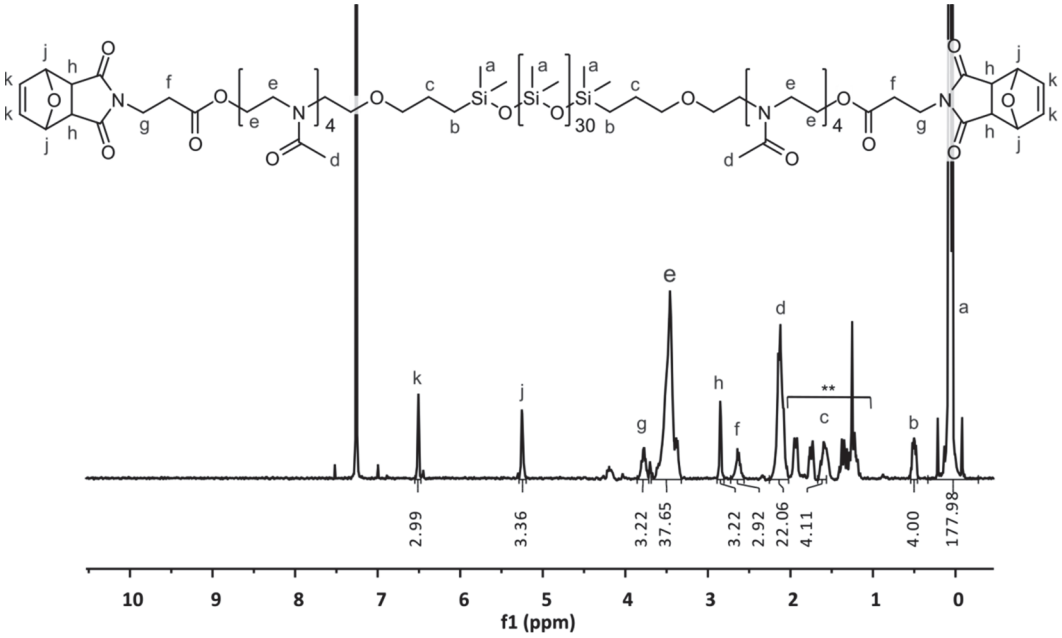

Figure 2.5 ^{1}H NMR spectrum of the FMal-linker end-group functionalized PMOXA$_4$-PDMS$_{30}$-PMOXA$_4$. The spectrum was recorded at 400 MHz in $CDCl_3$ and the containing inset peaks assigned to δ/ppm: a, 0.33 – (- 0.27) (bs, 6H, $SiCH_3$) b, 0.55 – 0.46 (bm, 4H, $SiCH_2$) c, 1.67 – 1.56 (bm, 4H, $CH_2CH_2CH_2$) d, 2.25 – 2.02 (bs, 6H, $C(O)CH_3$) e, 3.66 – 3.32 (bm, 8H, CH_2NCH_2) f, 2.72 – 2.56 (bm, 4H, $CH_2(O)O$) g, 3.86 – 3.71 (bm, 4H, $NCH_2CH_2(O)O$) h, 2.89 – 2.80 (bm, 4H, CH(O)N) j, 5.29 – 5.20 (bm, 4H, CHOCH) k, 6.54 - 6.47 (bm, 4H, CH=CH), **residual DCU.

Importantly, the ^{1}H NMR spectrum recorded for the lyophilized intermediate (Figure 2.5) featured all product specific peaks including the ester connective methylene protons at 2.64 ppm and the furan protons at 2.85 ppm (h), 5.25 ppm (j) and 6.50 ppm (k). It further revealed a PMOXA$_4$-PDMS$_{44}$-PMOXA$_4$ conjugation efficacy with FMal of > 73 % and a block copolymer composition of FMal-PMOXA$_4$-PDMS$_{30}$-PMOXA$_4$-FMal. The product was obtained with 65 % isolated yield, however it contained traces of residual DCU.

In the second synthesis step, the furan protected intermediate was dissolved in 10 ml toluene and under continuous stirring refluxed at 100 °C. This induced a thermal retro-DA furan deprotection reaction, for which the reaction progress was monitored by ^{1}H NMR. As the cleavage evolves, the furan related proton peaks (at 2.85 ppm (h), 5.25 ppm (j) and 6.50 ppm (k)) disappear almost entirely whilst simultaneously the olefinic maleimide proton peak arises at 6.70 ppm shift (h). The deprotection was completed after 9 hours and a ^{1}H NMR spectrum was recorded for the obtained lyophilized product (Figure 2.6). The spectrum revealed a triblock copolymer composition of Mal-PMOXA$_4$-PDMS$_{34}$-PMOXA$_4$-Mal **3** with 34 % of all polymer end-groups being substituted with active maleimide linking sites. The polymer **3** was obtained with 95 % isolated yield, a calculated M_n = 3800 Da (NMR), assuming that it is conjugated on both end-sides, and a hydrophilic to total molecular mass ratio f of 32 %. GPC analysis in DMF showed a polymer weight dispersity of 2.8.

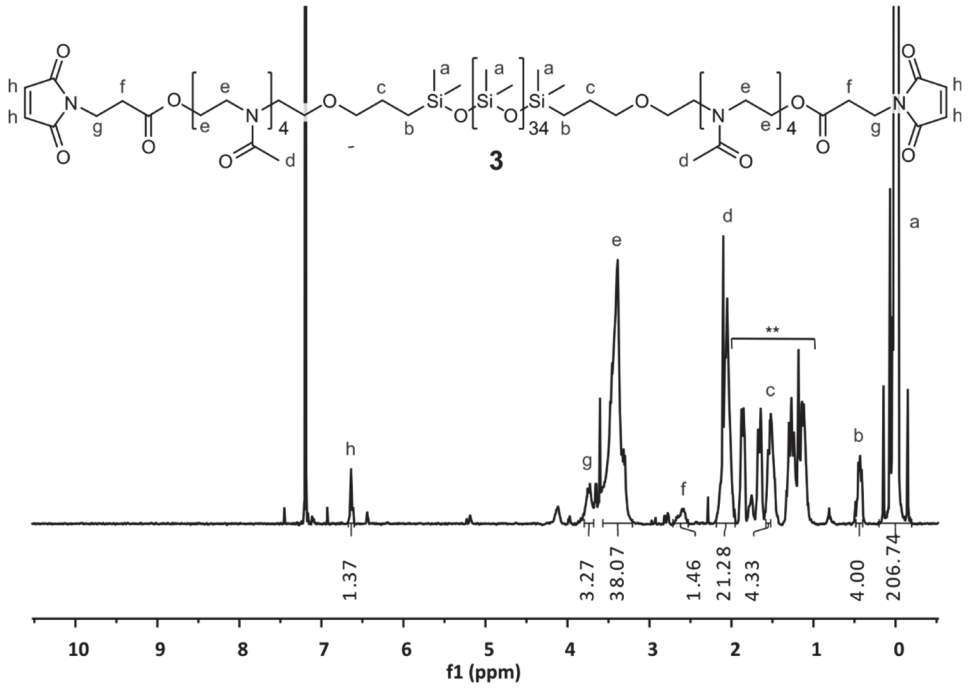

Figure 2.6 ^{1}H NMR spectrum of the Mal-PMOXA$_4$-PDMS$_{34}$-PMOXA$_4$-Mal conjugate 3. The spectrum is recorded at 400 MHz in $CDCl_3$ and the containing peaks used for structural identification δ/ppm: a, 0.27 – (- 0.13) (bs, 6H, $SiCH_3$) b, 0.56 – 0.46 (bm, 4H, $SiCH_2$) c, 1.65 – 1.59 (bm, 4H, $CH_2CH_2CH_2$) d, 2.25 – 2.02 (bs, 6H, $C(O)CH_3$) e, 3.64 – 3.28 (bm, 8H, CH_2NCH_2) f, 2.79 – 2.59 (bm, 4H, $CH_2C(O)O$) g, 3.87 – 3.75 (bm, 4H, $NCH_2CH_2(O)O$) h, 6.74 - 6.67 (bm, 4H, CH=CH), **residual DCU.

2.3 Preparation of NLS-functional and blank NCs

Nuclei targeting NLS-NCs were prepared *via* solvent-free film rehydration method [137]. To do so, a homogenous amphiphilic polymer film was co-assembled from 1.9 mg $PMOXA_4$-$PDMS_{44}$-$PMOXA_4$ **1** (95 wt%, n = 475 nM) and 0.1 mg maleimide end-group functionalized Mal-$PMOXA_4$-$PDMS_{34}$-$PMOXA_4$-Mal **3** (5 wt%, n = 26 nM), then deposited onto the bottom of a round-necked flask. Subsequent film-rehydration in 1 ml PBS containing 75 µM RR furnished the supramolecular polymersome assemblies upon film-desorption from solid support (Figure 2.7 A).

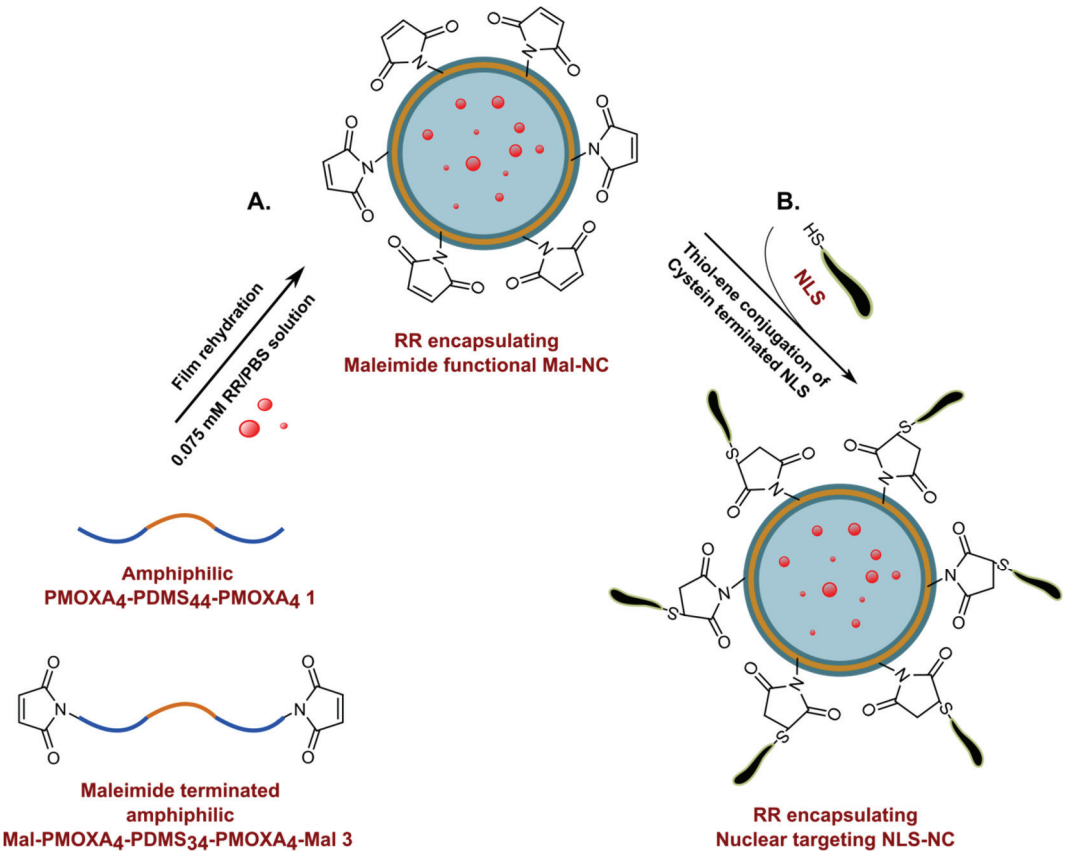

Figure 2.7 Schematic preparation rout towards cell nuclei targeting NLS-NCs. A. Amphiphilic $PMOXA_4$-$PDMS_{44}$-$PMOXA_4$ **1** together with the maleimide terminated derivative **3** undergoes in aqueous environment a spontaneous and self-directed assembly into polymersomes. Payloads, as here model Ruthenium Red (RR), are encapsulated into the vesicle`s lumen during the assembly process. **B.** Vesicle surface presented maleimide groups enable in the next step the NC conjugation with cysteine modified nuclear localization sequence (NLS) bipartites through a catalyst free thiol-ene 'click' reaction.

The RR encapsulating maleimide functional polymersomes (hereafter Mal-NCs) prepared in this way were still of heterogeneous size and were therefore extruded to a mean diameter comparable to the ~ 50 nm wide central NPC channels. Extrusion, in this context, depicts a process where the polymersome membranes are mechanically deformed whilst being squeezed through almost cylindrical 0.05 μm pores of polycarbonate membranes. This results a controlled destabilization of polymersomes larger than the membrane pore size and leads to the formation of smaller sized ones [144]. To generate polymersomes of roughly 50 nm-diameter and narrow size distribution, the extrusion process was repeated 15-times.

In the next step, non-encapsulated RR was removed from the preformed Mal-NCs using size exclusion chromatography (SEC) through a Sephadex G-25 column (GE Healthcare) using the manufacturer's protocol. This yielded the purified Mal-NCs with a mass concentration of 1 mg/ml after elution in PBS running buffer.

The Mal-NCs were eventually rendered viable for nuclear import by adding 0.28 mg of the nucleoplasmin bipartite nuclear localization sequence (NLS – CWKRLVPQKQASVAKKKK, M = 2127 Da; n = 130 nM). This initiates a spontaneous, catalyst-free thiol-ene 'click' reaction where NLS is conjugated across its cysteine terminus onto the NCs presented maleimide linking sites (Figure 2.7 B). Unreacted maleimide groups were quenched after 12 hours reaction time with the addition of 0.02 mg cysteine (M = 121.2 g/mol; n = 130 nM). The reaction was allowed to proceed overnight before the NLS-polymersome conjugates (hereafter NLS-NCs) were purified from unreacted NLS and cysteine by three rounds of dialysis against PBS for two hours each time.

Additionally, non-NLS conjugated NCs (hereafter blank NCs) were prepared as reference specimens and applied throughout as non-specific and `non-nuclei targeting` controls. The same solvent-free method was used to assemble a thin amphiphilic polymer film from 2 mg $PMOXA_4$-$PDMS_{44}$-$PMOXA_4$ that was subsequently rehydrated in 1 ml of 75 μM RR in PBS (Figure 2.8). The purification procedures remained unchanged. Extrusion through 50 nm pore size filters furnished blank NCs with approximately the same size as the NLS-NCs.

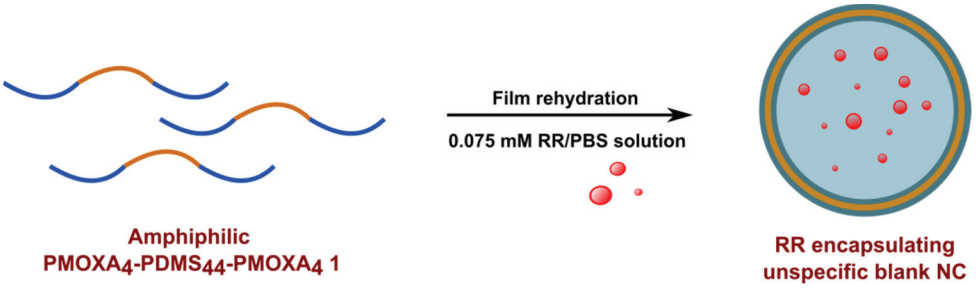

Figure 2.8 Preparation scheme towards non-specific `non-nuclei targeting` blank NCs. Amphiphilic $PMOXA_4$-$PDMS_{44}$-$PMOXA_4$ **1** undergoes in aqueous environment a spontaneous and self-directed assembly into polymersomes. Ruthenium Red (RR) is thereby encapsulated as model payload into the vesicle's lumen.

2.4 Structural characterization of NLS-functional and blank NCs

The cellular fate of nuclear targeting NCs and their nuclear translocation ability through ~ 50 nm NPC channels, is greatly predetermined by the intrinsic NC physico-chemical properties. As consequence it becomes vital to thoroughly study the NC characteristics *in vitro*. Dry & cryogenic transmission electron microscopy (TEM & cryo-EM) were used to measure the size, morphology, and membrane thickness of NCs, and the complementary methods of dynamic & static light scattering (DLS & SLS) were used to measure the size and molecular composition of the NCs.

The degree of NLS-linking sites per Mal-NC was assessed by fluorescence correlation spectroscopy (FCS) and the effect of NLS-conjugation to the overall polymersome surface charge was determined by Zeta-potential measurements. Further, the ability of NCs to encapsulate and delivery cargo entities to a foreseen site of action was investigated for fluorescent payloads using lifetime fluorescence correlation spectroscopy & lifetime fluorescence cross-correlation spectroscopy (FLCS & FLCCS).

2.4.1 Electron microscopic imaging and sizing

A first morphology study of NLS-NCs and blank NCs was carried out using dry transmission electron microscopy (TEM) to visualize the NC structures. The electron microscopic analysis of PMOXA-PDMS-PMOXA based polymersomes is however challenging as they are comprised of mostly light elements (C, H, O, N and Si) with low EM contrast. However, negative staining with uranyl acetate increased the polymersomes visibility and revealed the typical shrunken and dented structures of well dispersed and non-aggregated polymer vesicles (Figure 2.9 A and B upper panel). Statistical evaluation further confirmed that both carriers were formed with similar radii: $\bar{r}$ of 22 $\pm$ 13 nm for NLS-NCs (n = 203) and $\bar{r}$ of 25 $\pm$ 9 nm for blank NCs (n = 157). This means that they are comparable in size with the targeted ~50 nm wide NPC channels [10, 11, 145].

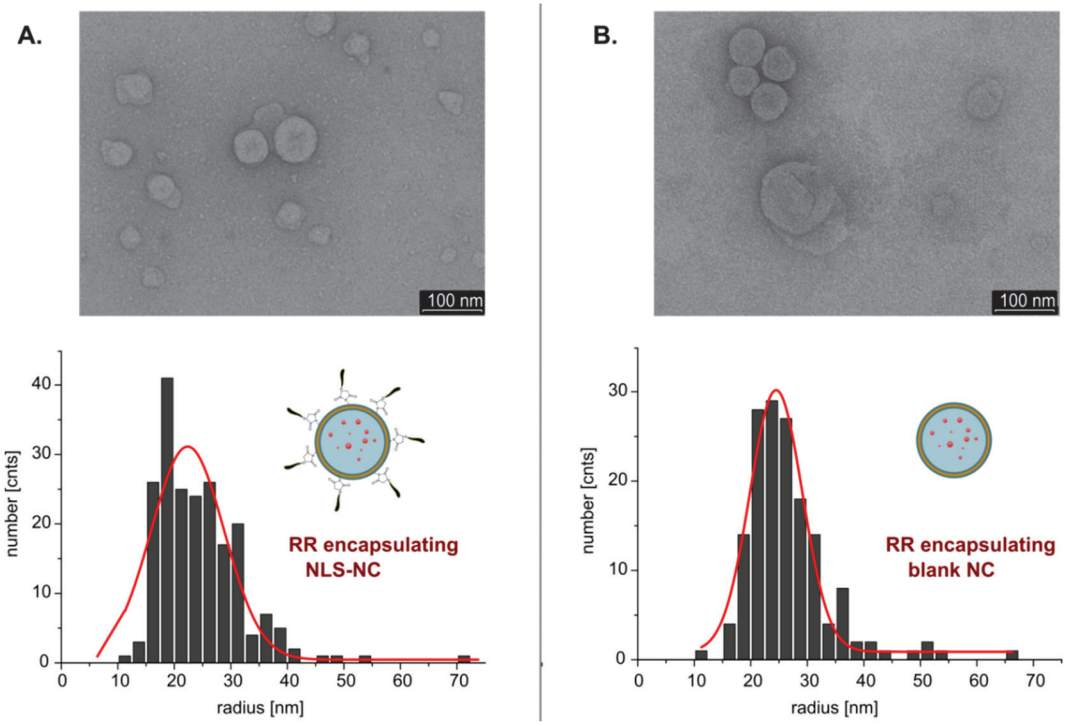

Figure 2.9 Dry TEM micrographs and respective size distribution histograms. A. Uranyl stained NLS-NCs were sized to an average radius of 22 ± 13 nm (n = 203) and **B.** uranyl stained blank NCs to an average radius of 25 ± 9 nm (n = 157).

More detailed insight into the structure and morphology of the NCs was obtained by cryogenic transmission electron microscopy (cryo-EM). Tilting a sheet of frozen NLS-NCs from -20° to 20° confirmed the symmetric hollow and spherical polymer vesicle architecture (Figure 2.10 A). Additionally, NC membrane thicknesses were determined from NLS-NC and blank NC imaging cryo-EM micrographs, measuring at least 300 different points across 20 vesicles of each NC type. An 8.4 ± 1.1 nm-thick membrane was found to span around NLS-NCs and an 8.2 ± 1.5 nm-thick membrane around blank NCs (see Figure 2.10 B). The polymersomes were essentially assembled of high molecular weight $PMOXA_4$-$PDMS_{44}$-$PMOXA_4$ (M_n = 4000 Da) and yielded thicker membranes compared to their natural ~ 4 nm-thick lipid-based analogues (> 1000 Da [2]). Synthetic polymer membranes are furthermore characterized by an enhanced stability and strength (*e.g.* due to physical polymer entanglement within the membrane) and bear an overall increased mechanical resistance that is believed to be one of the

most important prerequisites for intact cellular internalization and nuclear import [146, 147].

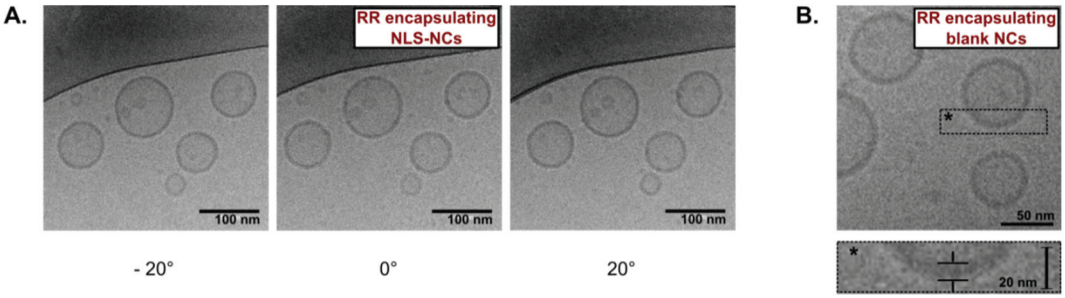

Figure 2.10 Cryo-EM visualization of the NC morphology and membrane thickness. A. The characteristic hollow and spherical NLS-NC structure is captured in a tilt series of images that were taken – 20° to 20 ° around the focal plane. **B.** The blank NCs enclosing amphiphilic membrane is exclusively assembled of $PMOXA_4$-$PDMS_{44}$-$PMOXA_4$ triblock copolymer and attributed with 8.2 ± 1.5 nm-thickness.

2.4.2 Molecular composition and supramolecular architecture

The morphology of the self-assembled supramolecular NCs was further assessed in terms of size, shape, aggregation number and architecture. To do this, combined measurements of static (SLS) and dynamic light scattering (DLS) [148] were conducted on freshly extruded NCs on a commercial Light Scattering Spectrometer (LS instruments). Optical property variations from the vesicle interior to the medium surrounding the vesicles may lead to additional scattering vector contributions, and so a full and systematic analysis of the NCs scattering properties was required. The effect of the incorporated payload RR was assessed by comparative measurements between blank NCs encapsulating 75 μM RR in PBS and blank NCs encapsulating only PBS.

SLS measurements were setup as follows: the average scattering intensities were examined for different polymersome concentrations of 0.15, 0.3, 0.4 and 0.5 mg/ml in PBS. Each concentration was measured at different scattering angles from 40° to 110° taking a step width of 10° and a signal integration time of

20 s per measured angle. The scattering intensities were recorded for all conditions in three individual runs and the measurement results were analyzed using Berry plots (Figure 2.11 A and B upper panel). The radius of gyration R_g, the weight average molecular mass M_w and the second viral coefficient B_2 were extracted from extrapolations to zero concentration ($c \rightarrow 0$) and zero scattering angle ($\theta \rightarrow 0$) and summarized in Table 2.1 (see also Appendix 6.1.1 for a detailed theoretic SLS description). Hydrodynamic radii (R_h) distributions were obtained for the samples using DLS measurements, performed at a scattering angle of 90° using 0.15 mg/ml diluted polymersome dispersions with a signal integration time of 60 s (Figure 2.11 A and B lower panel).

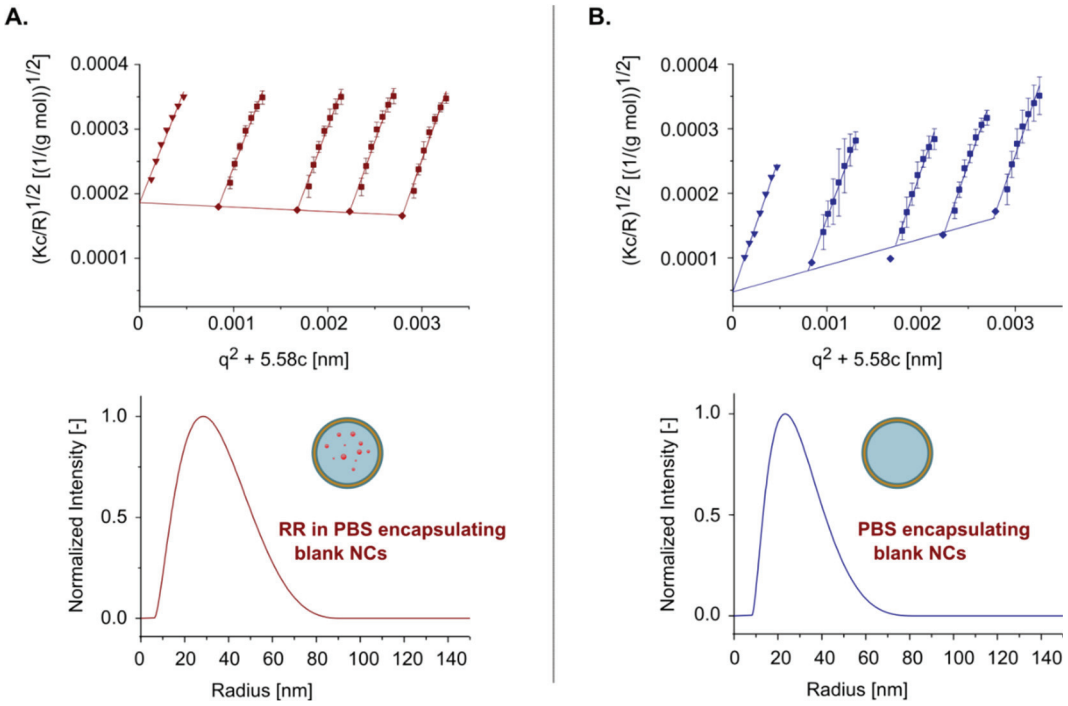

Figure 2.11 Combined laser light studies *via* SLS and DLS. SLS derived Berry plots are constructed from the concentration and angular dependent scattering intensities (upper panel) and DLS data presented as intensity based hydrodynamic radii R_h distributions (lower panel) for **A.** blank 75 μM RR in PBS encapsulating NCs and **B.** blank PBS encapsulating NCs.

Table 2.1 Results from static and dynamic light scattering experiments performed on blank NCs encapsulating either 75 μM RR in PBS or pure PBS.

LS results	*dn/dc** [ml g^{-1}]	M_{NC} [10^6 g mol^{-1}]	B_2 [mol ml g^{-2}]	R_g [nm]	R_h [nm]	*P*** [-]	ρ [-]
RR encapsulating blank NCs	0.188	88.3 ± 2.1	9.757E-8 ± 1.234E-8	25.3 ± 0.3	28.6 ± 14.0	22100	0.88
PBS encapsulating blank NCs	0.188	71.5 ± 15.9	3.679E-7 ± 1.396E-7	26.5 ± 3.0	24.3 ± 10.4	17900	1.09

*Indices taken from [137]

**Aggregation number with M_n = 4000 Da of $PMOXA_4$-$PDMS_{44}$-$PMOXA_4$

The vesicular polymersome architecture causes the overall polymersome molecular center of mass to be located along the enclosing membrane and hence a $\rho = R_g/R_h$ ratio of 1 or very close to 1 is expected [149]. Both, the RR- ($\rho = 0.88$) and PBS-encapsulating blank NCs ($\rho = 1.09$) gave ρ values very close to theory (see Table 2.1). The NCs are further characterized by an M_w of 88.3 ± 2.1 MDa for the RR- and 71.5 ± 15.9 MDa for the PBS-encapsulating ones. Knowing the average molecular weight of one $PMOXA_4$-$PDMS_{44}$-$PMOXA_4$ chain (^{1}H NMR: M_n = 4000 Da) allows calculation of the aggregation number *p*, giving a value of 22100 polymer chains per RR-polymersome (under the simplifying assumption that the entire molecular weight of 88.3 MDa corresponds to the polymeric material, with a negligible contribution from encapsulated RR) and to 17900 polymer chains enclosing one PBS-polymersome. Furthermore, these measured values of M_w permitted the calculation of concentrations of the supramolecular polymersome in solution. 1 mg/ml stock solutions consequently contain 12 nM RR- and 14 nM PBS-encapsulating blank NCs.

In addition, SLS studies on RR-encapsulating NLS-NCs and PBS-encapsulating NLS-NCs were attempted. The refractive index increments *dn*/*dc* needed for SLS data analysis were therefore determined with a Reichert AR7 refractometer and yielded here 0.059 and respectively 0.051 in PBS. Such low *dn*/*dc* values however prohibit the reliable evaluation of the associated M_W, R_g and ρ values. Instead, the molecular parameters extracted for blank NCs are used

in the successive work as close assumption to describe the supramolecular composition of NLS-NCs. This allowed the determination of supramolecular concentration of the 1 mg/ml RR-encapsulating NLS-NC stock solution giving a value of 12 nM.

Subsequently the theoretical number of surface conjugated NLSs could be calculated. NLS-NCs comprised of 22100 polymers with 5 wt% of maleimide end-group functionalized $PMOXA_4$-$PDMS_{34}$-$PMOXA_4$ with 34 % active maleimide sites (Thesis section 2.2.3) can be conjugated with a maximum of 376 NLS surfaced tags per nanocarrier. The number of maleimide functionalities that are accessible for NLS conjugation was determined in the following Thesis section 2.4.5.

2.4.3 Encapsulating nucleus-destined cargo compounds

Next, the ability of NLS-NCs to structurally incorporate cargo moieties for direct nuclear delivery was assessed. Bodipy and RR were used as fluorescent model payloads to make the NCs amenable for characterizations by dual color lifetime corrected fluorescence cross-correlation spectroscopy (FLCCS). FCCS and FLCCS are widely-used techniques to study molecular interactions and well-established methods, protocols and guidelines can be found in literature [150-152]. Lifetime correction was implemented to ensure high accuracy of the obtained FCCS measurement results. A detailed overview of the applied lifetime correction procedure will be given in Appendix 6.1.2.

For the NC structures developed here, it is proposed that the lipophilic Bodipy is intercalated into the NC membrane whilst the hydrophilic RR is located within the NC lumen. Hence, the polarity of the cargoes drives their local segregation within the carrier structure capturing them within the same particle for ensuing nuclear translocation. In practice, NC co-encapsulation with the two cargo moieties was achieved in two steps. First, hydrophilic RR was entrapped

within the inner aqueous cavity during the vesicle forming rehydration process (Thesis section 2.3). Second, 200 nM of lipophilic Bodipy was added to 0.5 mg/ml of the preformed RR encapsulating polymer vesicles and spontaneously intercalated into the membranes. Co-localization of the cargoes was then analyzed by dcFLCCS on 0.02 mg/ml NLS-NCs ($M_{NLS\text{-}NC}$≈ 88 MDa; n = 0.24 nM), detecting the red RR and the far-red Bodipy fluorescence emission in two separate channels. This yielded two characteristic fluorescence intensity time traces that were lifetime corrected, converted into channel specific auto-correlation (AC) functions $G_{AC}(\tau)$ and subject to further quantitative analysis.

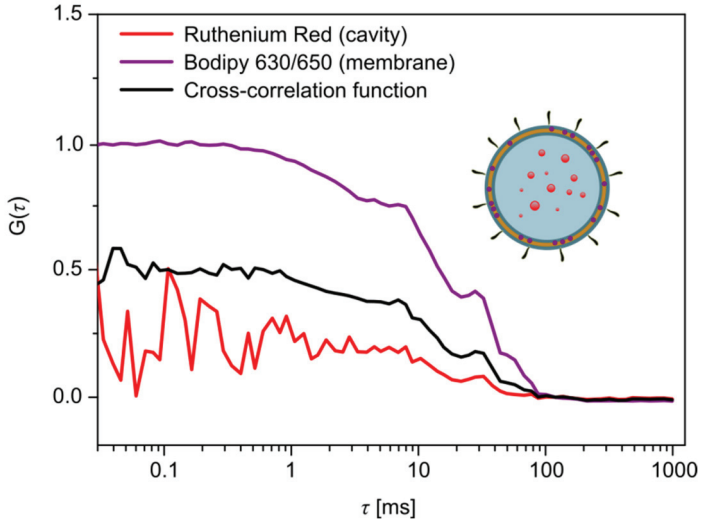

Figure 2.12 NC co-encapsulation with two model cargoes *via* dcFLCCS. The encapsulation of Ruthenium Red (red curve) and together with Bodipy 630/650 (purple curve) is demonstrated by the high cross-correlation amplitude (black curve).

Figure 2.12 shows that NCs exhibit the late-decaying AC functions typical for large and slowly-diffusing polymersomes, with the RR signal converted into the red AC curve and the Bodipy signal into the purple AC curve.

Both ACs were fit with a one component model equation of three-dimensional diffusion that contains a "triplet term" and a "diffusional term"

$$G(\tau)_{3D} = G(0)\underbrace{\frac{(1-T+Te^{-\frac{\tau}{\tau_T}})}{(1-T)}}_{G(\tau)_{triplet}}\underbrace{\frac{1}{1+(\frac{\tau}{\tau_D})}\sqrt{\frac{1}{1+(\frac{\tau}{\tau_D})S^2}}}_{G(\tau)_{diffusion}} \quad \text{(eq. 2.1)}$$

where τ_T depicts the characteristic triplet relaxation time and *T* the fractional triplet contribution to the total AC amplitude. The structural parameter is defined as $S = \omega_z/\omega_{xy}$ and the diffusion time as $\tau_D = \omega_{xy}^2/4D$. Consequently, the hydrodynamic radius R_h of the studied fluorescent NCs can be derived from the diffusion constant *D* in accordance with the Stokes-Einstein law:

$$D = \frac{k_B T}{6\pi\eta R_h} \quad \text{(eq. 2.2)}$$

with k_B being the Boltzmann constant, *T* the measurement temperature and η the dispersant viscosity.

A first indication for NC co-encapsulation of the two cargo-compounds was given by the diffusional behavior of the measured sample. Encapsulated cargoes should exhibit the same diffusion time as their host NC and consequently, RR and Bodipy are both expected to diffuse at the same rate when integrated into the same NC structure. Fitting the AC of RR showed that the fluorophore has a *D* of 7.6 ± 3 3 μm^2/s, corresponding to an R_h of 31.9 ± 18.4 nm. The AC of Bodipy was fit to a similar *D* of 5.8 ± 0.3 μm^2/s corresponding to an R_h of 39.7 ± 2.3 nm. A second indication of NC co-encapsulation was derived by cross-correlating the fluorescence fluctuation traces of the two detection channels. Both AC functions evidently follow similar decay patterns and consequently resulted here in a high cross-correlation amplitude.

Overall, the dcFLCCS measurements demonstrated that both model payloads are integral NLS-NC constituents, co-located within the same carrier structures.

NC incorporated cargo compounds are protected against exogenous agents that may cause, for example, premature chemical modification or enzymatic degradation, and can therefore be delivered into cell nuclei in their active form.

2.4.4 Bodipy interaction with the NLS-NC composite elements

Bodipy - as lipophilic cargo - is added to the nuclei targeting NLS-NCs after the polymersome formation and NLS conjugation process. Therefore, the question arose: with which NLS-NC components does Bodipy interact? To address this, the environment of encapsulated Bodipy was investigated by fluorescence lifetime spectroscopy, to identify whether it was in free solution or intercalated into the membrane.

The fluorescence lifetime τ is inverse of the first-order decay constant for the population of the excited state in fluorescence, and is therefore a measure of the time a fluorophore spends in the exited state before it returns back to the ground state by emitting a photon [153], or by other non-radiative processes. The electron relaxation rate is dependent on the fluorophore's chemical environment and was used here to sense the Bodipy interaction with individual NLS-NC components. To do so, in a first sample 200 nM Bodipy was mixed with 0.5 mg/ml NLS-NCs and in a second sample 200 nM Bodipy was mixed with 0.5 mg/ml blank NCs. After 30 minutes incubation, the polymersome samples were purified through SEC and diluted to 0.02 mg/ml. In addition, solutions of 1 nM free Bodipy, and 1 nM free Bodipy mixed with 1 nM free NLS, were prepared in PBS buffer. Fluorescence decay curves, consisting of photon counts as a function of time after a laser pulse were recorded for the Bodipy using a time-correlated-single-photon-counting (TCSPC) unit and analyzed to obtain τ values as outlined in Appendix 6.1.2.

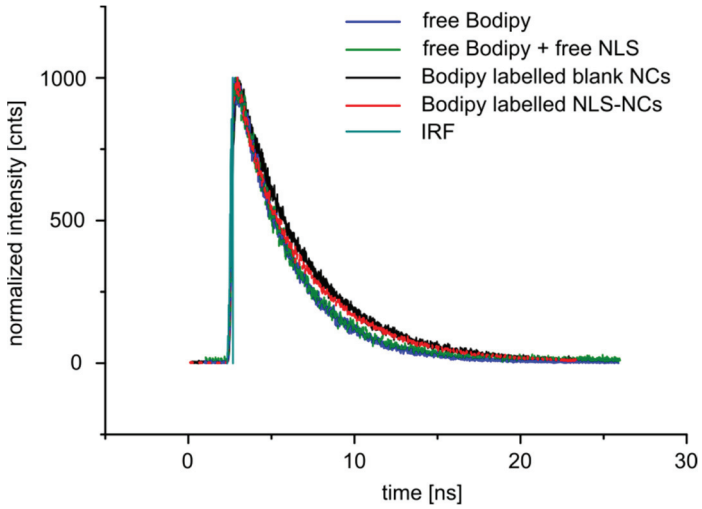

Figure 2.13 Fluorescence decay curves for Bodipy in different environments by TCSPC. Different fluorescence lifetimes indicate different chemical environments, and comparison of lifetimes can identify the environment of Bodipy within the NLS-NCs.

Table 2.2 Fluorescence lifetimes of Bodipy with respect to the fluorophore's chemical environment and its binding and interaction state.

	TCSPC Radiative Decay Times	
	τ [ns]	A_{rel} [-]
free Bodipy	4.22 ± 0.01	1
free Bodipy + free NLS	4.20 ± 0.01	1
Bodipy labelled blank NCs	4.38 ± 0.01	0.784 ± 0.006
	1.30 ± 0.02	0.217 ± 0.006
Bodipy labelled NLS-NCs	4.28 ± 0.02	0.881 ± 0.006
	1.02 ± 0.09	0.120 ± 0.006

Free Bodipy and free Bodipy mixed with free NLS showed very similar fluorescence lifetimes (Figure 2.13), 4.22 ± 0.01 ns in the absence of NLS and 4.20 ± 0.01 ns in the presence of NLS. Therefore, there is no evidence that Bodipy and NLS interact with one another. Bodipy labelled blank NCs exhibited fluorescence decay curves that could be fitted to two lifetimes, one of 4.38 ± 0.01 ns and a second of 1.30 ± 0.02 ns, that are respectively significantly longer and shorter than that observed for free Bodipy. The fluorescence lifetime is typically shorter in polar environment because a large dipole moment of surrounding molecules can promote an energy transfer to the fluorophore [154]. The observed longer lifetimes can therefore be explained by Bodipy intercalation into the lipophilic part

of the $PMOXA_4$-$PDMS_{44}$-$PMOXA_4$ based polymersome membrane. The same behavior was found for Bodipy labelled NLS-NCs that as well exhibited two distinct lifetimes, one of 4.28 ± 0.02 ns and a second of 1.02 ± 0.09 ns. Consequently, NLS that is tagged to the surface does not interact non-specifically with Bodipy and most important, shows also not to hinder Bodipy intercalation into the NC membrane.

2.4.5 Surface conjugation degree with NLS signals

To assess the number of NLS sequences that can be linked to NC surface, a fluorescence correlation spectroscopy (FCS) binding assay was used. As described in the Thesis section 2.3, polymersome formation from 95 wt% $PMOXA_4$-$PDMS_{44}$-$PMOXA_4$ and 5 wt% maleimide functional $PMOXA_4$-$PDMS_{34}$-$PMOXA_4$ resulted NCs that are surface decorated with multiple reactive maleimide groups (Mal-NCs). As the NLS itself is not fluorescent, the green-emitting SAMSA fluorescein (ThermoFisher) was used as a probe to evaluate the number of surface accessible maleimide groups that could be conjugated to the NLS. To do so, the acetyl protected SAMSA was activated with base to its thiol-containing form (ThermoFisher protocol) and applied in 1.5:1 molar stoichiometry to the preformed Mal-NCs. This catalyst free thiol-ene 'click' reaction could proceed overnight and the resultant SAMSA-Mal-NC conjugates (hereafter SAMSA-NCs) were purified from unreacted SAMSA using SEC through a Sephadex G-25 column.

The number of SAMSA entities per Mal-NC was then measured by FCS using a Zeiss LSM 510-META/Confcor2 laser-scanning microscope equipped with an Argon2-laser. In total, 30 x 10 s long intensity fluctuation time traces *I(t)* were recorded for 0.24 nM SAMSA-NC in PBS, and separately for 2 nM free SAMSA in PBS. The AC of free SAMSA was fitted with a one component model equation 2.1. In contrast, the measured SAMSA-NCs contained a second component of free

SAMSA that remained in solution even after NC purification. Hence, the two-component fit model

$$G(\tau) = G^0 \left[\frac{(1-T+Te^{-\frac{\tau}{\tau_T}})}{(1-T)}\right] \cdot \left[\frac{f_b}{\left(1+\frac{\tau}{\tau_{D,b}}\right)\sqrt{1+\frac{\tau}{S^2\cdot\tau_{D,b}}}} + \frac{f_f}{\left(1+\frac{\tau}{\tau_{D,f}}\right)\sqrt{1+\frac{\tau}{S^2\cdot\tau_{D,f}}}}\right] \quad \text{(eq. 2.3)}$$

was applied to extract the respective fractions *f* of NC on-bound f_b and of free f_f SAMSA.

To identify free and NC-bound SAMSA, hydrodynamic radii R_h of the fluorescent species were calculated from their diffusion constants *D* by the Stokes-Einstein law (equation 2.2).

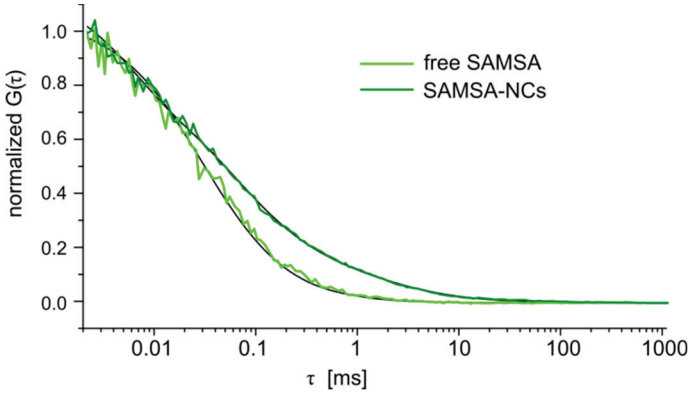

Figure 2.14 Normalized AC functions of free SAMSA fluorescein (lime curve) and of SAMSA-NC conjugates (dark green curve).

Table 2.3 Results from quantitative FCS measurements and respective AC fits for free SAMSA fluorescein and SAMSA-NC conjugates.

	D [µm²/s]	A_{rel} [-]	R_h [nm]	*CR* [kHz]	*N* [-]	*CPM* [kHz]
free SAMSA (1-component)	291.4 ± 39.5	1	0.8 ± 0.1	40.8 ± 8.1	28.1 ± 8.6	1.4 ± 0.3
SAMSA-NCs (2-components)	7.4 ± 2.5 271.5 ± 227.0	0.84 0.16	33.1 ± 8.4 0.9 ± 0.4	27.0 ± 5.9	0.6 ± 0.3 3.2 ± 1.7	37.5 ± 12.5 1.4 ± 0.3

The recorded intensity time traces were used to derive the number of Mal-NC conjugated SAMSA moieties by comparing the average brightness of a single SAMSA molecule to the average brightness of one SMASA-NC. To do this, values of counts-per-molecule (*CPM*) were calculated from the average count rate (*CR*)

for a sample, and the average number of molecules in the confocal volume for that sample. For SAMSA-NCs the overall *CR* of 20.1 ± 5.9 kHz is composed of contributions from both SAMSA moieties bound to the NC surface, and residual SAMSA molecules in free solution. The fractional *CR* signal contributions from these two species were determined by fitting the AC function (dark green curve in Figure 2.14) with the two-component model equation 2.3. On average 0.6 ± 0.3 SAMSA-NCs and 3.2 ± 1.7 free SAMSA molecules are present in the detection volume. The corresponding *CPMs* were calculated to 37.5 ± 12.5 kHz and 1.4 ± 0.3 kHz respectively and revealed here that 27 ± 9 SAMSA entities are linked to a single Mal-NC.

Comparing the theoretically calculated number of 376 maleimide linking sides per NC (Thesis section 2.4.2) with the experimentally determined one, shows that only 7 % has conjugated with the thiol-functional SAMSA. Such low conjugation efficacy might be related to hindered maleimide accessibility within the amphiphilic PMOXA-PDMS-PMOXA membrane. Nonetheless, the presence of 27 ± 9 maleimide groups per NC affords a sufficiently high number of sites available for the conjugation of the nuclear import facilitating NLS peptide. The average distance between two maleimide linking sites can be calculated to 8.5 ± 1.1 nm assuming here that all 27 ± 9 maleimide groups are evenly distributed across a 50 nm-diameter Mal-NC (with a calculated surface area of 1962.5 nm^2).

2.4.6 Surface charge

The surface charge of the NCs is expected to greatly influence their interactions in a cellular context. Zeta(ζ)-potential measurements were conducted to assess the surface charge of NLS-NC and blank NC. The 1.0 mg/ml polymersome stock dispersions in PBS were diluted 20-fold in Millipore water to reach a 25 μg/ml polymersome and < 10 mM salt concentration. Each sample was

measured three times on a Zetasizer Nano ZSP (Malvern Instruments Ltd UK) at 298 K and the average ζ-potential was determined.

In accordance with literature [155], pure $PMOXA_4$-$PDMS_{44}$-$PMOXA_4$ based blank NCs were found to have an average ζ-potential of 25.5 ± 9.4 mV due to their surface coverage with the positively charged polyamide functionalities of PMOXA. However, NC conjugation with the positively charged NLS-signals did not further increase, but rather decrease the ζ-potential of NLS-NCs to 18.7 ± 1.7 mV. Overall, both the NLS-NCs and blank NCs demonstrate a high positive ζ-potential.

Previously, particles with positive ζ-potential have been demonstrated to attach electrostatically to the cell's negatively charged plasma membrane, positioning them to be taken up into cells following endocytosis [106, 156]. In like manner, it is very probable that NLS-NCs and blank NCs actuate an electrostatically facilitated cellular uptake.

2.5 Materials and methods

2.5.1 Educts and solvents

PMOXA-PDMS-PMOXA **1** was synthesized from bifunctional carbinol-terminated PDMS (ABCR, code 116675, M_w = 5000 g/mol, ~ 65 repeat units, hydroxyethoxypropyl terminating end groups), triethylamine (Sigma-Aldrich , 99.5 %, CAS: 121-44-8, M_w = 101.19 g/mol, d = 0.726 g/cm^3), triflic acid anhydride (Fluka, TfsA ≥ 98.0 %, CAS: 358-223-6, M_w = 282.14 g/mol, d = 1.677 g/cm^3) and 2-methyl-2-oxazoline from (Sigma-Aldrich, 98 %, CAS: 1120-64-5, M_w = 85.10 g/mol, d = 1.005 g/cm^3). All the solvents used (anhydrous hexane, dichloromethane, acetonitrile, methanol, ethanol, and *d*-chloroform) were of the highest purity grade.

For the synthesis of the ***furan protected maleimide linker* 2***,* 3a,4,7,7a-tetrahydro-4,7-epoxysobenzofuran-1,3-dione was bought from Fluorochem (furan-maleic anhydride DA adduct, CAS: 5426-09-5, no purity declaration, M_w = 166.05 g/mol), 3-aminopropionic acid from Sigma (β-alanine, 99 %, CAS: 107-95-9, M_w = 89.09 g/mol) and anhydrous sodium carbonate (Na_2CO_3, 99.5 %, CAS: 497-19-8, M_w = 105.99 g/mol) from Acros Organics. The solvents used (methanol, dichloromethane, and aqueous 0.6 M HCl) were of the highest purity grade.

Mal-PMOXA$_4$-PDMS$_{34}$-PMOXA$_4$-Mal **3** was synthesized using the conjugation agents *N,N'*-Dicyclohexylcarbodiimide purchased from Aldrich (DCC, 99 %, CAS: 538-75-0, M_w = 206.33 g/mol) and 4-Dimethylaminopyridine from Aldrich (DMAP, ≥ 99 %, CAS: 1122-58-3, M_w = 122.17 g/mol). Solvents used for the synthesis (anhydrous CH_2Cl_2, EtOH, toluene) were purchased with highest purity grade.

2.5.2 Other consumables

NLS-NCs and ***blank NCs*** were extruded to 50 nm-diameter using polycarbonate membranes of 0.05 μm pore size (Whatman Nuclepore Track Etch Membrane) and purified by SEC through Sephadex G-25 columns (GE Healthcare Life Science HiTrap Desalting Column). In addition, NLS-NCs were conjugated with cysteine terminated bipartite nuclear localization sequences purchased from GenSkript (biNLSs, CWKRLVPQKQASVAKKKK, M_w = 2127 Da, Lot No: 91262870001/PE3665) and unreacted maleimide linking sites quenched with *L*-cysteine from Sigma-Aldrich (C, 97 %, CAS: 52-90-4, M_w = 121.16 g/mol).

2.5.3 Synthesis product characterization

Nuclear Magnetic Resonance (NMR) spectroscopy was used to record ^{1}H NMR spectra with 128 scans on a Bruker DPX-400 spectrometer in $CDCl_3$ without tetramethyl silane supplements. The spectra were phase corrected and a Whittaker Smoother applied to adjust the baseline prior to peak integration with *MestReNova* software (Mestrelab Research S.L., Spain). All spectra were aligned to the chemical shift of $CDCl_3$ at 7.26 ppm.

Gel Permeation Chromatography (GPC) traces were recorded on a WinGPC UniCrom device (V 8.20 - build 4815, Polymer Standard Service (PSS), Germany) that was calibrated against poly(methyl-methacrylate) standards in DMF. The GPC device was equipped with an Agilent Viscotek/Malvern mixed system composed of a 1100 series pump followed by an autosampler and a TDA 305 (RI, VWD, viscometer and 90° light scatter, Viscotek/Malvern) with a series of gram columns (pre-column (5 cm), 30 Å (30 cm) and two 103103 Å (30 cm), all 10 µm particles and 0.8 cm in diameter, PSS, Germany). The detectors and columns were kept at 60°C using DMF with 20 mM LiBr as eluent at a flow rate of 1 mL min^{-1}.

2.5.4 NC characterization

Transmission Electron Microscopy (TEM) was used to image the polymersomes on a Philips CM100 device operated at 100 kV acceleration voltage and equipped with a CCD-camera. The TEM samples were prepared on prehydrophilized carbon coated 400 mesh copper grids. Therefore, dilute polymersome solutions (5 µl of 0.2 mg/ml polymersomes) were deposited onto the copper grids and negatively staining with 2 % uranyl acetate. Size analysis was accomplished by ImageJ, taking at least 150 individual NC specimens for statistical evaluations.

Cryogenic Transmission Electron Microscopy (cryo-EM) samples were prepared from 1 mg/ml nanocarrier solutions. Therefore, 3 µl dispersion was dropped onto a carbon coated lacey copper grid. The mounted samples were blotted with a Gatan Cryo Plunge III to remove the supernatant without damaging the carbon layer. Samples were cooled down by liquid nitrogen and subsequently inserted into JEOL 2100 FEG microscope. The device was operated at 200 kV and cryo-EM images recorded with a Gatan 2kx2k UltraScan CCD camera.

Laser light scattering experiments were performed on a commercial Light Scattering Spectrometer (LS instruments) equipped with a 30 mW HeNe laser (wavelength 633 nm) and two parallel connected avalanche photomultiplier detectors (APDs). The detected count rate was set to 40 kHz applying an automatic laser intensity regulation function and potentially occurring APD afterpulsing effects were antagonized by pseudo cross-correlation between the signals detected in the two APDs. The scattering intensity of freshly extruded polymersomes was measured in dust free 10 mm high precision quartz cells, which were placed in an optically matching thermostat vat at 298 K.

Dual color Fluorescence Lifetime (Cross-)Correlation Spectroscopy (dcFL(C)CS) measurements were performed on an Olympus IX73 inverted microscope stand equipped with a 1.2 NA water immersion 60x superapochromat objective (UplaSApo, Olympus) and suitable emission and excitation band pass filters (Semrock and AHF). Two pulsed diode lasers (LDH-P-FA-530 and LDH-D-C-640, PicoQuant) were operated at 40 MHz for pulse interleaved excitation (PIE) dcFLCCS (Sepia II, PicoQuant). Emitted photons were detected in two separated channels coupled with two single-photon avalanche detectors (SPCM CD3516H, Excelitas). A time correlated single photon counting (TCSPC; 16 ps resolution, HydraHarp 400) unit was used to generate photon arrival time histograms known as fluorescence lifetime spectra. The laser powers were set to 20 µW for the

530-laser (except free RR dissolved in PBS was measured at 30 μW due to its very low fluorescence quantum yield) and to 17 μW for the 640-laser. Intensity fluctuation traces were then recorded for 120 s with a maximum correlation integration time τ of 2 s. The measurements were performed 20 μm away from the coverslip within previously calibrated confocal volumes from free dyes of known diffusion constants *D*. Here, Rhodamine B with a *D* of 426.4 $\mu m^2/s$ at 298 K and Atto-655 NHS-ester with a *D* of 403.6 $\mu m^2/s$ at 298 K were used for 530 nm and 640 nm diode lasers, respectively. The structural parameter was in both channels set to 4 and the maximal cross-correlation was derived to be 92 % based on the overlap estimation of the two illumination areas from calibration bead measurements.

Fluorescence Correlation Spectroscopy (FCS) measurements were conducted on a Zeiss LSM 510-META/Confcor2 laser-scanning microscope, equipped with an Argon2-laser (488 nm) and operated at 17 μW laser power. A 40x water-immersion objective (Zeiss C/Apochromat 40X, NA 1.2) and appropriate band pass 505 – 550 nm filters were used, and the pinhole adjusted to 70 μm with 5 % excitation transmission. The confocal volume was calibrated with Oregon Green 488 of known diffusion constant *D* of 411 $\mu m^2/s$ at 298 K [157].

Zeta potential measurements were performed on a Zetasizer Nano ZSP (Malvern Instruments Ltd UK) at 298 K. NLS-NC and blank NC dispersions of 0.5 mg/ml were diluted 20-fold in Millipore water to 25 μg/ml and < 10 mM salt concentration. Each sample was measured in triplicates to determine the average ζ-potential.

Chapter 3

Nucleocytoplasmic transport steps of NLS-NCs *in vitro*

Thesis chapter contributions

Dr. L. P. Zweifel (Research associate at University of Basel): Collaborative dcFLCCS titration-assay design, data analysis, and modeling of Kap to NLS-NC binding interactions.

Dr. L. Kapinos-Schneider (Research associate at University of Basel): Collaborative design of the SPR titration-assay. Analysis and interpretation of SPR data.

C. Rencurel (Technical associate at University of Basel): Expression and purification of Kaps, Nups and Ran proteins.

3 Nucleocytoplasmic transport steps of NLS-NCs *in vitro*

3.1 Introduction

The here developed NLS-NCs are designed to mimic the cargoes intrinsic to the cell, and so to exploit the existing biological mechanism of efficient nuclear import. To study the binding interactions underlying this process in living cells remains however a formidable challenge. This chapter will therefore investigate the potential for biofunctionality of NLS-conjugated NCs by reconstituting the necessary mechanistic steps in their nuclear-cytoplasmic translocation *in vitro* on simplified systems at a single-molecule or ensemble level.

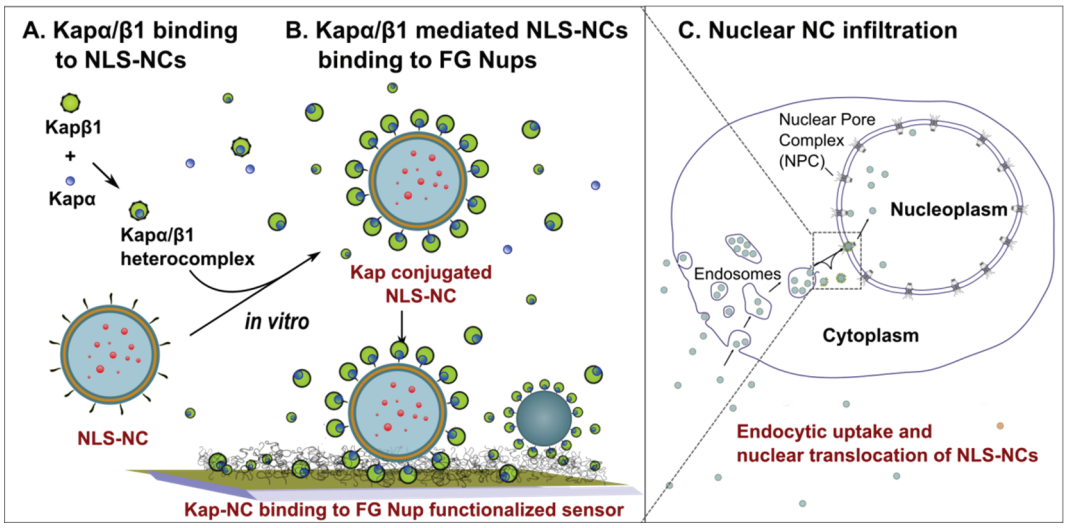

Figure 3.1 NLS-NCs are facilitating a selective nuclear import. A. The recognition of NLS-NCs as authentic nuclear cargoes by Kapα/β1 transport receptors is investigated *via* dual-colour fluorescence lifetime cross-correlation spectroscopy (dcFLCCS) and **B.** the subsequent Kap mediated FG Nup binding of the formed Kapα/β1•NLS-NC complexes studied *via* surface plasmon resonance spectroscopy (SPR). **C.** NLS-NC conjugation with Kapα/β1 complexes promotes the NPC barrier transcendence and eventually facilitates the nuclear infiltration.

Dual-colour fluorescence lifetime cross-correlation spectroscopy (dcFLCCS) was chosen to investigate the NLS-NC avidity towards Kapα/β1 on a single

molecular level (Figure 3.1 A). This method allowed not only to testify the biofunctionality of the NCs, but also enabled determination of the number of Kapα/β1 that can bind to a single NLS-NC, and measurement of the equilibrium dissociation constant K_D for that interaction. The NCs were visualized by transmission electron microscopy (TEM) before and after their surface coating with Kapα/β1 to ensure they remain structurally intact, and to determine the precise size of the Kapα/β1•NLS-NC complexes. In this respect, it was further examined whether their dimensions would permit them to cross the NPC gating channel. The affinity and kinetics of binding of the Kapα/β1•NLS-NC complex to selected FG Nup types were assessed using surface plasmon resonance (SPR) spectroscopy (Figure 3.1 B).

More specifically, the potential for diffusion of the Kapα/β1•NLS-NC complex along the Nup constituting NPC channels (Figure 3.1 C) was evaluated based on its binding affinity for the cytoplasmic periphery Nup214 [158], the central channel Nup98 [159] and the nuclear basket Nup153 [160]. The potential for release of the associated Kapα/β1•NLS-NC complex from the Nup-layers was assessed by measuring the effect of incubating the complex with RanGTP on the binding affinity to FG Nups (amongst others to the nuclear basket Nup153).

In order to demonstrate that any interactions favoring nuclear transport resulted from the NLS sequence, all measurements were also carried out on blank NCs (*i.e.* polymersomes that lack the NLS peptide required for Kapα/β1 binding).

3.2 Kap binding to NC surface exposed NLSs

Kaps typically exhibit high binding affinity towards NLS epitopes and association occurs already in the sub-nanomolar concentration range [161]. In order to assess binding at such low concentrations, dual color fluorescence lifetime cross-correlation spectroscopy (dcFLCCS) was selected to study the multivalent attachment of Kap transporters to NLS-NCs on a single-molecular level [162, 163]. The biofunctionality of the NLS-NCs was assessed in terms of presence and strength of the NLS•Kap interaction, which is essential for nuclear transportation. Both, the average number of Kaps conjugating to a single NLS-NC and binding affinity of Kaps for the conjugated NLS sequence were measured. Finally, transmission electron microscopic (TEM) measurements were conducted to obtain insight into the morphology of NLS-NCs before and after Kapα/β1 binding.

3.2.1 Theoretical background to FCS/FCCS binding studies

Fluorescence correlation spectroscopy (FCS) [164, 165] and fluorescence cross-correlation spectroscopy (FCCS) [166] have been widely used to investigate protein binding to ligand functionalized nanoparticles (NP).

In single-color FCS [167-169], binding is monitored based on the diffusional behavior of one of the binding partners in its free and in its bound state. It is common practice to analyze the behavior of the fast-diffusing protein, which upon binding substantially changes its diffusional behavior, exhibiting the reduced mobility of the much larger and hence slower diffusing NP. In contrast, the NPs undergo only minor mobility changes upon protein association due to a negligible increase in their mass and radius. FCS binding studies rely on the detection and discrimination of two species with distinct diffusion constants. Fractions and

concentrations of bound and unbound proteins are commonly extracted from auto-correlation (AC) function amplitudes using two-component diffusion models. Although single-color FCS is experimentally straightforward, a drawback of the method is that it is not always possible to distinguish a slowing of protein diffusion due to non-specific aggregation from that caused by specific binding of the protein to NPs.

Dual-color FCCS is an extension to the single-color FCS method [166, 170]. It circumvents the limitation of distinguishing binding specificity by monitoring and correlating the fluorescence intensity fluctuations of two interacting fluorescent binding partners. If the two bind to each other, then they move together through the detection volume and hence their fluorescence intensity fluctuations are correlated (coincident in time). Their dynamic co-localization is used to quantify the degree of binding based on the signal cross-correlation amplitude [152, 171]. FCCS experiments usually utilize spectrally-separated fluorophores that are excited with two distinct laser lines, and the emitted intensity fluctuations are typically measured with two detectors with appropriate wavelength-selective filters. Although FCCS is the more accurate method, most measurements still suffer from false-positive and false-negative cross-correlation artefact due to an inter-channel cross-talk or the lack of overlap in detection volumes for different colors due to chromatic aberrations [150]. Lifetime correction can essentially be used as an integral part to conventional FCCS and thereby cross-correlation artefacts excluded (see article [172] and [173] for characteristics and technical applications of fluorophore lifetimes). Since it offered considerable advantages and suitable instrumentation was available, dual-colour fluorescence lifetime cross-correlation spectroscopy (dcFLCCS) was used in preference to single-color FCS to study the binding of Kapα/β1 complexes to NLS-NCs.

3.2.2 dcFLCCS titration assay

A dcFLCCS titration was conducted to study the Kapα/β1 complex binding to NLS-NCs. The assay was carried out in PBS containing 200 nM Kapα and 20 nM Kapβ1, with only 2 nM of Atto-550 succinimidyl ester (Atto-550 NHS-ester or simply Atto-550) labelled Kapβ1 mixed with 18 nM non-labelled Kapβ1 so that the concentration of fluorescent Kapβ1 was sufficient to give good signal-to-noise in FCS measurements (*i.e.* the concentration was enough high to detect a sufficient signal but was not too high in order to detected sufficient intensity variations over time due to diffusion of single molecules in and out of the detection volume). The proportionally 10 fold higher Kapα concentration fosters complete complexation with all present Kapβ1 to yield 2 nM labelled and 18 nM non-labelled Kapα/β1 heterodimers [35]. In parallel, 0.5 mg/ml NLS-NCs ($M_{NLS\text{-}NC}$≈ 88 MDa; n = 6.0 nM, see Thesis section 2.3 for preparation details) were labelled with 200 nM Bodipy 630/650 (hereafter Bodipy). Increasing concentrations of 0, 0.046, 0.092, 0.138, 0.230, 0.345, 0.455 and 0.585 nM NLS-NCs were titrated against the 20 nM Kapα/β1 complex and the dcFLCCS data were measured for each titration step after 30 min incubation time to assess the binding equilibrium. Fluorescence intensity time traces were recorded for both the Atto-550 labelled Kapβ1 and the Bodipy labelled NLS-NCs, using the same PicoQuant MT200 system as described in Thesis section 2.5.4. Fluorescence for Atto-550 labelled Kapβ1 was excited with a pulsed 530 nm laser and referred to as the "red channel" in future discussions. Bodipy was exited with a pulsed 640 nm laser and referred to as the "far-red channel". The time between an individual laser pulse and the detection of a photon was measured on-line at ps resolution, using a system integrated time correlated single photon counting (TCSPC) unit. The fluorescence lifetimes present in the sample can be extracted by analyzing the decay of photon counts over time after the laser pulse, for a large number of photon counts. In addition to measuring the time between a laser pulse and the detection of a photon, the system also

records the detection time of each photon on the timescale of the whole experiment. This latter information allows the construction of auto-correlation and cross-correlation functions on any timescale that the user desires. For statistical binding analysis, 120 s long time traces were taken with a maximum correlation integration time τ of 2 s. Each measurement was repeated in three independent runs and the obtained data analyzed as outlined the following.

3.2.3 dcFLCCS data processing

To analyze the data of the dcFLCCS titration assay, first the TCSPC detected photon arrival times *I(t)* were plotted with SymPhoTime64 software and the resulted histograms fitted to multi-exponentials

$$I(t) = I_b + \sum_{i=0}^{n-1} \alpha_i exp\left(-\frac{t-t_0}{\tau_{L,i}}\right) \quad \text{(eq. 3.1)}$$

with α_i the amplitude and $\tau_{L,i}$ the fluorescence lifetime of the *i*-th component, I_b the non-decaying background intensity and t_0 the zero-time shift. In doing so, the fluorophore lifetime characteristics are obtained which (i) contain information about the binding or complexation state of the studied binding partners and (ii) were used to correct the fluorescence intensity time traces to remove parasitic signals (see Appendix 6.1.2 for detailed lifetime correction procedure).

Second, the corrected fluctuation time traces $F(t)$ were converted into corresponding auto-correlation (AC) $G_{AC}(\tau)$ and cross-correlation (CC) functions $G_{CC}(\tau)$ which can be written as follows:

$$G_{AC}(\tau) = \frac{\langle \delta F(t) \cdot \delta F(t+\tau) \rangle}{\langle F(t) \rangle^2} \quad \text{(eq. 3.2)}$$

$$G_{CC}(\tau) = \frac{\langle \delta F_r(t) \cdot \delta F_{fr}(t+\tau) \rangle}{\langle F_r \rangle \langle F_{fr} \rangle} \quad . \quad \text{(eq. 3.3)}$$

In the described context, angled brackets are denoting for the time averaged intensity over the entire acquisition time that are derived from the difference between the instantaneous and the mean recorded fluorescence. Whilst AC was

used to analyze the signal self-similarity within the individual channels, yielded the CC information about the similarity of the fluctuations of the signal in time between the two detection channels.

More specifically, the AC functions $G_{fr}(\tau)$ obtained in the far-red channel from the corrected intensity fluctuation time traces $\langle F_{fr} \rangle$ of Bodipy labelled NLS-NCs are described with a one-component model for objects freely diffusing in three dimensions, with the addition of a term to describe fluctuations in intensity arising from transition to the non-fluorescent triplet state. The equation therefore has both a "diffusional term" and a "triplet term" (in analogy to equation 2.1)

$$G_{fr}(\tau) = G_{fr}^{0} \cdot \frac{1+\frac{T \cdot e^{-\frac{\tau}{\tau_T}}}{1-T}}{\left(1+\frac{\tau}{\tau_D}\right)\sqrt{1+\frac{\tau}{S^2 \cdot \tau_D}}} \,. \qquad \text{(eq. 3.4)}$$

By fitting the AC function derived from the experimental data $G_{fr}(\tau)$ to this equation, one can obtain the diffusion time τ_D, and then the diffusion constant according to $\tau_D = \omega_{xy}^2/4D$, where ω_{xy} is the lateral radius of the confocal volume. The diffusion constant *D* can be used to calculate the hydrodynamic radius R_h of the fluorescent NCs using the Stokes-Einstein relation (in analogy to equation 2.2)

$$D = \frac{k_B T}{6\pi\eta R_h} \qquad \text{(eq. 3.5)}$$

with k_B being the Boltzmann constant, *T* the measurement temperature and η the dispersant viscosity.

Kapα/β1 binding to NLS-NCs was assessed in the red channel from the corrected intensity fluctuation time traces $\langle F_r \rangle$ of the Kapβ1-Atto-550 fluorescence signal. In this case, the AC function $G_r(\tau)$ was fitted with the two-component model:

$$G_r(\tau) = G_r^0 \left[\frac{(1-T+Te^{-\frac{\tau}{\tau_T}})}{(1-T)}\right] \cdot \left[\frac{f_b}{\left(1+\frac{\tau}{\tau_{D,b}}\right)\sqrt{1+\frac{\tau}{S^2 \cdot \tau_{D,b}}}} + \frac{f_f}{\left(1+\frac{\tau}{\tau_{D,f}}\right)\sqrt{1+\frac{\tau}{S^2 \cdot \tau_{D,f}}}}\right]. \qquad \text{(eq. 3.6)}$$

where one component accounts for Kapα/β1-Atto-550 complexes bound to NLS-NC and the other for unbound Kapα/β1-Atto-550 complexes. Their respective contributions are reflected in the fractional amplitudes of bound f_b and free f_f complexes in the AC function. The distribution of Kapα/β1-Atto-550 complexes shifts from mainly free (f_f) to mainly bound (f_b) as the equilibrium position changes during the titration.

Cross-correlation functions $G_{CC}(\tau)$ were fitted using a one-component model including only the NLS-NC component and no triplet relaxation

$$G_{CC}(\tau) = G_{CC}^{0} \frac{1}{1+(\frac{\tau}{\tau_D})} \sqrt{\frac{1}{1+(\frac{\tau}{\tau_D})S^2}} \ . \qquad \text{(eq. 3.7)}$$

3.2.4 dcFLCCS analysis of Kap binding to NLS-NCs

Next, the dcFLCCS data were used to determine whether Kapα/β1 and NLS-NCs do in fact bind to each other (Figure 3.2 A). Throughout the following section, this analysis makes use of the fluorescence lifetimes determined for each species (Figure 3.2 B and C) to produce lifetime-corrected AC functions (Figure 3.2 D and E) and cross-correlation functions.

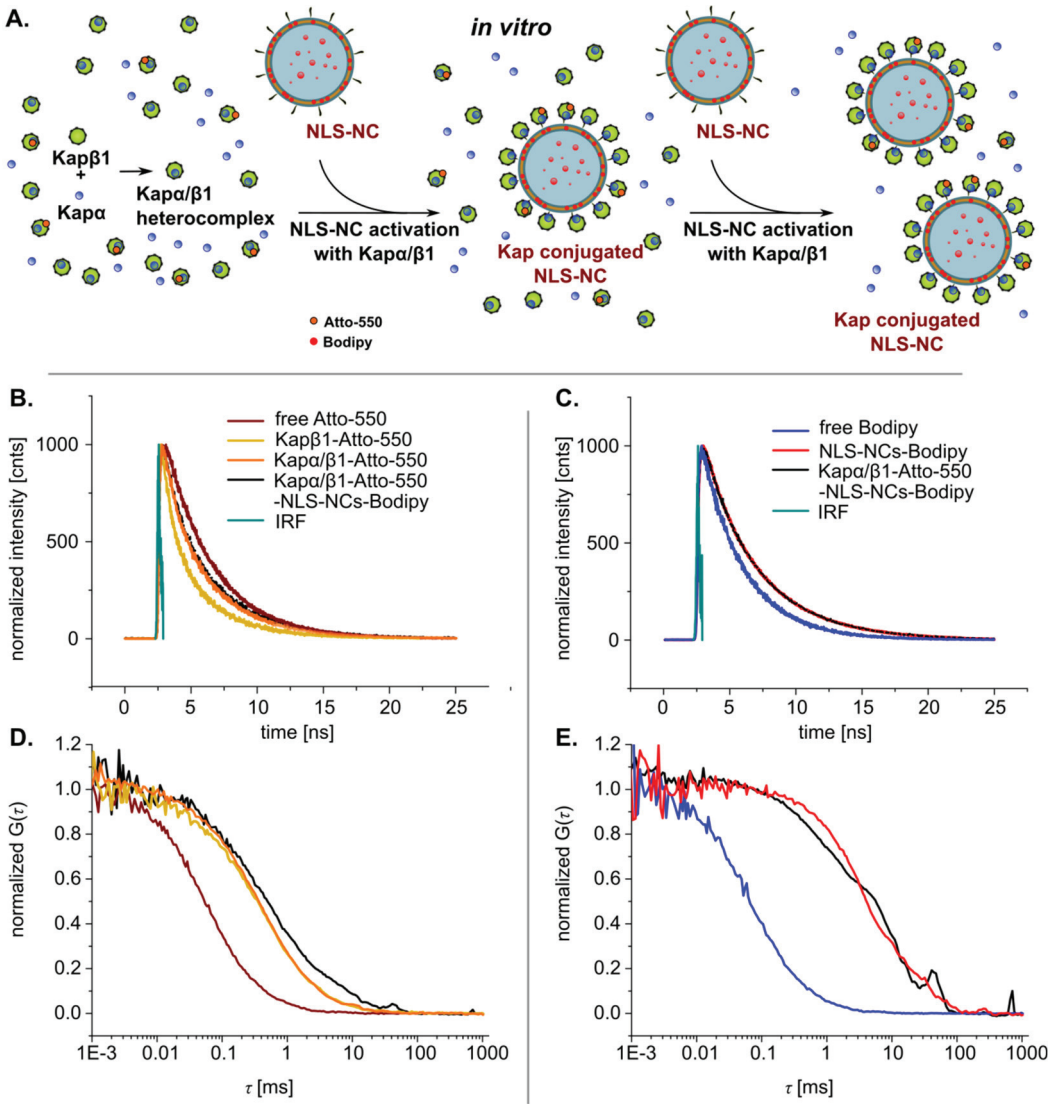

Figure 3.2 NLS-NCs are recognized by Kaps as authentic nuclear cargoes *in vitro*.A. Kapα together with Kapβ1 forms the heterodimer Kapα/β1 which as a complex is able to bind NLS on the NC surface. Here, the titration of increasing NLS-NC concentrations leads to a depletion of free Kapα/β1 in solution. The binding stoichiometry and dissociation constant for the interaction can be obtained from the dcFLCCS titration, by analyzing the dependence of the **B.** fluorescence lifetimes and **D.** diffusion times on Kapβ1-Atto-550 concentration. Complementary information about binding can be obtained from the data for the Bodipy **C.** lifetimes and **E.** diffusion times.

Table 3.1 Diffusional behavior and lifetime characteristics of Atto-550 and Bodipy in dependence of the experimental binding and complexation state *via* dcFLCCS and TCSPC analysis.

Time Resolved Fluorescence Spectroscopy		dcFLCCS Diffusional Behavior			TCSPC Fluorophore Lifetime	
		D [μm²/s]	A_{rel} [-]	R_h [nm]	τ_R [ns]	A_{rel} [-]
Red channel	Free Atto-550	341 ± 5.2	1	0.68 ± 0.01	3.60 ± 0.04	1
	Kapβ1-Atto-550	45.3 ± 1.6	1	5.1 ± 0.2	3.38 ± 0.03 0.95 ± 0.03	0.56 ± 0.01 0.44 ± 0.01
	Kapα/β1-Atto-550	43.3 ± 2.2	1	5.3 ± 0.3	3.74 ± 0.02 1.20 ± 0.05	0.73 ± 0.01 0.27 ± 0.01
	Kapα/β1-Atto-550 -NLS-NC-(Bodipy)	5.5 ± 1.5 46.6 ± 6.5	0.07 ± 0.02 0.93 ± 0.07	42.1 ± 9.0 5.0 ± 0.6	4.02 ± 0.04 1.40 ± 0.07	0.73 ± 0.01 0.27 ± 0.01
Far-red channel	Free Bodipy	373 ± 21.0	1	0.6 ± 0.0	3.98 ± 0.04	1
	NLS-NC-Bodipy	6.0 ± 0.5	1	38.3 ± 2.9	3.23 ± 0.01	1
	Kapα/β1-(Atto-550) -NLS-NC-Bodipy	5.9 ± 0.5	1	39.2 ± 2.8	3.30 ± 0.03	1

TCSPC recorded photon arrival time histograms were fitted to obtain one or more fluorescence lifetimes τ_R (see Appendix section 6.1.2 for fitting-procedure). Furthermore, the AC curves were analyzed to obtain diffusion constants and to calculate hydrodynamic radii R_h for the different fluorescent species in solution (see Thesis section 3.2.3 for fitting-procedure). In this regard, the red channel was used to monitor the lifetime and the diffusional behavior of the red-emitting Atto-550: (i) free in solution, (ii) covalently bound to Kapβ1-Atto-550, (iii) complexed in the Kapα/β1-Atto-550 heterodimer and (iv) associated in the Kapα/β1-Atto-550-NLS-NC-(Bodipy) complex. The far-red channel was used to monitor the lifetime and diffusional behavior for the far-red emitting Bodipy: (i) free in solution, (ii) intercalated within the membrane of uncomplexed NLS-NC and (iii) intercalated within the membrane of the NLS-NC that is part of the Kapα/β1-(Atto-550)-NLS-NC-Bodipy complex.

The fluorescence lifetimes τ_R were used to analyze the chemical environment of the fluorophores [174] giving direct information about a given binding state. The TCSPC histograms of free Atto-550 in PBS could be fitted with a single lifetime of 3.60 ± 0.04 ns (see Figure 3.2 B and Table 3.1). However, upon covalent conjugation with Kapβ1, two lifetimes were required to adequately fit the data, one of 3.38 ± 0.03 ns (relative amplitude A_{rel1} = 0.56 ± 0.01) that is similar to that of free Atto-550, and a second of 0.95 ± 0.03 ns (A_{rel2} = 0.44 ± 0.01). The non-covalent Kapα/β1-Atto-550 complex, also has two discrete lifetimes, a longer lifetime of 3.74 ± 0.02 ns (A_{rel1} = 0.73 ± 0.01) and a shorter lifetime of 1.19 ± 0.05 ns (A_{rel2} = 0.27 ± 0.01), which may reflect a change in the overall environment of the fluorophore molecules that affects both lifetimes observed for the Kapβ1-Atto-550 conjugate. It can be speculated that this lifetime shift is related to a conformational change in Kapβ1 which happens during complexation [28]. Furthermore, both Kapα/β1-Atto-550 lifetimes clearly increase upon NLS-NC binding to 4.02 ± 0.04 ns (A_{rel1} = 0.73 ± 0.01) and 1.40 ± 0.07 ns (A_{rel2} = 0.27 ± 0.01). Again, it can be speculated that conformational changes in Kapα/β1 shift the fluorophore's lifetimes upon complexation with the NLS-cargo [37]. Indeed, this lifetime shift indicates the NLS-NC recognition as nucleus-destined cargo and shows for the first time that this synthetic carrier - due to its encoded biofunctionality - is able to recruit Kaps. Accordingly, similar trends were found for Bodipy, which shows one discrete lifetime of 3.98 ± 0.04 ns free in PBS, then shifts to a shorter 3.23 ± 0.01 ns lifetime once intercalated in the polymeric NLS-NC membrane (see Figure 3.2 C). No significant lifetime change was observed after Kapα/β1 NLS association, indicating that the chemical environment of Bodipy remains unchanged, *i.e.* the dye stays intercalated within the NCs membrane when the NLS-NC forms a complex with Kapα/β1.

Next, binding interactions were investigated based on the mobility of the binding partners by comparing their diffusion constants *D* and hydrodynamic

radii R_h. AC function analysis showed here that covalent conjugation of Atto-550 to Kapβ1 reduces its *D* from 341 ± 5.2 to 40.0 ± 2.3 μm²/s whilst its R_h concomitantly increases from 0.68 ± 0.01 nm to 5.8 ± 0.1 nm (see Figure 3.2 D). The subsequent non-covalent complexation of Kapβ1-Atto-550 with Kapα alters *D* only slightly to 38.0 ± 3.6 μm²/s and therefore the R_h increases only slightly to 6.1 ± 0.5 nm. In the next step, a fractional Kapα/β1-Atto-550 association to NLS-NCs could be detected from the large decrease of *D* to 5.5 ± 1.5 μm²/s which corresponds to an R_h of 42.1 ± 9.0 nm for the Kapα/β1-Atto-550-associated NLS-NC complexes. However, a second fraction of unbound Kapα/β1-Atto-550 remained in solution that had a *D* of 46.6 ± 6.5 μm²/s and an R_h of 5.0 ± 0.6 nm. These findings were complemented by measurements of the mobility of Bodipy in free solution, compared with Bodipy intercalated in the NLS-NC membrane. A clear transition is seen from a high value of *D* 373 ± 21.0 μm²/s and small R_h 0.62 ± 0.03 nm to a much lower value of *D* 6.0 ± 0.5 μm²/s and a 38.3 ± 2.9 nm R_h. Binding of Kapα/β1 to NLS-NCs had a negligible effect on the diffusion of the NLS-NC with D 5.9 ± 0.5 μm²/s and R_h 39.2 ± 2.8 nm, values that are within error of those measured for NLS-NC alone.

3.2.5 Kap binding degree and dissociation constant to NLS-NCs

Having demonstrated Kap binding to NLS-NCs, further analysis of the cross-correlation data was used to obtain information about (i) how many Kaps bind to a single NLS-NC at saturation and (ii) what is the upper limit of the dissociation constant K_D for the interaction of Kaps with NLS-NCs. To achieve this, the dcFLCCS curves recorded at every titration step were analyzed quantitatively for Kapα/β1•NLS-NC binding using a method reported by *Krüger et al.* [175]. In outline, increasing concentrations of NLS-NCs in the range 0 – 0.585 nM were titrated against a constant concentration of 20 nM Kapα/β1, leading to a reduction in concentration of freely diffusing Kapα/β1 complexes ($C^{free}_{Kap\alpha/\beta1}$) in

solution. The fractional distributions of NLS-NC bound Kapα/β1 complexes $C_{\mathrm{Kap\alpha/\beta1 \bullet NLS-NC}}$ and free Kapα/β1 complexes $C_{Kap\alpha/\beta1}^{free}$ were assessed based on the measured relative CC amplitudes (*RCA*) [150]. The fraction of complex formation could be calculated from the initial amplitude of the cross-correlation function G_{CC}^{0} and the initial amplitude in the AC function for the far-red channel G_{fr}^{0} (signal from the Bodipy-labelled NLS-NCs) as follows (see Table 3.2):

$$RCA = \frac{G_{CC}^{0}}{G_{fr}^{0}} = \frac{C_{\mathrm{Kap\alpha/\beta1 \bullet NLS-NC}}}{C_{Kap\alpha/\beta1}^{0}} \qquad \text{(eq. 3.8)}$$

The total Kapα/β1 concentration $C_{Kap\alpha/\beta1}^{0}$ was determined by spectrophotometry (Nanodrop 2000) before the titration assay. Plotting the fraction bound against the titrated concentration of NLS-NCs (C_{NLS-NC}) yielded a curve with the sharp breakpoint characteristic of an interaction where the concentration of the constant species in the titration is much higher than the K_D (black squares, Figure 3.3 B).

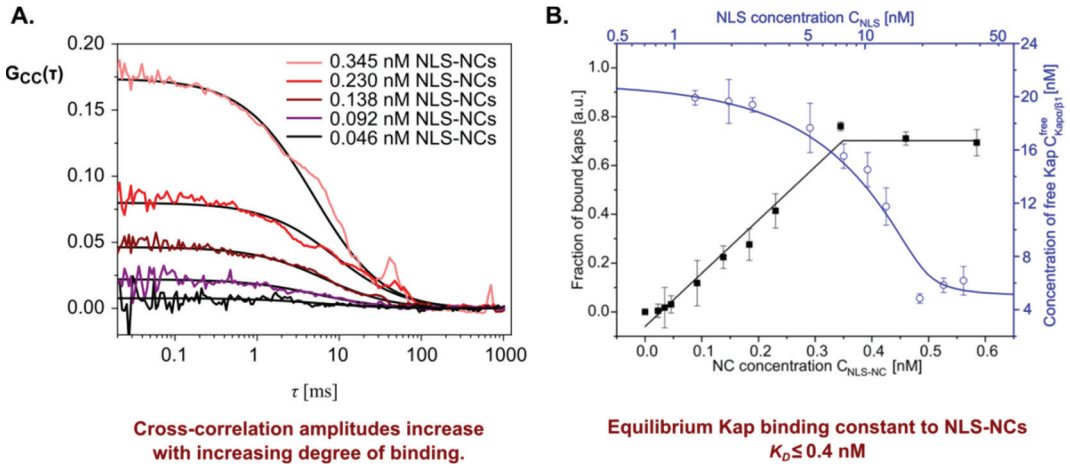

Figure 3.3 Kapα/β1 binding to NLS-NCs. A. The binding affinity of Kapα/β1 for NLS-NCs was assessed by dcFLCCS. Increasing concentrations of NLS-NCs were titrated against 20 nM Kapβ1 and 200 nM Kapα. Signal cross-correlation $G_{CC}(\tau)$ increases due to the increasing degree of binding. **B.** Fitting the fraction of bound Kaps (black squares) obtained from the relative cross-correlation amplitude to the equations described below (best fit curve shown as a black line) yields 57 ± 3 Kapα/β1 complexes per NLS-NC with $K_D \leq 0.4$ nM. The drop in free Kapα/β1 concentration (blue circles) is accurately simulated (blue line) based on the assumption that the maximum number of bound Kapα/β1 complexes per NLS-NC is equal to the number of NLS peptides competent for binding per NC.

Table 3.2 Quantitative Kapα/β1 binding to NLS-NCs *via* dcFLCCS titration curve analysis. Here, cross-correlation curves $G_{CC}(\tau)$ were analyzed to obtain Kapα/β1•NLS-NC complex diffusion constants *D* and hydrodynamic radii R_h. Additionally, from the initial amplitudes of the far-red auto-correlation G_{fr}^0 and the cross-correlation G_{CC}^0functions, the free Kapα/β1 concentration $C_{Kapα/β1}^{free}$ and hence the fraction of complexation could be calculated using equation 3.12.

C_{NLS-NC} [nM]	D [μm²/s]	R_h [nm]	G_{fr}^0 [-]	G_{CC}^0 [-]	$C_{Kapα/β1}^{free}$ [nM]
0	-	-	0	0	20 ± 0
0.046	5.05 ± 0.00	45.7 ± 8.2	0.245 ± 0.023	0.006 ± 0.003	19.39 ± 0.54
0.092	5.95 ± 0.26	38.8 ± 1.7	0.176 ± 0.038	0.019 ± 0.034	17.65 ± 1.85
0.138	7.20 ± 1.04	32.1 ± 4.0	0.140 ± 0.026	0.029 ± 0.017	15.53 ± 0.92
0.184	6.33 ± 0.71	36.5 ± 3.7	0.194 ± 0.110	0.049 ± 0.097	14.51 ± 1.28
0.230	6.03 ± 0.50	38.3 ± 2.9	0.093 ± 0.022	0.036 ± 0.031	11.75 ± 1.40
0.345	6.90 ± 0.40	33.5 ± 1.8	0.119 ± 0.074	0.083 ± 0.080	4.84 ± 0.36
0.460	6.87 ± 0.46	33.6 ± 2.1	0.072 ± 0.022	0.047 ± 0.021	5.83 ± 0.54
0.585	6.82 ± 0.55	33.9 ± 2.5	0.027 ± 0.020	0.043 ± 0.035	6.18± 1.08

Assuming that the NLSs on the NLS-NC behave as multiple independent (non-cooperative) binding sites (each binding a single Kapα/β1 complex) and introducing correction parameters for concentration errors arising from titration inaccuracies and / or surface adsorption of protein and an upper limit for competent Kapα/β1 (U_L), the binding curve can be fit with [176]

$$T_E + U_L \cdot \frac{k \cdot C_{NLS-NC} + C_{Kapα/β1}^0 + K_d - \sqrt{\left(k \cdot C_{NLS-NC} + C_{Kapα/β1}^0 + K_d\right)^2 - 4 \cdot k \cdot C_{NLS-NC} \cdot C_{Kapα/β1}^0}}{2 \cdot C_{Kapα/β1}^0} \quad \text{(eq. 3.9)}$$

where *k* is the number of bound Kapα/β1 complexes per NLS-NC. The abrupt saturation of the binding curve suggests tight binding. Therefore, first the K_D of the Kapα/β1•NLS-NC interaction was fixed to 10^{-15} M and the other parameters were varied in the fit, giving *k* = 57 ± 3, T_E = -0.06 and U_L = 0.76 with an R^2 = 0.984. In a next step, *k* was fixed to 57 and an *F*-test analysis was performed to analyze the range values of K_D that could fit the data at or above a given statistical confidence level. This analysis showed that the upper limit of the 95 % confidence interval for K_D was 0.4 nM (black line, Figure 3.3 B), and that the lower limit could not be constrained by the data (as expected for a titration of a very high affinity interaction, where the concentration of the constant species cannot be further reduced because of detection limits).

Next, the fit parameters (k, K_D, T_E and U_L) were used to describe the dependence of freely diffusing Kapα/β1 complexes $C^{free}_{Kap\alpha/\beta1}$ on the NLS concentration. First the concentration of NLS sequences available for binding (C_{NLS}) can be related to the concentration of NLS-containing nanocarriers using the parameter k described above:

$$C_{NLS} = C_{NLS-NC} \cdot k. \qquad \text{(eq. 3.10)}$$

The total Kapα/β1 concentration equals the sum of free and NLS-NC bound Kapα/β1 until binding reaches saturation:

$$C^0_{Kap\alpha/\beta1} = C^{free}_{Kap\alpha/\beta1} + C_{NLS-NC} \cdot k = C^{free}_{Kap\alpha/\beta1} + C_{NLS} \qquad \text{(eq. 3.11)}$$

Calibration of the effective confocal volumes V_{eff} for each color through bead scans allows the concentration of freely diffusing Kapα/β1 complexes $C^{free}_{Kap\alpha/\beta1}$ to be calculated from the total Kapα/β1 concentration $C^0_{Kap\alpha/\beta1}$ based on the RCA:

$$\frac{G^0_{CC}}{G^0_{fr}} = \frac{V_{eff,fr}}{V_{eff,CC}} \frac{C^0_{Kap\alpha/\beta1} - C^{free}_{Kap\alpha/\beta1}}{C^0_{Kap\alpha/\beta1}} \qquad \text{(eq. 3.12)}$$

Finally, by combining equations 3.9, 3.10 and 3.11 it is possible to derive:

$$C^{free}_{Kap\alpha/\beta1} = \frac{V_{eff,CC}}{V_{eff,fr}} \cdot (1 - T_E) \cdot \left(C^0_{Kap\alpha/\beta1} - U_L \cdot \frac{C_{NLS} + C^0_{Kap\alpha/\beta1} + K_d - \sqrt{\left(C_{NLS} + C^0_{Kap\alpha/\beta1} + K_d\right)^2 - 4 \cdot C_{NLS} \cdot C^0_{Kap\alpha/\beta1}}}{2} \right) \qquad \text{(eq. 3.13)}$$

The dependency of the free Kapα/β1 concentration $C^{free}_{Kap\alpha/\beta1}$ on the titrated concentration of NLS C_{NLS} (blue circles, Figure 3.3 B) can then be simulated by equation 3.13 (blue line in Figure 3.3 B) using the obtained parameters $V_{eff,CC}$, $V_{eff,fr}$, K_D, T_E and U_L.

Diffusion constants D and the corresponding hydrodynamic radii R_h for the Kapα/β1•NLS-NC complex were calculated from the cross-correlation curves using equation 3.7 and 3.5 at each point in the titration and are given in Table 3.2.

To conclude, as the concentration of NLS-NC increases during the titration, so does the concentration of NLS available for Kapα/β1 binding (blue circles in Figure 3.3 B). This shifts the binding equilibrium towards NLS-NC bound Kapα/β1. As a result, the CC amplitudes increase after each titration step (Figure 3.3 A). Fitting the binding curve in Figure 3.3 B to the multiple independent binding sites model of equation 3.9 yields a maximal binding capacity of 57 Kaps per NLS-NC with an apparent binding affinity K_D 0.4 nM for Kapα/β1•NLS binding (black line Figure 3.3 B). This K_D value is significantly lower in comparison to literature ones ($K_D \approx 10$ nM) [161], and demonstrates elevated affinity most likely due to the high local NLS concentration on NC surface. This may lead to immediate rebinding of Kapα/ β1 heterodimers after dissociation, giving a lower apparent dissociation rate and therefore tighter binding.

3.2.6 Kap binding to NCs is NLS specific

Next it was tested whether the in the previous Thesis section observed binding of Kaps to NLS-NCs was dependent on the presence of conjugated NLS peptides. Therefore, control experiments were performed in the same way as the binding titration outlined before but with blank NCs (instead of NLS-NCs, Figure 3.4 B) mixed with Kapα/β1 and with NLS-NCs mixed with Atto-550 (instead of Kapα/β1-Atto-550, Figure 3.4 C).

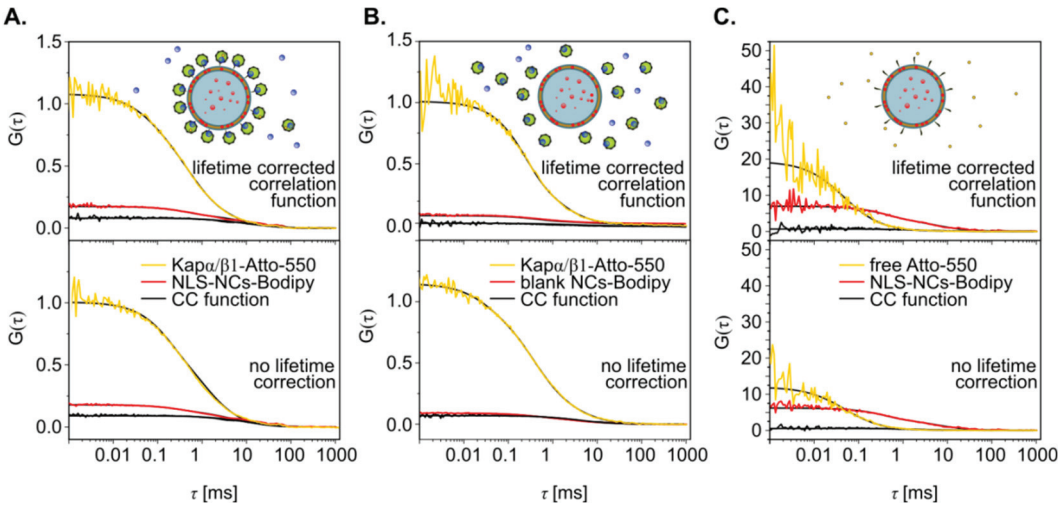

Figure 3.4 Comparing binding interactions based on dcFCCS AC and CC functions before and after lifetime correction. A. Atto-550 labelled Kapα/β1 complexes show substantial binding to Bodipy labelled NLS-NCs before and after lifetime correction. **B.** Lifetime correction of the AC and CC functions for Atto-550 labelled Kapα/β1 mixed with Bodipy labeled blank NCs shows that both do not non-specifically interact. **C.** Also, free Atto-550 mixed with Bodipy labelled NLS-NCs do not interact non-specifically.

Before lifetime correction was applied to the data, there was a non-negligible CC amplitude, suggesting that there was binding of Kapα/β1 to blank NLS-NCs. When lifetime correction was applied to the data, this CC amplitude disappeared. This suggests that it was an artifact arising from parasitic signals / cross-talk. Applying the same correction to the experiment with the NLS-NCs didn not remove the observed CC. It therefore results from genuine binding (Figure 3.4 A).

By the same method, there is no apparent binding of NLS-NCs to Atto-550, showing that the binding of Kap α/β1-Atto-550 to NLS-NCs is not only due to binding of Atto-550.

3.2.7 Size and morphology of Kap on-bound NLS-NCs

Morphology studies on NLS-NCs and blank NCs were performed using TEM to analyze how Kap treatment affects NC structural integrity and size. In addition, DLS was used as complementary method to support the TEM size-evaluations. For both methods, samples were prepared equivalently: 0.1 mg/ml NLS-NCs ($M \approx 88$ MDa; n = 1.2 nM, preparation details in Thesis section 2.3) or 0.1 mg/ml blank NCs ($M \approx 88$ MDa; n = 1.2 nM) were incubated with 100:1000 nM Kapβ1:Kapα. After 2 h, excess Kaps were removed by two rounds of dialysis against PBS, for 2 h each time. In parallel, dilutions of 0.1 mg/ml NLS-NCs or 0.1 mg/ml blank NCs in PBS were prepared without any additional Kaps. The nanocarriers were imaged on a Philips CM100 TEM operating at 100 kV and equipped with a CCD-camera. TEM specimens were prepared on pre-hydrophilized carbon-coated 400 mesh copper grids. NCs were deposited onto the grids and negatively stained with 2 % uranyl acetate. Size analysis was performed using ImageJ, taking at least 150 individual NC specimens for statistical size and size distribution evaluation. DLS measurements were performed on the same samples in accordance with the procedure described in Thesis section 2.4.2.

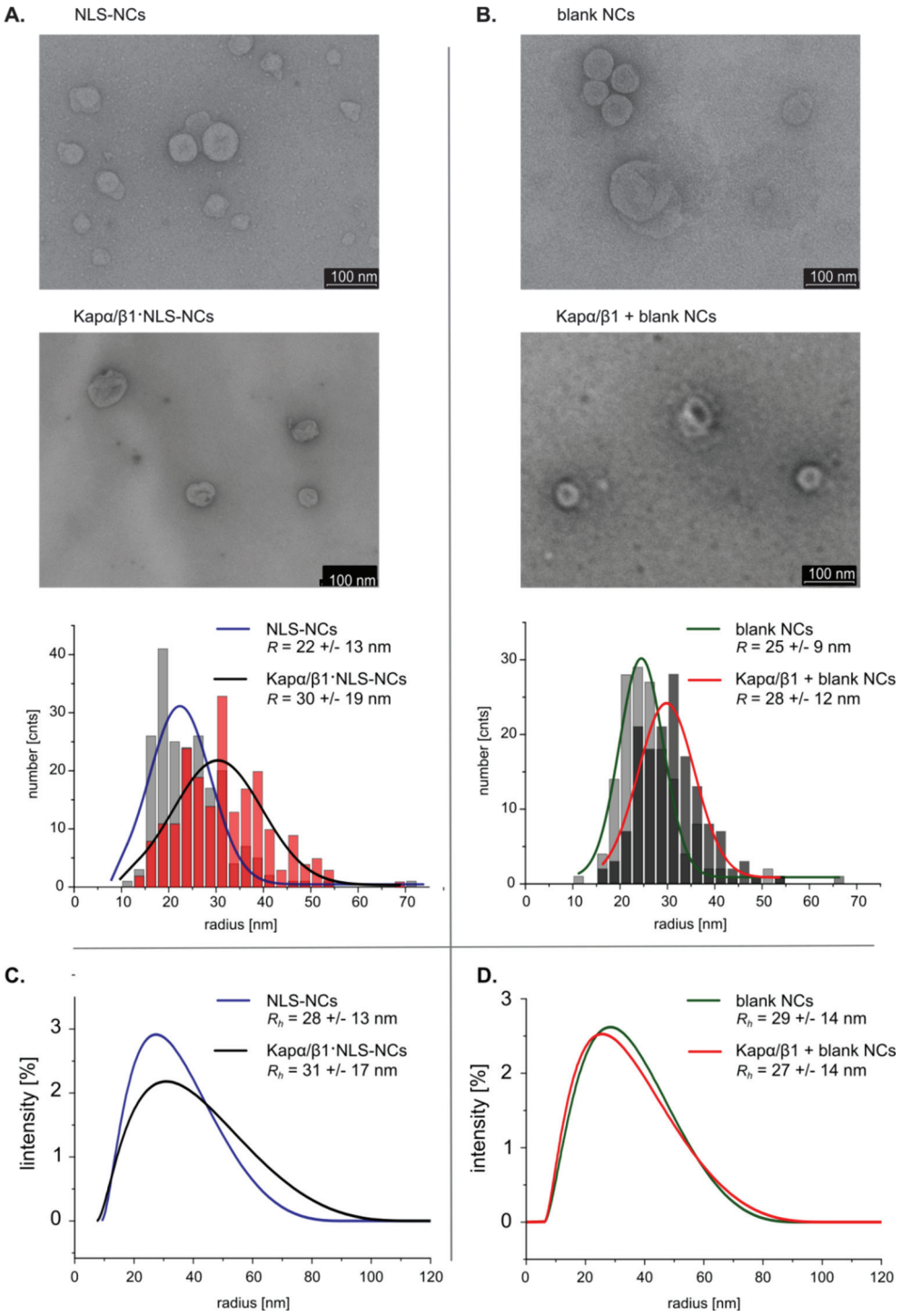

Figure 3.5 TEM micrographs with respective radii distribution histograms and DLS radii distribution curves before and after Kapα/β1 treatment of **A./ C.** NLS-NCs and **B./ D.** blank NCs.

TEM image analysis revealed here the typical shrunken and dented structures expected for well dispersed and non-aggregated polymersomes, for both NLS-NCs and blanks NCs, both before and after Kapα/β treatment (Figure 3.5 A and B). Statistical NC size evaluations of the untreated carriers showed that they have similar radii, $\bar{r}$ of 22 ± 13 nm for NLS-NCs (n = 203) and $\bar{r}$ of 25 ± 9 nm for blank NCs (n = 157), and that they are therefore comparable in size with the NPC channels that facilitate nuclear import (r ~ 25 – 40 nm [10, 11, 145], see also Thesis section 2.4.1 for a more detailed NC characterization by TEM). Kap conjugation to NLS-NCs did not affect the morphology of the carriers but significantly increases the overall NCs $\bar{r}$ to 30 ± 19 nm (n = 205). The difference can be attributed to a layer of Kapα/β1 complexes, whose diameter was determined before to 10.6 ± 0.6 nm by FLCS (see Table 3.1) consistent with values reported in literature [35]. DLS measurements further confirmed that association of Kapα/β1 with NLS-NC results in an increase in average hydrodynamic radius R_h from 28 ± 13 nm without conjugated Kaps to 31 ± 17 nm with conjugated Kaps (Figure 3.5 C). In contrast, blanks NCs were characterized with only slight increased radii of 28 ± 13 nm whilst treated with Kaps (TEM, n = 152) and nearly identical R_h distributions of 29 ± 14 nm before *vs*. 27 ± 14 nm after Kap treatment as determined by DLS (Figure 3.5 D).

3.3 Kap bound NLS-NCs are recognized by FG Nups

Multivalent interactions between Kaps and FG Nups promote facilitated diffusion in the NPC [35]. To assess whether this function was retained by Kaps bound to NLS-NCs, a surface plasmon resonance (SPR) binding assay (see Thesis section 3.4.3 for method details) was used to quantify the binding affinity of Kapα/β1•NLS-NC complexes to three different FG Nups (Nup98, Nup214 and Nup153, see Figure 3.6 A) and to compare it with the binding affinity exhibited by isolated Kapα/β1 complexes (Figure 3.6 B) [177].

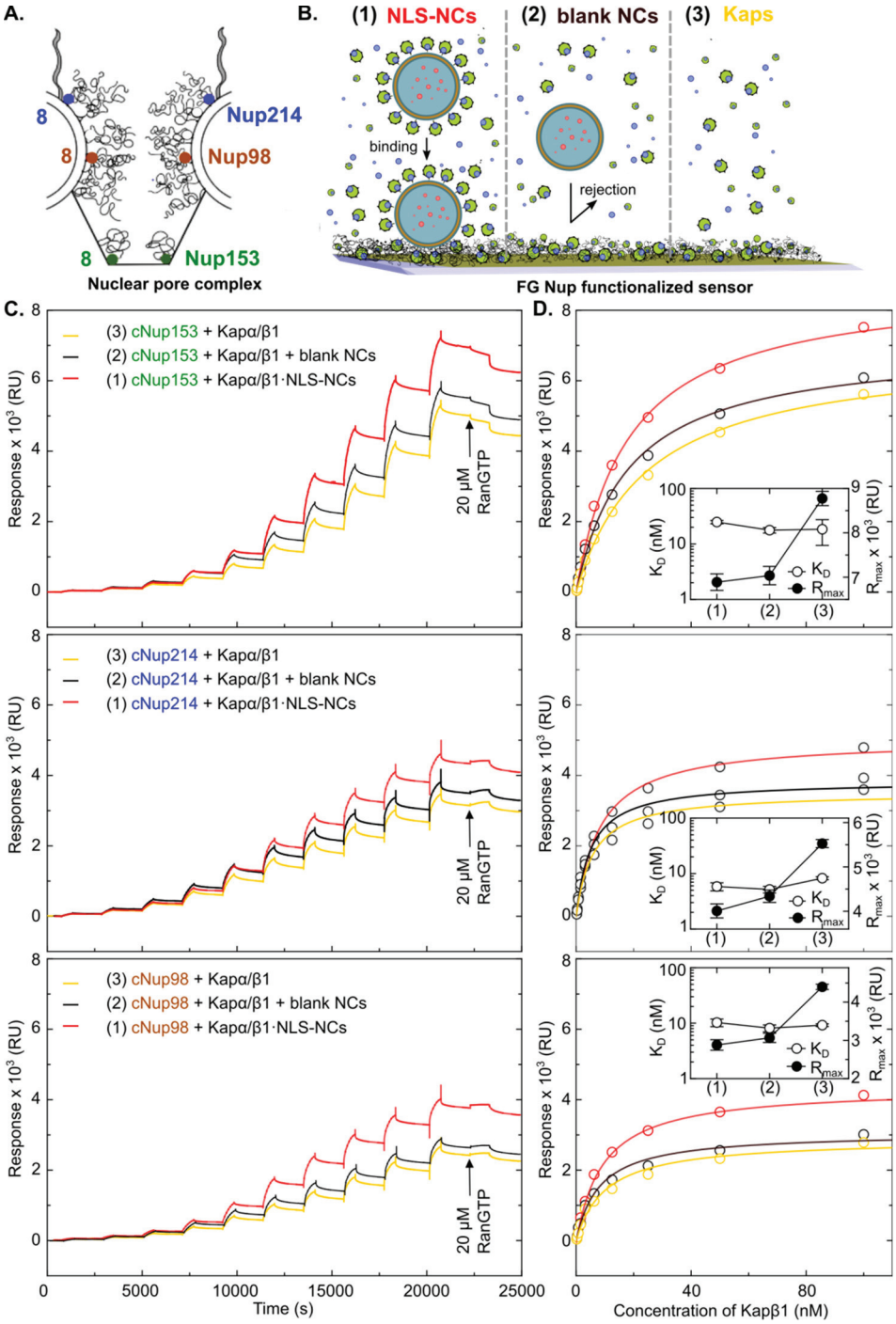

Figure 3.6 Kap bound NLS-NCs interact with FG Nups *in vitro*.A. Nucleoporins as the cytoplasmic filaments Nup214 (blue panel), the central channel Nup98 (brown panel) and the nuclear basket building Nup153 (green panel) are tethered together to form the NPC channel. **B.** Surface plasmon resonance (SPR) spectroscopy was used to investigate the bio-physical interactions of Kaps•NLS-NCs (1), blank NCs mixed with Kaps (2) and standalone Kaps (3) towards FG Nup functionalized sensors *in vitro.* **C.** SPR response curves were recorded for the FG Nup binding of increasing titrated concentrations of (1), (2) and (3). **D.** Equilibrium binding analysis of the respective SPR response curves are represented here as Langmuir isotherms. The isotherm fits are shown as solid lines and yielded each the maximal response signal R_{max} and the equilibrium dissociation constant K_D.

Table 3.3 Summary maximal SPR response signals R_{max} and equilibrium dissociation constants K_D.

		Nup153	Nup214	Nup98
Kaps•NLS-NCs (1)	R_{max} **[RU]**	8774.7 ± 161	5026 ± 91	4398.6 ± 69
	K_D **[nM]**	18.4 ± 9	8.25 ± 0.5	9.2 ± 0.5
Kaps + blank NCs (2)	R_{max} **[RU]**	7036.5 ± 206	3839.4 ± 140	3066 ± 121
	K_D **[nM]**	18.4 ± 1.5	5.17 ± 0.71	8.13 ± 1.14
Kaps (3)	R_{max} **[RU]**	6888.8 ± 186	3507.8 ± 158	2879.8 ± 137
	K_D **[nM]**	24.8 ± 1.7	5.84 ± 0.97	10.25 ± 1.6

SPR sensorgrams were recorded (Figure 3.6 C) and the concentration dependence of the biosensor response were analyzed by fitting to a simple saturation binding model to determine the equilibrium dissociation constant (K_D) for the interaction. The data are presented in Figure 3.6 D and the fitted maximal response signals R_{max} and equilibrium dissociation constants K_D are given in Table 3.3.

As expected, Kapα/β1•NLS-NC binding to the three different FG Nups exhibited a maximal response that was considerably higher than for Kapα/β1 alone, due to the extra mass of the NLS-NCs (Table 3.3). In control measurements, blank NCs mixed with standalone Kapα/β1 did not elicit the same increased response as Kapα/β1•NLS-NCs, showing that blank NCs do not bind independently to either the FG Nups or the Kapα/β1•FG Nup complex. In contrast, the dissociation constants for interaction with the three different FG Nups did not differ significantly between Kapα/β1•NLS-NCs and isolated Kapα/β1 with no NCs present, or indeed for Kapα/β1 mixed with blank NCs.

These results show that NLS-NC binding to FG Nups is facilitated by the interaction of the NLS peptide with Kaps. However, the multivalent presentation of app. 57 Kapα/β1 complexes on the surface of a single NLS-NC at saturation did not appear to significantly alter the strength of Kap•FG Nup binding.

3.3.1 Attempted NLS-NC release from FG Nup layers *via* RanGTP

At the end of each measurement, the final cargo release out the NPC channel was mimicked by injecting 5 μM of RanGTP, which is essential for cargo release during nuclear import. As previously reported [35], a slight reduction in the SPR response was observed for Kapα/β1 due to the release of Kapα following RanGTP•Kapβ1 complex formation (Kapα - 58 kDa; RanGTP - 26 kDa). However, up to 20 μM RanGTP did not elicit a large drop in signal denoting NLS-NC release from the FG Nups (see Figure 3.6 C). This is likely due to the presence of 57 binding facilitating Kapα/β1 complexes per NLS-NC that exert a partially sterically shielded FG Nup-binding and hence, hindered the *in vitro* complex dissociation out the 2D FG Nup layer. To still be able to study the RanGTP facilitated NLS-NC release from FG Nups, nuclear import assays in permeabilized HeLa cells were conducted as described in one of the next Thesis chapter 4.

3.3.2 NLS-NCs cannot bind to FG Nups in the absence of Kaps

For completeness, the binding of blank NCs and NLS-NCs to FG Nups in the absence of Kapα/β1 was studied using the same SPR binding assay. Neither NLS-NCs nor blank NCs showed any significant sensor response in the absence of Kapα/β1, indicating that they do not bind to FG Nup153 on their own (Figure 3.7). Thus, the binding observed between NLS-NCs and FG Nups must be mediated by Kapα/β1 and cannot be due to direct interaction of FG Nups with the PMOXA-PDMS-PMOXA scaffold material or the surface-conjugated NLS peptide.

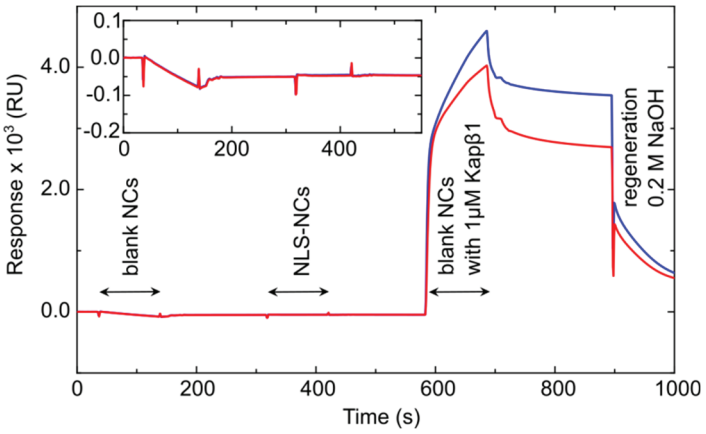

Figure 3.7 NLS-NCs and blank NCs do not interact with Nup153 in the absence of Kaps.

3.4 Materials and methods

3.4.1 NC preparation and labelling

0.5 mg/ml ***NLS-NC*** and 0.5 mg/ml ***blank NC*** stock dispersions were prepared as described in Thesis section 2.3. For dcFLCCS studies, nanocarriers were labelled with 200 nM lipophilic Bodipy 630/650 (Lumiprobe). The lipophilic dye was let intercalate spontaneously into the NCs membrane. After 30 min, the NCs were purified from free dye by SEC through a commercial Sephadex G-25 column (GE Healthcare).

3.4.2 Protein expression, purification and labelling

Human Kapβ1 was amplified by PCR in full-length and inserted into a *NcoI–BamHI* digested pETM-11 vector (EMBL Protein Expression and Purification Facility) in accordance to [35]. In an E. coli BL21 (DE3) cell line, the N-terminal His_6-tagged Kapβ1 was expressed at 30 °C overnight and afterwards purified using a nickel-nitrilotriacetic acid (Ni-NTA) column (Roche, buffer 1 : 10 mM TrisHCl, pH 7.5, 100 mM NaCl, 1mM DTT; eluted with 80 – 500 mM imidazole) followed by a size exclusion Superdex 200 column (Superdex 200 16/600, GE Healthcare). The obtained protein was analyzed on a 12 % SDS–PAGE and the identified Kapβ1

containing fractions pooled and dialyzed back against buffer 1. The protein concentration was determined by absorption measurements at 280 nm. For dcFLCCS experiments, Kapβ1 was labelled with Atto-550 succinimidyl ester (Atto-550 NHS-ester or simply Atto-550) in PBS buffer using the standard labelling procedure for primary amine-reactive probes (Invitrogen Protocols). The conjugation efficiency was determined by spectrophotometry (Nanodrop 2000) and revealed a stoichiometric 1:1 labelling of one Atto-550 dye molecule conjugated to one Kapβ1 receptor.

Full-length ***human Kapα*** (Addgene template pCMVTNT-T7-KPNA2; plasmid 26678) was cloned as reported previously in [35] into a *Xenopus laevis* Kapα containing pQE70 plasmid vector using EcoRI–BamII restriction enzymes. Both constructs are His_6-tag substituted at their C-terminus that is connected with a short linker (-GSRSHHHHHH) to not disturb the complex formation of this protein with Kapβ1. The formed Kapα was purified on a Ni-NTA column (Roche) followed by a size exclusion Superdex 200 column (Superdex 200 16/600, GE Healthcare). The final protein purify was analyzed on a 12 % SDS–PAGE and the protein concentration determined by absorption measurements at 280 nm.

The nuclear import vector ***wild type (WT) Ran*** was derived from the plasmid pQE32 encoding full length human RanQ69L *via* site-directed mutagenesis [35]. The expression of full-length His_6-tagged WT Ran was induced in isopropyl-*β*-*D*-thiogalactopyranosid (IPTG, Bioline Meridian, 0.5 M) treated BL21 competent cells at 24 °C overnight. The cells were lysed in buffer (50 mM HEPES-KOH (Sigma-Aldrich), pH 7, 100 mM NaCl (Merck), 5 mM DTT, 5 mM $MgCl_2$ (Merck), 20 mM imidazole (Merck), 10 mg/ml each of DNase (ThermoFischer), Pefobloc (Sigma-Aldrich) and lysozyme (Sigma-Aldrich)). Finally, WT Ran was purified using a Ni-NTA column (Roche) and an imidazole gradient (10 - 500 mM). The eluted protein was dialyzed in 10 mM HEPES buffer, pH 7.2 with 100 mM NaCl. WT Ran

was incubated for 30 min in 10 mM U9 (EDTA, Sigma-Aldrich) mixed with 1 mM guanosine triphosphate nucleotide (GTP, Sigma-Aldrich). Excess 25 mM $MgCl_2$ was added afterwards to ensure GTP binding to nucleotide-free Ran. GTP loaded WT Ran was then dialyzed into PBS buffer, pH 7.2 (GIBCO by Life Sciences), in the presence of 1 mM $MgCl_2$ and isolated with an Åkta Purifier integrated Superdex 200 HiLoad 16/60 column (GE Healthcare). Ran purity was analyzed by 12 % SDS-PAGE and the protein concentration determined by absorption measurements at 280 nm.

The ***human Nup153*** FG repeat domain 601aa, that is located at the proteins C-terminus (aa 874 – 1,475, Nup153-C), was PCR-cloned into commercial pGEX 6P-1 bacterial expression vector (GE Healthcare) in accordance to [178]. The so expressed construct is His_6-tagged at the C-terminus and contains an N-terminal glutathione-S-transferase (GST). The ***human Nup98*** FG repeat domains aa 1 - 505 were cloned into pPEP-TEV plasmid vector at the EcoRI and BamHI restriction sites using the pPEP-TEV prokaryotic expression vector as reported in [178]. The expressed construct contained a TEV protease cleavage site and an N-terminal His_6-tag followed by 36 residues of a short laminin linker. A pETM-11 vector was used for cloning the FG domain of ***human Nup214*** [177]. One cysteine was added to the C-terminus of each of the nucleoporins as a covalent tether to Au (on SPR sensor chips). For the expression of the recombinant Cys-Nup153, Cys-Nup98 and Cys-Nup62, again E. coli BL21 (DE3) competent cells (Novagen) were used. Protein purification was conducted under denaturing conditions (at pH 8.5 in 8 M urea, 100 mM Na_2HPO_4, 10 mM DTT and 10 mM Tris-HCl) using a Ni-NTA column. Subsequent cleavage of the N-terminal glutathione-S-transferase (GST) and C-terminal His_6-tag from Cys-Nup153-C was triggered by a PreScision protease (GE Healthcare). The His_6-tag of Cys-Nup98 was removed using a TEV protease. The purity of the final proteins was analyzed by 12 % PAGE at 0.1 % SDS and the

selected fractions dialyzed against PBS (Invitrogen, pH 7.2) and stored at -80°C for further use.

3.4.3 Instrumental binding analysis

The ***Fluorescence lifetime (cross-)correlation spectroscopy (FL(C)CS)*** setup used for Kap binding analysis to NLS-NCs and blank NCs including confocal volume calibrations are described in chapter 2. Also, the ***Transmission Electron Microscopy (TEM)*** setup and the applied TEM sample preparation procedure as well as the ***Dynamic Light Scattering (DLS)*** setup and the DLS sample preparation procedure that were used to study Kap binding to NLS-NCs and blank NCs are described in chapter 2.

Surface Plasmon Resonance **(SPR)** ***spectroscopy*** was used to study the binding of Kapα/β1 conjugated NLS-NCs to nucleoporins *in vitro*. Standard binding assays were performed on a BiacoreT200 (GE Healthcare) instrument that was therefore equipped with a flow cell with four parallel flow channels at constant 298 K. As described in more detail before by Schoch *et al.* (2012, [179]) and Kapinos *et al.* (2014, [177]), differential resonance determinations were derived between two flow cells conjugated with cysteine modified Nup98, Nup214, or Nup153 (sample cells) and two flow cells conjugated with PUT (reference cells with PUT = HS-$(CH_2)_{11}$-$(OCH_2$-$CH_2)_3$-OH, Nanoscience). A 1 % BSA (Sigma Aldrich) and 1 mM $MgCl_2$ containing PBS (Gibco by Life Technologies, pH 7.2) running buffer was used. At a flow rate of 10 μl/min, successively increasing concentrations of Kapβ1:Kapα (1:10): 0.1953125:1.953125, 0.390625:3.90625, 0.78125:7.8125, 1.5625:15.625, 3.125:31.25, 6.25:62.5, 12.5:125,25:250, 50:500 and 100:1000 nM were added and whilst indicated *in situ* mixed with respectively increasing mass concentrations of 0.195, 0.391, 0.781, 1.563, 3.125, 6.25, 12.5, 25, 50 and 100 μg/ml of NLS-NCs or blank NCs. The NCs were incubated with Kap complexes for 2 hours before flow cell injection.

Chapter 4

NLS-NCs are Targeting HeLa Cell Nuclei *via* NPCs

Thesis chapter contributions

C. Rencurel (Technical associate at University of Basel): Expression and purification of Kaps, NTF2 and Ran protein.

C. Tiberi (Technical staff at University of Basel): Thin-sectioning of polymersome treated cell-pellets and preparation of cell-section mounted grids for BioEM.

I. Cracium (Postdoctoral researcher at University of Basel): Examination and analysis of the cell viability of NLS-functional and blank polymersomes in HeLa cells.

4 NLS-NCs are targeting HeLa cell nuclei *via* NPCs

4.1 Introduction

Previously it was reported that nanoparticles (NPs) are capable of adopting various different pathways to translocate into cell nuclei [129]. Whilst NLS- [126, 180] or IBB- [58] conjugated NPs actively trigger a Kap facilitated NPC migration, TAT-conjugated NPs were found to employ an Kap-NPC independent nuclear import mechanism by electrostatically induced nuclear envelope penetration [181]. Also, the NPs' scaffold material itself can drive nuclear infiltration. As a case in point, cationic polymeric particles prepared from poly (*L*-tartaramidoamine) were found to enter the nucleus by inducing holes in the nuclear membrane [182]. In addition to the those pathways, NPs can undergo nuclear translocation when the NE is degraded as the cell is prepared for division in the M-phase of the cell cycle [183].

To complicate matters, successful translocation of nuclear targeting NPs depends on multiple cellular trafficking steps [94] and is generally affected by the NPs apparent (i) internalization kinetics [128, 184], (ii) their biodistribution and cytotoxicity and (iii) their intracellular mobility, given by the cellular permeability towards NP migration. Moreover, all of those trafficking steps seem to be highly dependent on the structural and physico-chemical properties of the applied NPs [131, 132]. This chapter intends therefore to identify key molecular parameters underlying the nuclear import of NLS-NCs (see Figure 4.1 C). The aim is to resolve structure-activity relationship for NLS-NC uptake. The intracellular localization and nuclear or perinuclear targeting of NLS-NCs were investigated by different import assays, and the results were correlated with the physico-chemical (Thesis chapter 2) and biofunctional (Thesis chapter 3) properties of the polymersomes.

As a control to ensure that the observed behavior was NLS-specific, additional measurements were made for blank NCs (*i.e.* polymersomes that are lacking the nuclear import activating NLS surface tag).

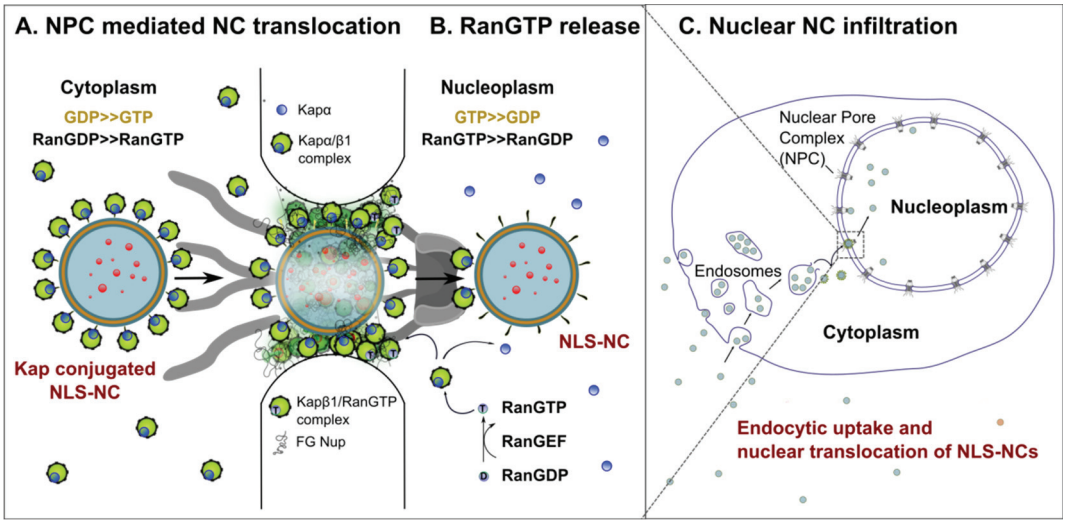

Figure 4.1 Polymersome-NCs are imported into cell nuclei by NLS-mediated mechanisms. A. NLS-NCs are utilizing surface associated Kapα/β1 complexes to migrate from the perinuclear region into NPC channels through multivalent binding interactions with FG Nups. **B.** Subsequent Kapα/β1•NLS-NC complex dissociation by RanGTP at the nuclear channel exit finalizes the import with the finite NLS-NC release into the cell nucleus. **C.** Selectively imported NLS-NCs are accumulating in the nucleus and due to the existing RanGTP/RanGDP asymmetry can do so even against prevailing concentration gradients.

Time-lapse fluorescence microscopy was used to monitor the cellular internalization kinetics and the nuclear infiltration of NCs in living HeLa cells. Electron microscopy was used to visualize the migration of NCs across the nuclear envelope at the level of single NCs (see Figure 4.1 A), allowing the minimal functional NPC diameter of HeLa cells to be determined. This functional NPC diameter is of crucial importance for the design of nuclear targeting nanocarriers because only carriers with diameters equal or smaller than that diameter can be imported [126, 185].

Finally, an e*x vivo* transport assay in digitonin-permeabilized HeLa cells was used to investigate the dependence of NLS-NC uptake on the presence of RanGTP.

This small Ras-related nuclear protein is an essential import factor that finalizes the release of biological cargo from NPCs [68]. To identity all import mechanistic steps, it was important to demonstrate that this process was also involved in successful NC entry into the nucleus (see Figure 4.1 B).

4.2 Nuclear infiltration by NLS-NCs

It has previously been shown that PMOXA-PDMS-PMOXA based polymersomes are readily engulfed by HeLa cells and enter the cytoplasm through an endosomal escape pathway [186]. The work in this chapter aims to illuminate the fate of polymersomes upon cellular internalization and to correlate their nuclear import viability to the presence of NLS targeting signals on the polymersome surface. Time-lapse fluorescence microscopy (FM) was used to monitor the migration of Bodipy 630/650 labelled NLS-NCs across HeLa cells. Their nuclear targeting ability was examined, and their time dependent quantitative targeting efficacy compared to those of Nile Red 552/636 labelled blank NCs.

A mild, three-dimensional deconvolution wide-field FM method was chosen to minimize photobleaching and phototoxicity during image acquisition. This greatly reduced the intensity of excitation light compared to standard confocal FM techniques [187]. The possibility of pixel saturation during long time-course imaging of effectively internalized fluorescent NCs was mitigated by determining an optimal but sufficiently low fluorescence exposure time and laser power.

Live cell experiments were performed at 50 – 80 % confluency, at 37 °C and in a 5 % CO_2 atmosphere. To start the experiments, 0.6 nM NLS-NCs, 0.6 nM blank NCs or a mixture containing both 0.6 nM NLS-NCs and 0.6 nM blank NCs, were added in one shot to the HeLa cells and gently mixed with the culture medium that surrounded the cells (see Thesis section 4.6.4 for experimental details).

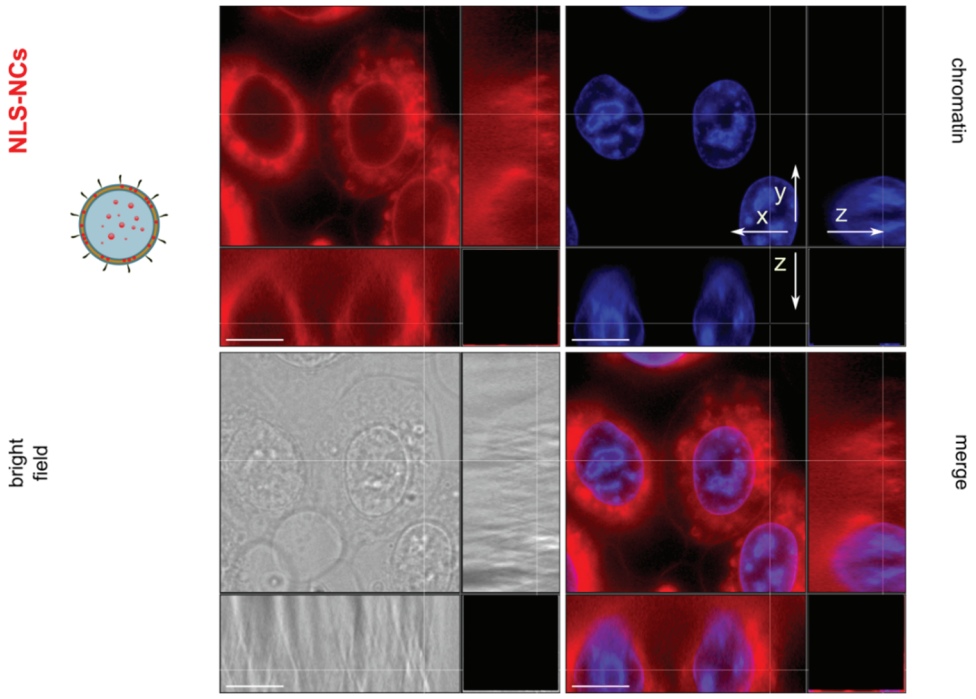

Figure 4.2 HeLa cells incubated with NLS-NCs and visualized after 12 hours by three-dimensional deconvolution fluorescence microscopy. The fraction of nuclei imported NLS-NCs can be seen to be co-localized with the nuclear chromatin (bottom right merged image). Scale bar is 10 μM.

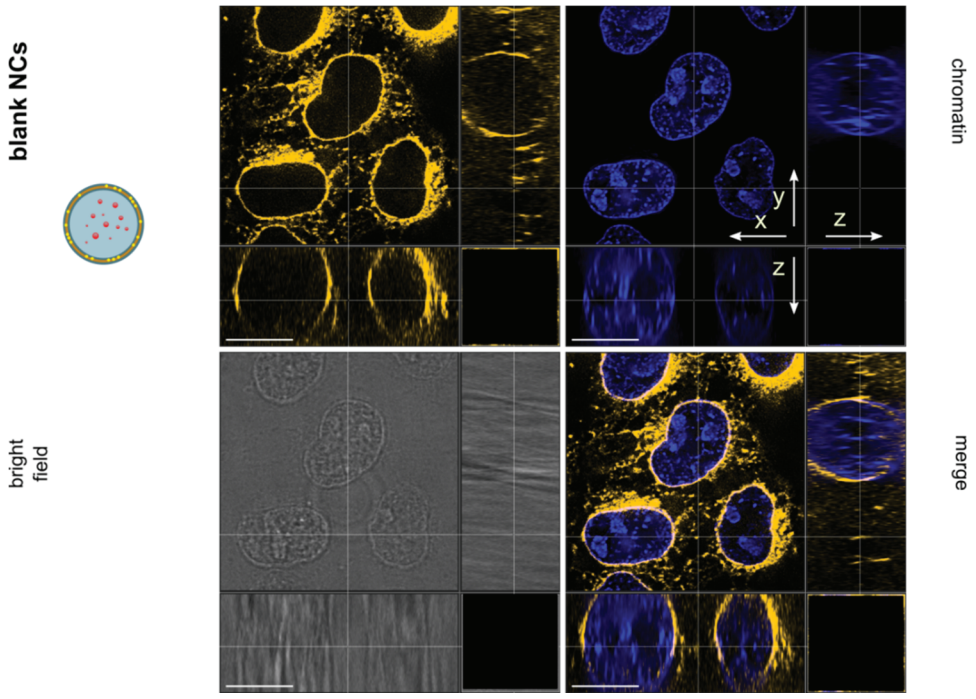

Figure 4.3 HeLa cell incubated with blank-NCs and visualized by three-dimensional deconvolution fluorescence microscopy after 12 hours. Signal co-localization of blank NCs with the nuclear chromatin shows only minor nuclear import but significant NC accumulation along the nuclear envelope (bottom right merged image). Scale bar is 10 μM.

The cellular internalization and nuclear infiltration of NLS-NCs and blank NCs was investigated over a time course of 12 hours with images taken every 30 minutes. The time-dependence of NC biodistribution across cell compartments was extracted from z-stacked image sets recorded at each time point over a stack range of 15 μm at z-intervals of 0.35 μm. The images were deconvoluted for increased resolution and reconstituted as 3D images using *Imaris* software.

NCs imported into HeLa cells were identified based on the Bodipy 630/650 signal of NLS-NCs and the Nile Red 552/636 signal of blank NCs and subsequently their co-localization with Hoechst-stained nuclear chromatin assessed by inspection of merged images. Following 12 hours incubation, both NLS-NCs and blank NCs are taken up into the cells. However, only NLS-NCs showed a pronounced increase in the average nuclear fluorescence intensity (see merged image in Figure 4.2). Strikingly, after nuclear import, the NLS-NCs tended to accumulate along the nucleoli. This distribution might arise because of electrostatic attraction between the positive surface potential of the NCs (see Thesis section 2.4.6 for details) and the negatively-charged nucleoli [188]. In marked contrast, blank NCs are transported to perinuclear regions but are prevented from further passage through the nuclear envelope. They accumulate around the nuclear envelope, giving an apparent rim-staining of the nucleus (Figure 4.3). Differences between the nuclear uptake of NLS-NCs and blank NCs are most evident following their co-incubation with the same cells. As can be seen in Figure 4.4, under these circumstances it is predominantly NLS-NCs that enter the nucleus.

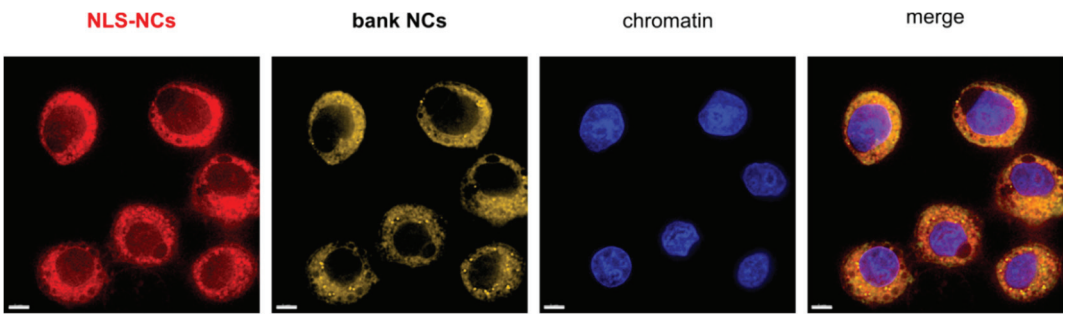

Figure 4.4 HeLa cells co-incubated with NLS-NCs and blank NCs. After 12 h incubation, predominantly NLS-NCs entered the nucleus whilst blank NCs were mostly blocked out along the nuclear envelope. Scale bar is 10 μM.

4.2.1 Cellular import kinetics

For quantitative evaluation of the cellular uptake and biodistribution of NLS-NCs and blank NCs, the same time-lapse z-stack image data-sets were analyzed with the *Imaris* module *ImarisCell* (Thesis section 4.6.7). This allows the analysis of fluorescence intensity summed over the entire 3D volume of each reconstituted HeLa cells, as a function of time. This analysis was applied to a total of 28 cells incubated with NLS-NCs and 18 cells incubated with blank NCs (Figure 4.5). The fraction of nuclear imported NCs was determined from NC signal that co-localized in the same 3D volume as the nuclear chromatin Hoechst stain. Thereof, the quantity of cell cytoplasm localized NCs was derived as difference to the sum intensity that was detected in the 3D reconstituted cell volume. On a technical note, the NC signals that are presented in Figure 4.5 as relative fluorescence intensities *I(t)* are calculated from the detected photon counts per unit volume, using the value at time zero as a reference.

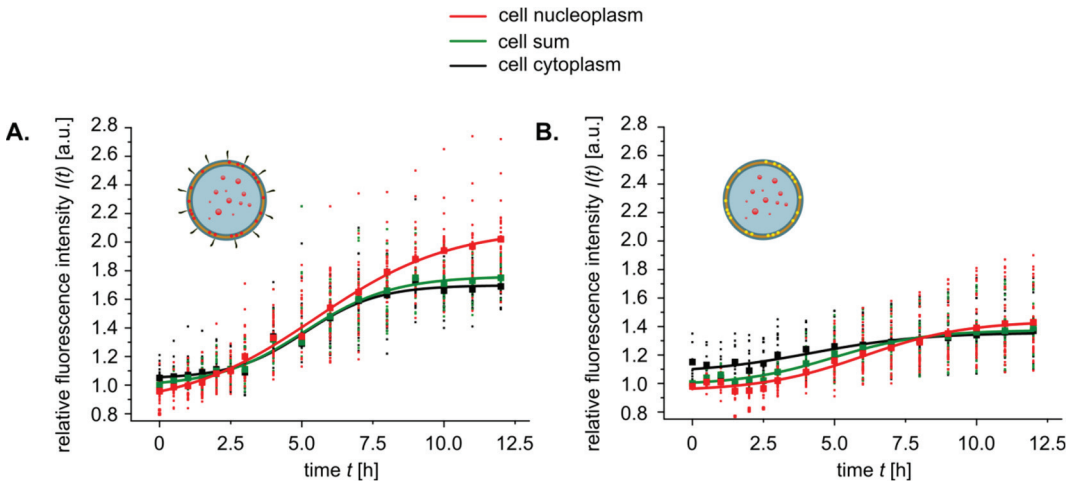

Figure 4.5 Intensity plots of the time-dependent signal evolution of cell uptaken NCs A. Bodipy 630/650 labelled NLS-NCs and **B.** Nile Red 552/636 labelled blank NCs.

A time-dependent increase in the summed fluorescence intensity from the whole cell for both the Bodipy 630/650 labelled NLS-NCs and the Nile Red 552/636 labelled blank NCs, showed that both NC types infiltrated HeLa cells. However, the behavior of the NC types varied significantly. The detected increase in cytoplasmic fluorescence was larger for cells incubated with NLS-NCs than for cells incubated with blank NCs (to see on the higher net-amplitude of the black graph in Figure 4.5 A as compared to the black graph in Figure 4.5 B) and suggests that HeLa cells preferentially internalize the NLS conjugated NC derivative. This phenomenon has been reported before for polymersomes from polyethylene glycol (PEG) – polylactic acid (PLA) diblock copolymer, where cellular import across the plasma membrane of BxPC-3 cells could only be triggered by polymersome conjugation with the short NLS peptide PKKKRKV [106]. NLS sequences with an overall positive net charge therefore appear to mediate cell penetration [189] and this might have amplified the NLS-NC uptake in the experiments described here. It is also apparent that nuclear transport is promoted by the NLS sequence. The average nuclear intensity for NLS-NCs increased by 108 %, a significantly higher increase compared to the 40 % observed for blank NCs (red graph in Figure 4.5 A *vs*. red graph in Figure 4.5 B).

The difference in biodistribution of NLS-NCs and blank NCs becomes more apparent when uptake into the cytoplasm is compared with uptake into the nucleoplasm. After 2.5 hours of NLS-NC incubation, the carrier concentration in the nucleoplasm becomes equivalent to that in the cytoplasm and the relative abundance of NLS-NCs in the nucleoplasm increases further at longer time points. Generally, there are several factors that must be taken into account when considering these concentration distributions: (i) the NC concentration in the cytoplasm is increased by import across the plasma membrane, but decreased by import of NCs into the nucleus, (ii) since nuclear import of NCs can be assumed to be irreversible, there is no process acting to decrease the nuclear concentration of NCs over time and (iii) the concentration of NCs in a given compartment is determined by the amount of NCs and the volume of the compartment. Since the nucleus has a much smaller volume than the cytoplasm, a given amount of NCs in the nucleus would give a much higher concentration than the same number in the cytoplasm. All things considered, NLS-NCs seem to be facilitating an off-gradient concentrated nuclear import already 2.5 hours after their exogenous application. In marked contrast, blanks NCs import less into cell nuclei and an off-gradient nuclear NC accumulation is seen only after 8 hours incubation time.

NLS-NCs and blank NCs have similar physico-chemical properties and differ only in the presence or absence of surface-conjugated NLS peptides. Hence, the observed difference in nuclear import can be ascribed to the biofunctionality arising from the NLS peptides on the NLS-NC surface. These results suggest that nuclear import occurs *via* a Kap-NPC facilitated mechanism for NLS-NCs.

The resolution of the deconvolution wide-field FM is limited by diffraction. The available resolution was not sufficient to identify the precise trajectories that NLS-NCs take across the NE. Therefore, this data cannot determine whether NCs are shuttling through NPCs, or whether they undergo a non-specific NE penetration to reach the cell nucleus.

4.3 Ultrastructural analysis of nuclear infiltration by NLS-NCs

To determine the path of the NLS-NCs across the NE, whether that pathway involved NPCs, and whether NLS-NCs retained their structural integrity after transport, transmission electron microscopy (TEM) ultrastructural analysis was performed. For the sake of clarity, in this work the term BioEM is used to refer to structural analysis of the biology of cells. In BioEM it remains however a formidable challenge to resolve PMOXA-PDMS-PMOXA based NCs in crowded cellular environment due to their low image contrast. Thus, an EDTA regressive staining protocol (Thesis section 4.6.4) was employed to visualize single nuclear import events. This Thesis section details the investigation of the trajectories that NLS-NCs are taking to cross the NE (Thesis section 4.3.4) and evaluates the functional NPC diameter of HeLa cells (Thesis section 4.3.3).

4.3.1 NC visualization in HeLa *via* regressive EDTA staining

NLS-NCs and blank NCs that had been internalized into cells were visualized by BioEM. This uses a regressive EDTA staining (Bernard, 1969 [190]) to enhance the visibility of the polymersomes (app. 60 nm-diameter) in crowded cellular environment. 0.6 nM of RR encapsulating NLS-NCs or 0.6 nM of RR encapsulating blank NCs were exogenously applied to HeLa cells and incubated over a period of 12 hours. Cell sections of < 50 nm thickness were prepared from aldehyde-fixed and Epon embedded HeLa cells and mounted onto Nickel grids. These sections were negatively stained with 6 % uranyl acetate (UA) solution. Subsequent treatment with 0.2 M EDTA solution led to partial regressive extraction of uranyl cations such that the uranyl ion depleted tissue appeared with lower contrast in EM. Within the cell nucleus, EDTA is depleting predominantly uranyl ions that are staining the chromatin and less uranyl ions that are intercalated in the RNA. Final post-staining with lead citrate rendered all RNA containing compounds contrast

rich whilst deoxyribonucleoproteins have lost most or all their staining. As consequence, the otherwise very densely stained nucleus (Figure 4.6 B) seems less filled (Figure 4.6 A) and provided here a means to `uncover` polymersome-nanocarriers located in the nuclear and in the perinuclear region.

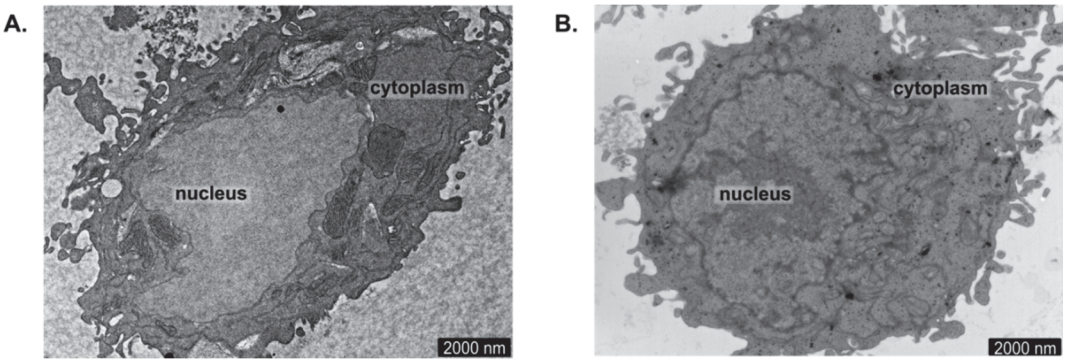

Figure 4.6 HeLa cell sections treated with different stainings **A.** Section treatment with uranyl acetate and a regressive EDTA post-staining results a bright cell nucleus due to 'unstained' chromatin. This staining procedure enabled here the visualization of nuclei imported polymersomes. **B.** Section treatment with only uranyl acetate and no EDTA leaves the nuclei inherent nucleoli, interchromatin granulates and cytoplasmic ribosomes heavily stained and hampers the precise identification of nuclei imported polymersomes.

4.3.2 Structural identification of NCs in HeLa

Whilst cells and most subcellular organelles are enclosed by ~ 4 nm-thick phospholipid bilayers [191] the NLS-NCs have a 8.4 ± 1.1 nm-thick membrane and blank NCs have a 8.2 ± 1.5 nm-thick membrane (Thesis section 2.4.1). In addition, phospholipid bilayers treated with UA appear with a sharp rim on both sides, given by the electrostatic staining of the negatively charged phospholipid head groups. However, $PMOXA_4$-$PDMS_{44}$-$PMOXA_4$ polymersomes have more blurred and less defined membranes, but their identification is aided by a distinct bright inner cavity. Therefore, evaluation of BioEM images focused on NLS-NCs and blank NCs identified both by a closed circular membrane of > 8 nm thickness and a bright inner cavity (Figure 4.7).

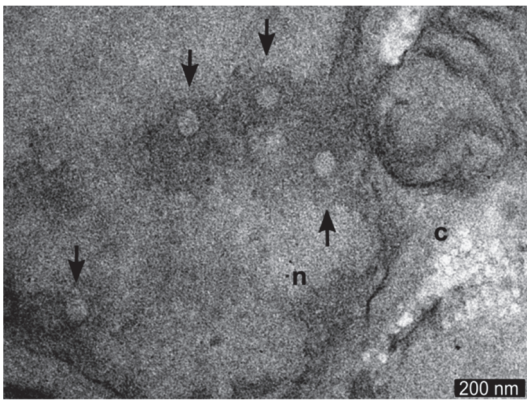

Figure 4.7 Cell internalized polymersomes as identified after EDTA staining based on their closed circular membrane of > 8 nm-thickness and their bright inner cavities (c, cytoplasm; n, nucleoplasm).

4.3.3 NPC channel diameter in HeLa

Figure 4.8 A. shows a representative TEM micrograph of an NPC cross-section where the inner channel appears empty due to the regressive EDTA staining procedure that would leave any RNA cargo in the NPC unstained. The pore width of 197 such NPCs was measured with *ImageJ* software, taking the measurement across the narrowest side of the central pore, giving an average diameter of 61 ± 16 nm (Figure 4.8 B). This value is in good agreement with the 68 ± 3 nm reported previously [145].

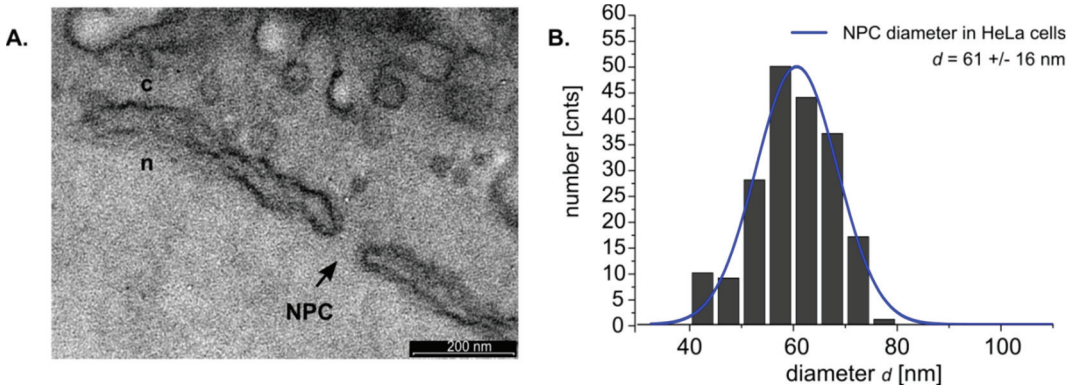

Figure 4.8 NPC channel diameter in HeLa cells *via* BioEM. A. Representative EM micrograph showing an NPC channel that perforates the nuclear envelope of a HeLa cell (c, cytoplasm; n, nucleoplasm). **B.** Cross-section analysis of 197 NPCs revealed an average gated channel diameter of 61 ± 16 nm.

4.3.4 NLS-NCs in NPC transit

All the results described before in this Thesis suggest that NLS-functional polymersomes enter cell nuclei through Kap-facilitated NPC translocation. This assertion is supported by the observed selective Kapα/β1 binding to NLS-NCs (Thesis section 3.2), the consequent Kapα/β1•NLS-NC binding to FG Nup layers (Thesis section 3.3) and finally the import of NLS-NCs into HeLa cell nuclei (Thesis section 4.2). These findings are complemented by resolving the transport of NLS-NCs across the NE in greater detail using BioEM.

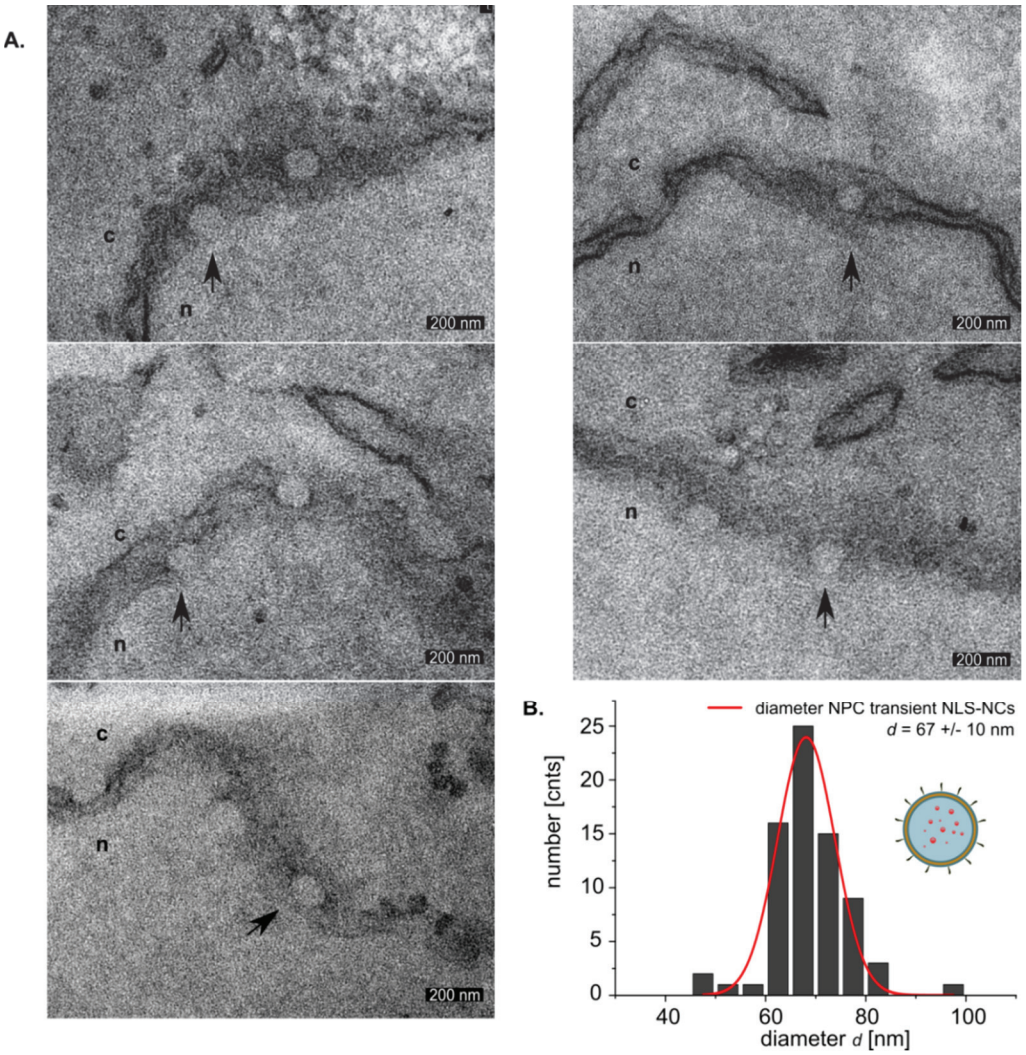

Figure 4.9 Nuclear import in HeLa was visualized 12 hours after the exogenous administration of 0.6 nM NLS-NCs. A. BioEM analysis revealed NLS-NCs as partially caught in NPC transit (c, cytoplasm; n, nucleoplasm). **B.** For statistical size analysis, 72 NPC transient NLS-NCs were imaged in in total 56 HeLa cells and their average diameter determined to 67 ± 10 nm.

NLS-NC passage across the NE was visualized 12 hours after their administration to the exterior of the cells. In 56 HeLa cells imaged by BioEM, 72 NLS-NCs were observed to be trapped during NPC transit. Their sizes and size distribution were determined using *ImageJ* software, giving an average diameter of 67 ± 10 nm. By comparison, the NPC channel width in HeLa was determined to be 61 ± 16 nm. It is therefore apparent that NPCs can accommodate synthetic NLS-functional objects that are equal to or exceed the size of their own central channels.

The maximum size of cargo that can be translocated by the NPC (the NPC threshold size) was investigated for the first time in 1988 (Dworetzky *et al.* [185]). At that time, NLS-bearing gold nanoparticles of different sizes were injected to *Xenopus oocytes* and the functional NPC diameter was determined to 26 nm. However, in 1995 it was shown that NLS-cargoes diffuse through the NPC channel together with their soluble Kaps in a cargo-receptor complex (Görlich *et al.* [192], Moroianu *et al.* [193], Radu *et al.* [194]). These new insights motivated a subsequent study to determine the correct NPC threshold size. 26 nm diameter NLS-bearing gold nanoparticles were once more employed, but in this case they were precoated with a Kapα/β1 layer, and the overall cargo-receptor complex diameter was determined to be 39 nm (Panté *et al.* [84]). Those 39 nm particles were seen to be imported into *Xenopus oocyte* nuclei. However, slightly larger 43 nm Kapα/β1-coated NLS-gold particles could not be translocated through the NPC. It was therefore concluded that the ~ 44 nm diameter central gated pore of *Xenopus oocyte* NPCs has a functional diameter of 39 nm for nuclear NLS-cargo translocation.

In accordance with the work of Panté *et al*., the average size of NLS-functional polymersomes complexed with Kapα/β1 (Kapα/β1•NLS-NCs) was determined using TEM to be 62 ± 34 nm prior their cellular application (see Thesis section 3.2.7) and to be 67 ± 10 nm in HeLa cells during NPC transit. These findings

imply that the nuclear import into HeLa cell nuclei is not limited to cargo compounds less than or equal in diameter to the value of 39 nm given in literature. It has been suggested that NPC threshold size varies with cell type [94], and the data here suggest that the functional NPC diameter is much larger for HeLa cells than for *Xenopus oocytes*. With an NPC diameter of 61 ± 16 nm, even 67 ± 10 nm diameter NLS-specific cargo compounds can be incorporated and translocated along the gating channels. Since only one size of NLS-NCs were used in this study, which were able to cross the NPC, it is not possible to estimate the maximum size threshold for NPC transport in HeLa cells. Nevertheless, the anticipated variation of NPC threshold size on cell-type is confirmed by the data presented here. It is therefore very important to consider the NPC threshold size of the cell type that is being targeted when attempting to nanoengineer nuclei targeting nanoparticles. This study also shows that BioEM represents a convenient and straightforward way to estimate that crucial parameter. It allows characterization of the NPC structure in isolation, and through the use of the regressive EDTA staining protocol it also permits identification and location of PMOXA-PDMS-PMOXA based polymersomes in cell cross-sections.

On another note, the translocation of large NLS-cargoes across the confined gate channels is promoted only in Kapα/β1•NLS-cargo transport complexes whilst the like is highly improbable for non-specific (non- Kapα/β1 carrying) cargoes as of blank NCs. To examine the permeability of NPCs towards blank NCs experimentally, a comparative BioEM measurement was conducted. Despite the identical experimental conditions and the similar 67 $\pm$ 6 nm NC diameters, only 11 blank NCs were captured in NPC transit within in total 21 cells. This corresponds to a reduction in the NC-import frequency of 60 % for NPC-transient blank NCs as compared to the above discussed NPC-transient NLS-NCs. Thus, it is apparent that blank NCs are not so readily accommodate and translocated by the NPC as are NLS-NCs, an observation that is consistent with previous time-lapse fluorescent microscopy results (Thesis section 4.2). Although

blank NCs can be imported into cell nuclei, this occurs through a non-specific pathway since they lack the NLS sequence essential for Kap-facilitated import. The results presented here show that this non-specific import occurs with far reduced probability compared to the specific pathway.

4.3.5 Cellular NC distribution

Next the biodistribution of NCs between the cytoplasm and the nucleoplasm of HeLa cells was examined using BioEM with regressive EDTA staining, 12 hours after the exogenous application of either 0.6 nM NLS-NCs or 0.6 nM blank NCs. This allowed a statistical assessment of the effect of NC size and of NCs conjugation with NLS signals upon the efficacy of NC nuclear import.

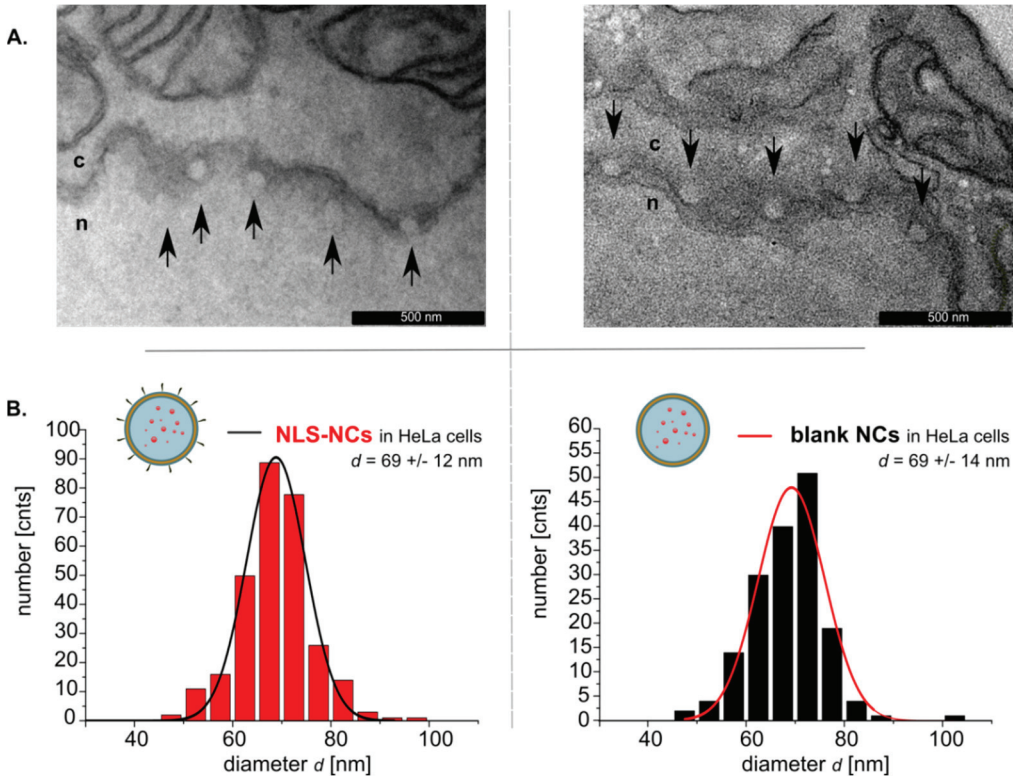

Figure 4.10 Biodistribution of cell internalized nanocarriersfollowing a 12 hours HeLa cell incubation with 0.6 nM NLS-NCs (left side) or 0.6 nM blank NCs (right side). A. Representative BioEM micrographs show NLS-NC accumulation along the nucleoplasmic side of the NE and in contrast NE rejected nuclear entry for blank NCs. **B.** For statistical size and size distribution analysis, 292 HeLa cell internalized NLS-NCs were imaged, and their average diameter determined to 69 ± 12 nm. In the same manner, blank NCs (n = 166) showed very similar diameters with 69 ± 14 nm.

Figure 4.10 (upper panel) shows clearly that both NLS-NCs and blank NCs were transported to the perinuclear region, apparently with full structural integrity. However, in agreement with fluorescence microscopy data, only NLS-NCs show an enhanced tendency to accumulate inside the cell nucleus. Size analysis of cell-internalized NCs was accomplished using *ImageJ*, from a total of 292 NLS-NCs in 56 cells that were visualized distributed across the cell cytoplasm, the perinuclear region, caught in NPC transit, or accumulated in the nucleus. The average diameter of these NLS-NCs was determined to be 69 ± 12 nm. The average diameter of 166 blank NCs that were found distributed in 21 cells was found to be very similar at 69 ± 14 nm (Figure 4.10 lower panel).

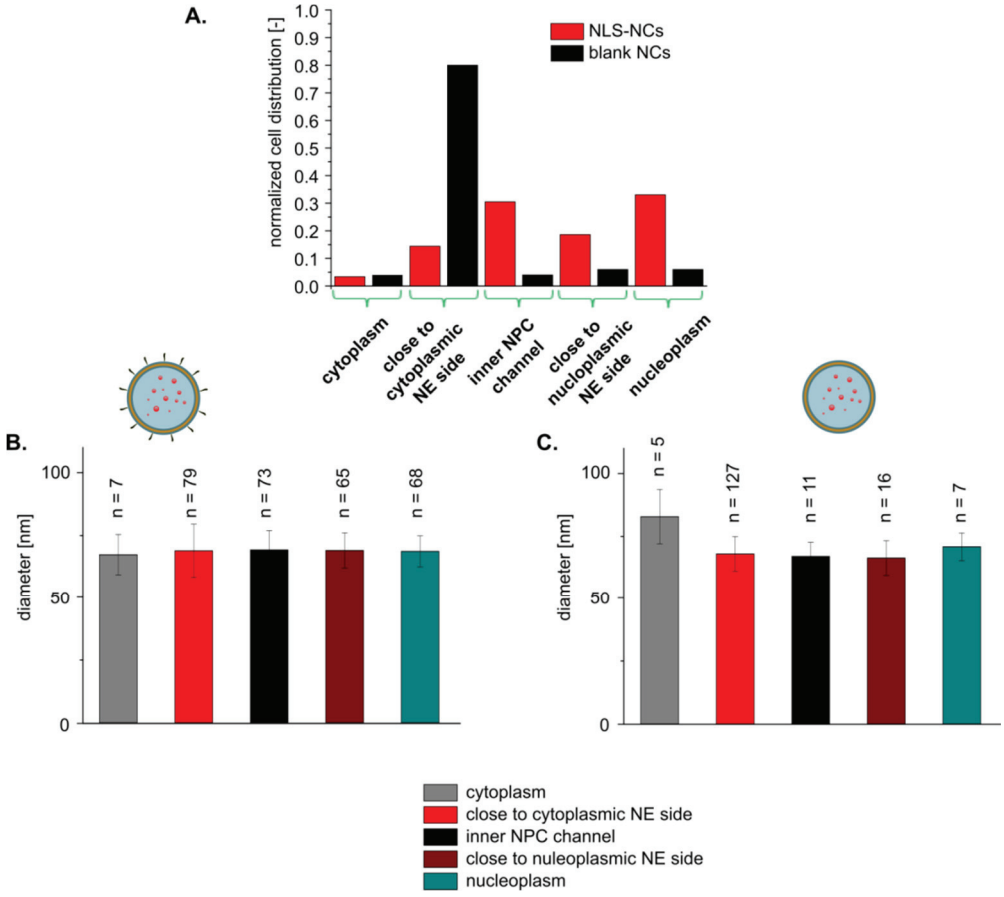

Figure 4.11 HeLa cell internalized polymersomes were found distributed across the cell cytoplasm, close to the cytoplasmic side of the nuclear envelope (NE), in NPC transit, close to the nucleoplasmic NE side and accumulated within the nucleoplasm. A. Statistical distribution of NLS-NCs (n = 292 in 56 cells) and blank NCs (n = 166 in 21 cells) across the cell compartments. The same **B.** NLS-NCs and **C.** blank NCs were classified for their cellular location and correlated with their local size distribution.

A breakdown of the distribution of NLS-NCs based on intracellular location and their average diameters is shown in Figure 4.11. The percentage of NLS-NCs in each location and their average diameter can be summaries as follows: (i) nuclear interior – 23 % with diameter 68 ± 6 nm (n = 68) (ii) NPC channel – 25 % with diameter 69 ± 8 nm (n = 73), and (iii) cytoplasm – 3 % with diameter 67 ± 8 nm (n = 7). Moreover, 27 % NLS-NCs were found at the cytoplasmic NE (diameter 68 ± 11 nm, n = 79) and 22 % at the nucleoplasmic NE side (diameter 69 ± 7 nm, n = 65). These data show that the NLS-NCs do not show a size-dependent localization. The observed number distribution across the 61 ± 16 nm wide HeLa NPC channels as well as the evaluated average NLS-NC size is almost equal in all compartments.

It should further be note that a high fraction of NLS-NCs reached the nuclear interior and did so whilst maintaining their intact carrier structure. In marked contrast, despite their similar 68 ± 7 nm diameter, 77 % of blank NCs (127 out of 166 observed) were found in the cytoplasm, having apparently been prevented from passage into the nucleus.

In summary, all the results reported here demonstrate that the functionalization of polymersomes with NLS sequences facilitates enhanced nuclear import due to the adoption of the Kap-NPC import mechanism. It was however not possible to detect a size dependency (*i.e.* a size exclusion effect) to this translocation and the consequent biodistribution.

4.4 Cytotoxicity of NLS-functional and blank NCs

NLS-NCs have shown to possess the necessary structural integrity to be translocated through NPCs and into the nucleus. Next, a standardized cell viability assay (MTS, Invitrogen) was conducted to investigate whether the carriers are

cytotoxic once internalized into HeLa cells, which is of particular importance for their use in biomedical applications. Importantly, this study showed that neither NLS-NCs nor blank NCs were toxic to the HeLa cells up to 48 hours (Figure 4.12).

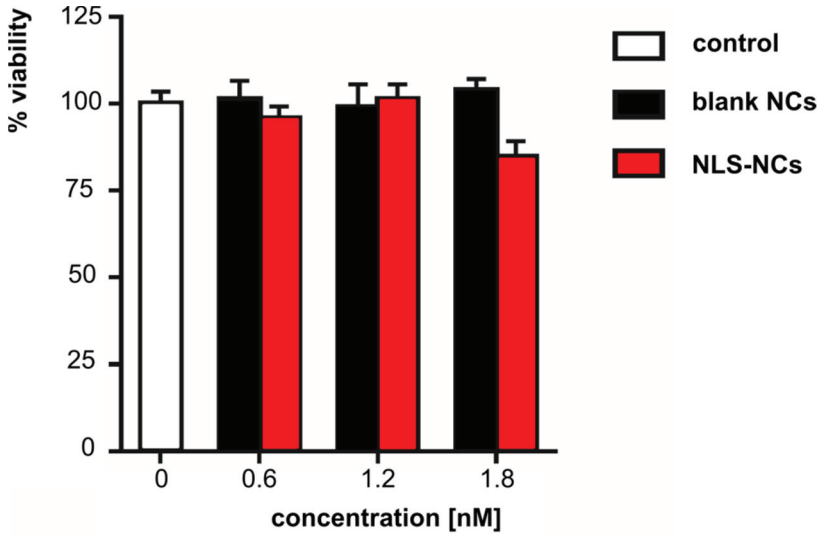

Figure 4.12 NLS-NCs and blank NCs exert an only minor cytotoxicity to HeLa cells after 48 h incubation time whilst treated with 0.6 nM NCs (standard concentration used in all HeLa cell experiments) and not for doubled 1.2 nM or triplet 1.8 nM NC concentrations.

4.5 RanGTP regulates the nuclear uptake of NLS-NCs

4.5.1 Permeabilized HeLa cell import assay

Next, the role of RanGTP in the nuclear import of NLS-NCs and blank NCs was investigated using a digitonin-permeabilized HeLa cell assay, first developed by Adam *et al.* in 1990 [195]. This assay provides a means to (i) characterize the nucleocytoplasmic trafficking of proteins, RNA and other macromolecular or supra-macromolecular cargoes, (ii) analyze requirements for the import of specific cargoes and (iii) identify crucial import vectors and their regulatory functions [196].

Cell treatment with low concentrations of the nonionic, cholesterol binding detergent digitonin (here applied 40 μg/ml) increases the permeability of the plasma membrane [197] towards exogenous (biological, synthetic or hybrid) nanoobjects whilst leaving the nuclear envelope intact and the NPC structures with full integrity and functionality [195]. After treatment with digitonin, permeabilized cells are depleted of shuttling nuclear transport factors. The assay reconstitutes NCT using a mixture of exogenously applied recombinant transport factors, generally referred to as "Ran mix".

To assess the regulatory function of RanGTP towards the nuclear import of polymersomes, a Ran mix was applied that consisted of (i) 100 μM ATP, 4 mM creatine phosphate and 20 U/ml creatine kinase, to provide energy for nuclear transport, (ii) fixed concentrations of Kapβ1 (1 μM) and Kapα (2 μM) and (iii) varying RanGDP/ GTP/ NTF2 concentrations including the physiological values 5 μM/ 1 mM/ 1 μM, 4 fold higher concentrations, 20 μM/ 4 mM/ 4 μM, and no exogenously applied RanGDP/ GTP/ NTF2. The respective Ran mix was added to the permeabilized cells and incubated for 30 minutes. RanGDP is thereby transported into the cell nucleus by its transporter NTF2 where it is converted to RanGTP by endogenous RanGEF.

Nuclear import was then visualized and quantified using FM (see Thesis section 4.6.6 for more details). NLS-NCs labelled with Bodipy 630/650 or blank NCs labelled with Nile Red 552/636 were added to the solution surrounding the cells, at a final concentration of 0.6 nM. Their NCT was visualized at RT with a wide-field fluorescence microscope over 120 minutes with images taken every 10 minutes. This allowed the progress of nuclear import for NLS-NCs to be compared in the absence of exogenous RanGDP, at 5 μM RanGDP and at 20 μM RanGDP. As a control, the progress of nuclear import for blank NCs was observed after the cells were incubated with 5 μM RanGDP.

4.5.2 RanGTP regulates the nuclear NLS-cargo import efficacy

Reversible Kap binding to NLS-NCs (*in vitro* dcFLCCS assay in Thesis section 3.2) and Kap-mediated NLS-NCs association to FG Nups (*in vitro* SPR assay in Thesis section 3.3) have been identified as integral mechanistic steps in NCT of NLS-NC *via* NPCs. However, a role for RanGTP in the NCT of NLS-NCs has not yet been demonstrated unambiguously, although it was studied using 2D FG Nup networks in an SPR assay (Thesis section 3.3.1). *Ex vivo* transport assays in digitonin-permeabilized HeLa cells were conducted to elaborate whether NLS-NCs are indeed translocated through NPCs in a Ran-dependent manner [68].

Bodipy labelled NLS-NCs could not be detected in the nucleus when RanGDP was absent (Figure 4.13). Yet, a physiological concentration of RanGDP (5 μM) was sufficient to drive nuclear NLS-NC uptake, and 20 μM RanGDP enhanced the degree of uptake further. These results imply that in addition to the effects of the physico-chemical properties of the applied NC structures (*e.g.* size, shape or surface charge), the nuclear RanGTP concentration greatly affects the efficacy of nuclear import for NLS-NCs.

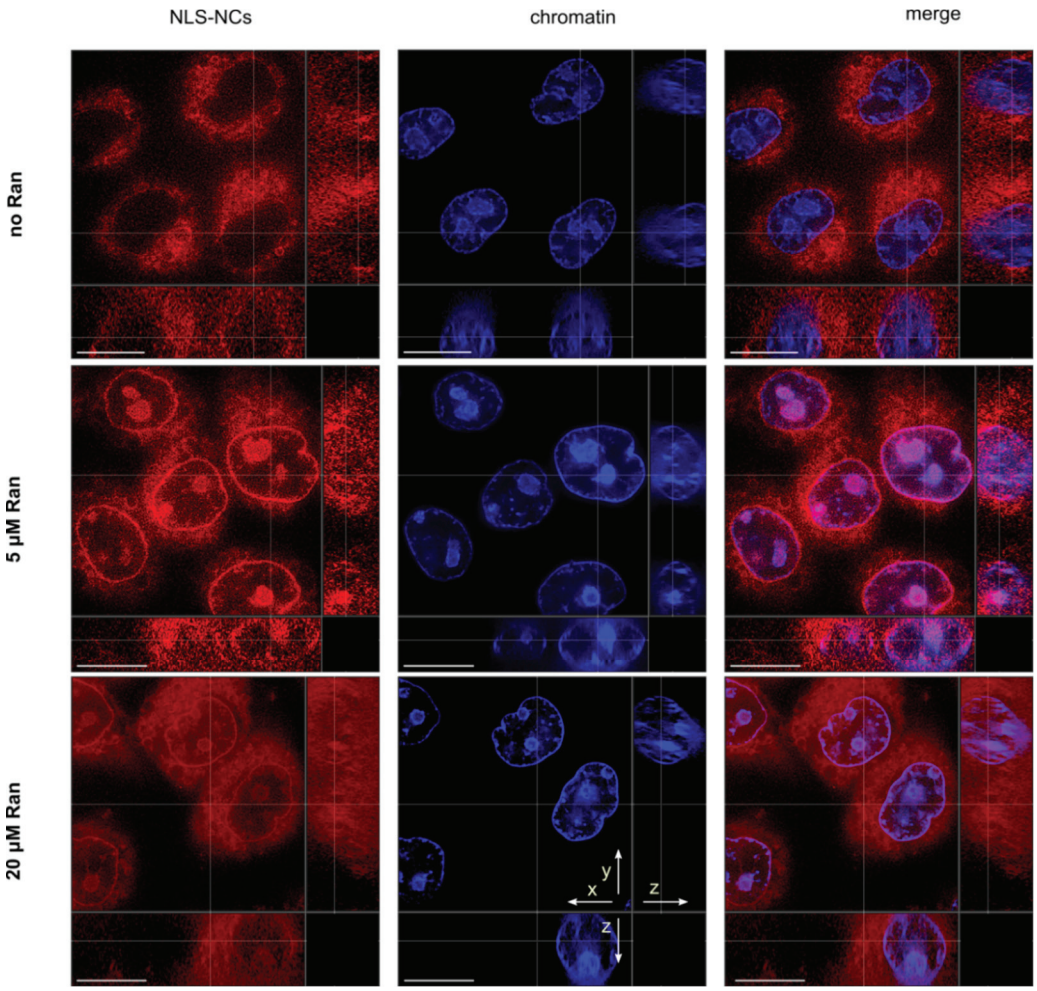

Figure 4.13 Nuclear uptake of NLS-NCs in permeabilized HeLa cells is Ran dependent. The NLS-NC nuclear import efficacy is visualized after 90 minutes incubation by wide-field fluorescence microscopy and appears highest at 20 µM Ran and lowest when Ran is absent. The scale bar is 10 µm.

Next, the same transport assay was applied to examine in more detail how the nuclear RanGTP concentration affects the NLS-NC nuclear uptake kinetics. To do so, the nuclear import of NLS-NCs was quantified at regular time intervals by assessing the intensity of Bodipy signal co-localized with the fluorescent DAPI chromatin label. From the recorded z-stacked image sets, the average nuclear fluorescence intensity per volume unit was determined using the *Imaris* module *ImarisCell*. This data was used to construct a curve of intensity over time for nuclear imported NLS-NC in each of the three Ran mix conditions (20 µM Ran, 5 µM Ran, no exogenous Ran).

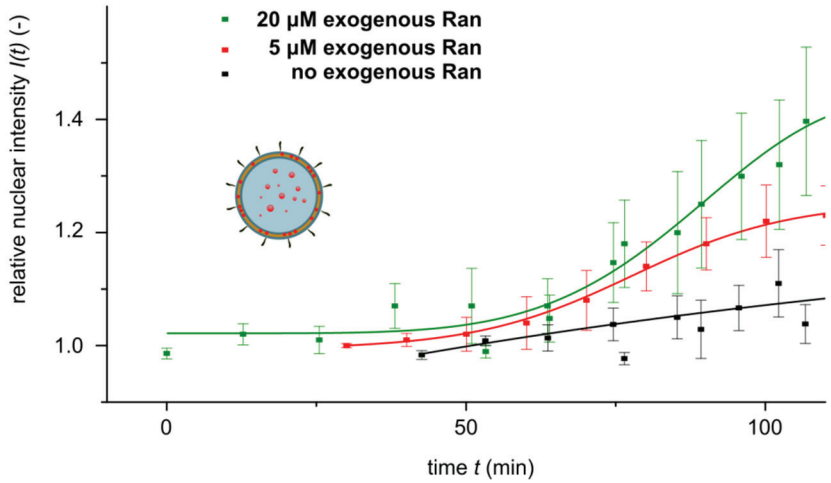

Figure 4.14 Nuclear import rate of NLS-NCs in permeabilized HeLa cells is Ran dependent. Here, quantitative time-laps fluorescence microscopy image analysis demonstrates increased nuclear import of NLS-NCs with increasing nuclear Ran concentration.

Increased nuclear import rates were observed for NLS-NCs added to permeabilized HeLa cells that were treated with increasing RanGDP concentrations (Figure 4.14). The import rate is highest in the presence of 20 µM Ran, and much reduced in the absence of Ran. It has previously been shown that IBB-conjugated quantum dots could explore the entire NPC in the absence of RanGTP, but that their probability of exit and release at the nuclear side was greatly increased in the presence of RanGTP [58]. Those experiments demonstrated that RanGTP is a critical regulator for NCT directionality. It is likely that the same effect is operating in the experiment described here. A high concentration of RanGTP at the nuclear NPC channel exit site should accelerate the dissociation of Kapα/β1•NLS-NC complexes, irreversibly releasing them into the nucleus, and giving rise to the observed increase in nuclear import rate.

In addition, the curves of relative nuclear intensity *vs*. time for the nuclear import of NLS-NCs in Figure 4.14 have a sigmoid form. This might be explained by occlusion of the NPC channel (61 nm) by the large-diameter NLS-NCs (67 nm) during import. Occlusion of the channel might sterically hinder exchange of Ran

through the NPC channels, perturbing the Ran cycle and thereby inhibiting further nuclear import.

This mechanism can be outlined in more detail as follows. The high rate of nuclear NC import at the beginning of the experiments is predominantly determined by the initial nuclear RanGTP concentration. As the time course proceeds, cargo release at the nuclear side of the NPC is accompanied by the formation of a new Kapβ1•RanGTP complex that binds with high avidity to the FG Nups. This reduces the concentration of free nuclear RanGTP. This would normally be replenished by the shuttling of NTF2•RanGDP from the cytoplasmic side followed by nucleotide exchange. However, if this process is prevented by occlusion of the NPC by NLS-NCs the concentration of free nuclear RanGTP would be steadily depleted. This depletion would reduce the rate of NLS-NC release at the nuclear side of the NPC on longer timescales, indicated by the sigmoid form of the time courses in Figure 4.14.

The slowing of nuclear import rates at long timescales could also be due to cargo depletion in the cytoplasm. However, the effect is less pronounced in the presence of 20 μM Ran compared 5 μM Ran, even though the NLS-NC cargo concentration equal in those experiments. This suggests that the import kinetics are more strongly influenced by RanGTP depletion than by NLS-NC cargo depletion.

4.5.3 The Ran regulated nuclear import is specific to NLS-cargoes

Next, the selectivity of nuclear import towards NLS-NCs cargo was investigated using the same transport assay with a physiological Ran concentration (5 μM). All other experimental conditions were as described previously (Thesis section 4.5.1) and a control experiment was also performed

using blank NCs. Nuclear accumulation of NCs was again monitored by quantifying the co-localization of NC fluorescence with DAPI fluorescence.

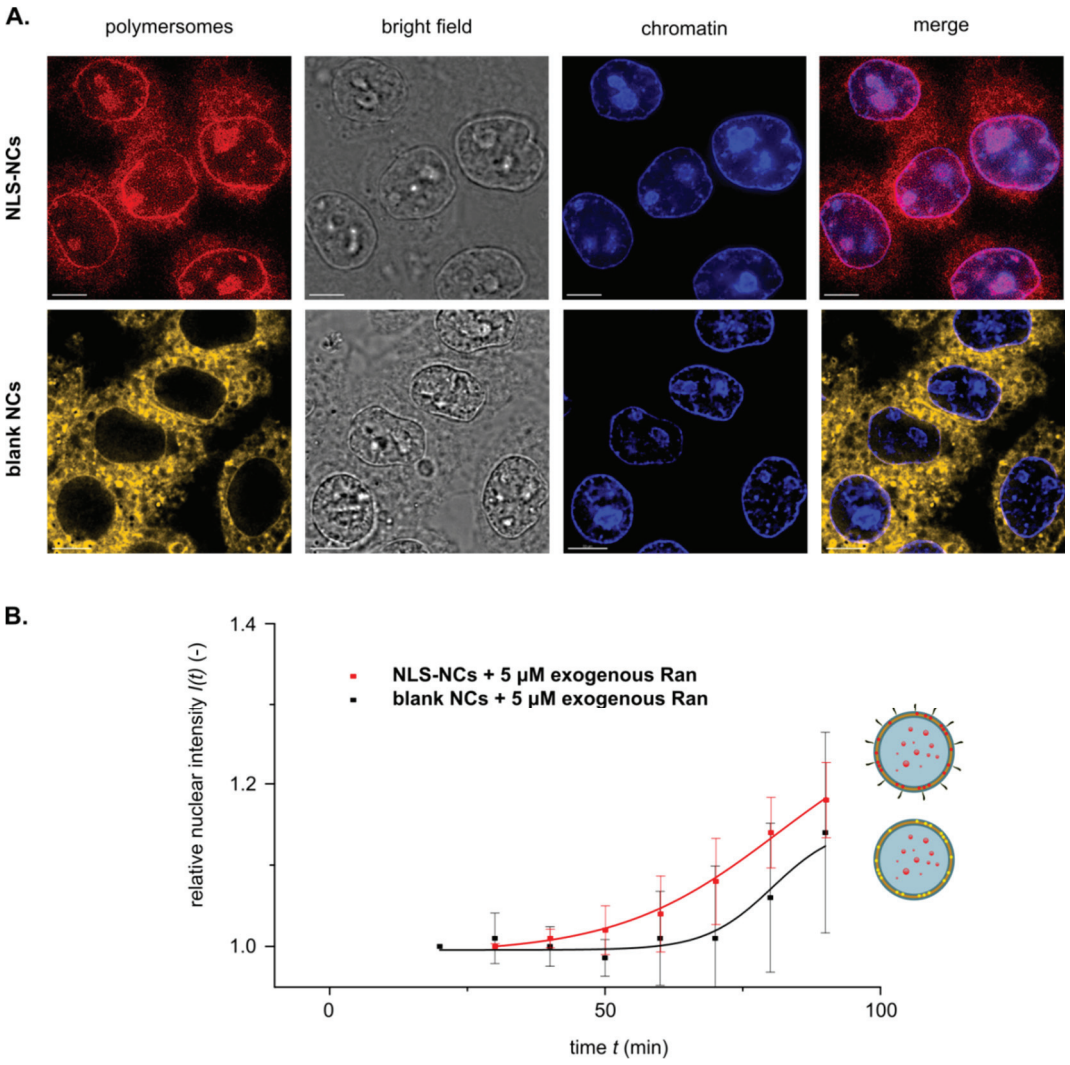

Figure 4.15 Ran regulates the nuclear import of NLS-NCs in permeabilized HeLa cells. A. Fluorescence microscopic images were recorded 90 minutes after the exogenous NC application and show NLS-NCs to accumulate inside cell nuclei. At the same 5 µM Ran concentration, blank NCs are largely blocked out the nuclei and primarily populate in the cells cytoplasm. The scale bar is 7 µm. **B.** On average, nuclear import is pronounced for NLS-NCs as compared to blank NCs, to see here on the determined steeper increase in relative nuclear intensity.

Merged fluorescence images recorded 90 minutes after exogenous NC application (Figure 4.15 A right column), clearly show that NLS-NC have been internalized in cell nuclei. An accumulation of NLS-NCs around the nucleoli is also

apparent, which is perhaps not surprising considering the charge complementarity between the positively-charged NLS-NCs (Thesis section 2.4.6) and the negatively charged rRNA in the nucleoli [198]. A further NLS-NC fraction can be observed in NPC transit, giving rise to a pronounced rim-staining of the HeLa cell nuclei. These observations are in good agreement with the cellular biodistribution found before using BioEM (see details in Figure 4.11). In contrast, blank NCs lacking the nuclear targeting NLS sequence predominantly accumulate in the cytoplasm, with relatively little fluorescence apparent in the nucleus suggesting that there is relatively little translocation. The rim-staining of the nucleus observed for NLS-NCs is also seen for blank NCs. However, it is likely that this arises not from the presence of large numbers of blank NCs in the NPC, but rather from the accumulation of blank NCs at the cytoplasmic side of the NE, as observed in BioEM experiments (see Figure 4.10). This FM analysis in combination with the BioEM described before confirm that the nuclear import of blank NCs is hindered, due to the absence of the NLS sequence and the fact that NCs exceed the cut-off size for passive diffusion through the NPC [199].

In addition, quantification of the time dependent nuclear import of NLS-functional *vs* blank NCs (Figure 4.15 B) revealed that over a time course of 90 minutes, NLS-NCs showed a pronounced uptake into cell nuclei. This, together with the nuclear NLS-NC import visualized in Figure 4.15 A, proves a selective Kap-NPC facilitated nuclear uptake pathway. In marked contrast, blank NCs followed significantly retarded import kinetics and did not begin to pass through the NE until 70 minutes.

4.6 Materials and methods

4.6.1 NC preparation and labelling

0.5 mg/ml ***NLS-NC*** and 0.5 mg/ml ***blank NC*** stock dispersions were prepared as described in Thesis section 2.3 and labelled with 1 μM lipophilic Bodipy 630/650 (Lumiprobe) or 1 μM lipophilic Nile Red 552/636, respectively. The lipophilic dyes were let intercalate spontaneously into the NCs membrane. After 30 minutes incubation, the NCs were purified from free dye by SEC through a commercial Sephadex G-25 column (GE Healthcare).

4.6.2 Protein expression, purification and labelling

The expression procedures of Kapα and Kapβ1 are to find in Thesis section 3.4.2 together with the labelling procedure of Kapβ1 with Atto-550. Also, the expression and purification of wild type (WT) Ran is outlined in Thesis section 3.4.2. In contrast to the already described formation of RanGTP was here the ***RanGDP*** construct generated by incubating WT Ran for 30 minutes in 10 mM Ethylenediaminetetraacetic acid (EDTA, Sigma-Aldrich) mixed with 1 mM guanosine diphosphate nucleotide (GDP, Sigma-Aldrich). All subsequent purification and characterization steps remained the same.

4.6.3 Cell culture

HeLa cells (epitheloid cervix carcinoma, human; ATCC, CCL-2) were cultured in Dulbecco's Modified Eagle Medium GlutaMAX^{TM}-I (DMEM, Gibco Life Sciences) and supplemented with 10 % v/v Fetal Bovine Serum (FBS, BioConcept), 100 units/ml Penicillin and 100 μg/ml Streptomycin (Sigma Aldrich). Cells were maintained at 37 °C and 5 % CO_2 atmosphere.

4.6.4 Live cell studies

Three-dimensional wide-field fluorescence microscopy import assay. HeLa cells were seeded in 8-well glass bottom μ-slides (Ibidi) using DMEM with 10 % v/v FBS and 1 %w/v Penicillin/Streptomycin as nutrition medium and grown until they reached a confluency of 50 – 80 %. In all live-cell fluorescence microscopy studies, cell nuclei were stained with Hoechst and the DMEM medium exchanged to a phenol red free one (Gibco). The cells were then transferred for imaging into a chamber platform mounted on top of an Olympus IX71 stand that was preheated to 37 °C and evacuated with 5 % CO_2 atmosphere. A DeltaVision core wide-field fluorescence microscope equipped with a photometrics CoolSNAP HQ^2 camera coupled to an interline CCD transfer was used for imaging and operated with *SoftWorx 4.12* software. An 60x oil objective was applied here. The excitation and emission wavelength were set for the individual fluorophores or markers to: Hoechst chromatin stain (390/ 18 nm ex/ 435/ 48 nm em), Nile Red blank NC label (542/ 27 nm ex/ 597/ 45 nm em) and Bodipy NLS-NC label (632/ 22 nm ex/ 679/ 34 nm em). To begin with the experimental import assay, a final concentration of 0.6 nM Bodipy 630/650 labelled NLS-NCs, 0.6 nM Nile Red 552/636 labelled blank NCs, or both 0.6 nM NLS-NCs and 0.6 nM blank NCs were added to the cell medium. The cellular uptake kinetics into the cell cytoplasm and eventually into the cell nuclei were followed over a time laps of 12 hours with images taken every 30 minutes. Cell studies were repeated at least 3 times for each experimental condition.

Electron microscopic import assay. HeLa cells were seeded in 100x21 mm cell-culture dishes (ThermoFischer) and grown in DMEM media containing 10 % v/v FBS and 1 % w/v Penicillin/Streptomycin until a substantial number of cells were obtained for electron microscopic (BioEM) analysis. The cells were then incubated for 12 hours at 37° and 5 % CO_2 atmosphere with 0.6 nM RR encapsulating NLS-NCs or 0.6 nM of RR encapsulating blank NCs. Thereafter, the

cells were washed with PBS three times and collected into cell pellets. The pellets were immediately frozen with Karnovsky fixative, embedded in Epon-resin and ultrathin cell sections prepared. The cuts were mounted onto Nickel grids and treated according to a regressive EDTA staining protocol (Bernhard, 1969 [200]). To do so, the thin sections were floated for 5 minutes over a 6 %age aqueous uranyl acetate solution. Rinsing with double distilled H_2Odd followed a second floating step on a 0.2 M EDTA/water solution. The pH of the solution was raised to 7.0 by adding 1 N sodium hydroxide drop by drop over a 30 minutes time course. The sections were rinsed again with H_2Odd and stained with lead citrate for 5 minutes before rinsing them another time with H_2Odd. The dried samples were imaged on a Philips CM100 device operated at 100 kV acceleration voltage and equipped with a CCD-camera.

4.6.5 Cell viability assay

Cell viability was determined using a CellTiter 96® AQueous One Solution Cell Proliferation Assay (MTS, Invitrogen) based on a standard protocol. HeLa cells were seeded in a 96 well plate (5 000 cells/well). After 24 hours, cells were dosed with increasing concentrations of blank NCs or NLS-NCs (0.6 nM, 1.2 nM and 1.8 nM, final concentrations) and incubated further for 48 hours. The MTS reagent (20 µl) was added to each well and after 2 hours absorbance at 490 nm was measured using a Spectramax plate reader. Background absorbance was subtracted from each well and data was normalized to control untreated cells. Experiments were done in quadruplicate (n = 4) and data was plotted using GraphPad Prism.

4.6.6 Permeabilized cell studies

Transport assay. The cell studies were conducted on plasma membrane perforated HeLa cells *via* three-dimensional wide-field fluorescence microscopy. Therefore, the cells were cultured in 8-well glass bottom μ-slides (Ibidi) to 50 – 80 % confluency using DMEM media mixed with 10 % v/v FBS and 1 % w/v Penicillin/Streptomycin. The cells were washed 3 times with PBS before treating them with digitonin solution (40 μg/ml in transport buffer) for exactly 5 minutes (Adam *et al.* 1990 [195]). This was followed by three washing steps with PBS buffer, cell nuclei staining with DAPI (Sigma-Aldrich) and another three times washing with PBS. Excess buffer was wicked off and the permeabilized cells incubated with 300 μl Ran mix for 30 minutes (containing 1 μM Kapβ1, 2 μM Kapα, a specified amount of RanGDP, 1 mM GTP (Roche), 1 μM NTF2, 100 μM ATP (Roche), 4 mM creatine phosphate (Roche), 20 U/ml creatine kinase (Roche)). The cells containing Ibidi dishes were transferred to a DeltaVision wide-field fluorescence microscope setup in away described before for the live cell experiments. To start the time-lapsed nuclear import studies, 30 μl of either 6 nM Bodipy 630/650 labelled NLS-NCs or 6 nM Nile Red 552/636 labelled blank NCs were added to the Ran mix solution to obtain a final NC concentration of 0.6 nM. Cellular internalization and nuclear import were then monitored for 120 minutes with images taken every 10 minutes. Studies on permeabilized cells were repeated at least 3 times for each experimental condition.

***Transport buffer (TB) preparation*.** The import assays were conducted in 20 mM HEPES (4-(2-hydroxyethyl)-1-piperazineethanesulfonic acid, Sigma-Aldrich) buffer at pH 7.3. The buffer contained a combination of 10 mM potassium acetate (Sigma-Aldrich) and 2 mM magnesium acetate (Merck) mixed with 1 mM ethylene glycol-bis(2-aminoethylether)-*N*,*N*,*N*'*N*'-tetraacetic acid (EGTA, Sigma-Aldrich), 2 mM dithiothreitol (DTT, ThermoFischer), 1 mM phenylmethanesulfonyl

fluoride (PMSF, Sigma-Aldrich), 1 mg/ml aprotinin (Sigma-Aldrich), 1 mg/ml pepstatin (ThermoFischer) and 1 mg/ml leupeptin (ThermoFischer).

4.6.7 Fluorescence image analysis

The time dependent nuclear NC import ability in permeabilized HeLa cells and in live HeLa cells was visualized with ***three-dimensional deconvolution fluorescence microscopy*****,** using the above described DeltaVision microscope setup (see Thesis section 4.6.4). For the image based nuclear NC import quantification, z-stacked image sets of NC treated cells were recorded at each the time-laps point. Fluorescence microscopic images were thereby recorded over a stack range of 15 μm at 0.35 μm z-intervals and reconstituted for further analysis using *Imaris* software with an integrated *ImarisCell* module. More specifically, the average signal intensity distribution of cell internalized nanocarriers was mapped based on the Bodipy 630/650 signal of NLS-NCs and respectively the Nile Red 552/636 signal of blank NCs. Nuclei imported NCs were co-localized with the fluorescent chromatin label Hoechst in live cells or the fluorescent chromatin label DAPI in permeabilized cells. This allowed quantifying the nuclear uptaken fluorescence intensity per volume unit. In doing so, the average time-dependent intensity evolution was reconstituted for all nanocarrier composites in at least 15 cells for all conducted experimental conditions. To compare import of NLS-NCs and blank NCs in living HeLa cell nuclei and separately the Ran dependent NLS-NCs import in permeabilized HeLa cells, time-laps intensity plots *I(t)* were normalized as to 1, as the starting point of nuclear detected NC import signals.

Chapter 5

Conclusions and Outlook

5 Conclusions and outlook

5.1 Conclusions

Polymersome-NCs bear great potential as non-viral systems for drug and gene delivery into cell nuclei. Payload integrity is a prerequisite for prospective biomedical applications. Cargo molecules, either integrated into the hydrophobic membrane or encapsulated in the aqueous lumen, should be directly delivered to the nucleus without modification or degradation. High NC stability and cargo loading capacity are therefore essential for uncorrupted nuclear targeting. These requirements demand thick polymeric membranes (> 5 nm) and large lumina (R_h > 25 nm), setting minimal dimensions for promising NC systems that may ultimately prove counterproductive due to the size restrictions for nuclear uptake. This Thesis work has shown that passive nuclear uptake of the inert polymersome-nanocarriers (blank NCs) across NPCs is constrained due to their diameter (~50 nm) and mass (~88 MDa). However, this limitation was overcome by employing active NCT mechanisms intrinsic to the cell. NCT offers a specific and efficient way to accumulate NCs modified with nuclear localization sequences (NLS-NC) within the nucleus. The presented investigations revealed that this facilitated uptake requires a cellular identification of the loaded NLS-NCs as authentic NCT cargo. This involves (i) the initial recognition of NLS on the NC surface by nuclear transport receptors (*e.g.* Kapα/β1), (ii) the association of Kapα/β1•NLS-NC complexes (Kap•NCs) to phenylalanine-glycine rich nucleoporin (FG Nup) assemblies *via* the Kaps and (iii) the RanGTP dissociation of Kapα/β1 from the Nup•Kap•NC complex, finally resulting in the release of NLS-NC into the cell nucleus.

Here, a holistic approach was followed that aimed to characterize and optimize every step of this process from the polymer synthesis, to their eventual

nuclear enrichment in the living cells. It was focused on examining step (i) to (iii) over multiple length and time scales by means of various *in vitro* and *in vivo* assays. To do so, NCs were rendered as authentic nuclear targeting systems. Specifically, a freshly synthesized, biocompatible $PMOXA_4$-$PDMS_{44}$-$PMOXA_4$ triblock-copolymer was mixed on-demand with a novel maleimide derivate to form a ~8 nm thick nanocarrier membrane that could be conjugated at its surface to NLS peptide tags (see Figure 2.10). The synthesized polymeric compounds and their yields were characterized by ^{1}H NMR (see Figure 2.3and Figure 2.6), and successful blank NC and NLS-NC formation was verified by TEM, cryo-EM, DLS and SLS (see Figure 2.11). Fluorescent model payloads (membrane-associated Bodipy and luminal RR) were used to make NCs amenable to characterization by fluorescence methods. dcFLCCS demonstrated that both payloads are integral constituents co-located in individual NCs (see Figure 2.12). Moreover, TEM, DLS and SLS studies showed that cargo loading did not alter the morphology of NCs (Figure 3.5).

Step(i) – the recognition of NLS on the NC surface by Kapα/β1 – was examined by dcFLCCS (see Figure 3.2). This yielded a maximum of 57 Kapα/β1 complexes per NLS-NC at saturation and a Kaps•NLS dissociation constant (K_D) of ≤ 0.4 nM, consistent with literature values [201]. Kapα/β1 complexes were found to interact exclusively with the NLS-, since blank NCs did not bind Kaps (Figure 3.4). Together, these observations show that NLS-NCs are indeed recognized as authentic cargo for nuclear import by the Kapα/β1 complexes, a crucial step to hijack the NCT mechanisms for NC based delivery systems.

Step (ii) – the association of Kap•NLS-NC to NPC – was investigated by SPR *in vitro* (Figure 3.6) and BioEM *ex vivo* (Figure 4.9). The binding of the Kapα/β1•NLS-NCs complex to immobilized FG-Nups provoked a considerably larger amplitude of SPR response than Kapα/β1 complexes alone, due to the

additional mass of the NCs. However, the apparent dissociation constants were comparable, in the range 18 ± 9 nM (towards Nup153, see also Table 3.3). A control mixture of blank NCs together with Kapα/β1 did not exhibit the same increased amplitude of response, signifying a lack of binding between blank NCs and Kapα/β1. Neither blank NCs nor NLS-NCs showed FG Nup-binding in the absence of Kapα/β1 (Figure 3.7). Thus, on average 57 Kapα/β1 complexes are bound to a single NLS-NC and are responsible for selective binding to FG Nups. Employing BioEM with elaborate EDTA regressive staining procedures allowed NCs to be resolved in thin sections (< 50 nm) of HeLa cells. To our knowledge, this is the first time that the nuclear uptake of polymersome-nanocarriers through NPCs has been visualized (Figure 4.9). While 25 % of the overall imaged NLS-NCs (n_{total} = 292) were captured during their passage across the NE, less than 5 % of blank NCs (n = 166) were found inside NPCs (Figure 4.11). Importantly, NLS-NCs maintain their structural integrity while accommodated within NPC structures, probably due to the high membrane stability of vesicles prepared from amphiphilic polymers. This stability may contribute to compression of FG Nups and potentially facilitate the passage of the app. 60 nm NLS-NCs. NPCs are thus capable of translocating cargo complexes that are equal to their own supramolecular mass (60 – 120 MDa per NPC versus ~88 MDa per NC).

Step (iii) – the RanGTP dissociation of Kapα/β1 from the Nup•Kap•NLS-NC complex – was primarily investigated by the means of quantitative time-lapse fluorescence microscopy in permeabilized HeLa cells (Figure 4.11). When RanGTP was absent, NLS-NCs gave pronounced NE rim staining due to their interaction with NPCs, but NLS-NCs were not detected in the nucleus. On the other hand, application of a Ran mix, that supplies RanGDP to produce RanGTP by nuclear RanGEF, resulted in release and therefore accumulation of NLS-NC in the nucleus, and correlated with increasing RanGTP levels. Thus, NLS-NCs readily permeate the NE, whereas neither fluorescence time-lapse studies in living HeLa cells (Figure **4.3**)

nor BioEM investigations (Figure 4.10) captured substantial nuclear uptake of blank NCs - despite the availability of RanGTP. While the BioEM analysis shows that over 50 % of the NLS-NC were located on the nucleoplasmic side of the NE, only 4 % of blank NCs were found in the nucleus (Figure 4.11). The NLS-NCs thereby preserve their vesicular structure and exhibit the stability required to deliver cargo molecules to the nucleus without being degraded or mechanically corrupted.

In conclusion, a novel polymersome-nanocarrier based drug delivery system was presented in this Thesis that exploits active nucleocytoplasmic transport mechanisms intrinsic to eukaryotic cells. It was shown for the first time that polymeric NCs based on PMOXA-PDMS-PMOXA retain their structural integrity throughout the process, from endocytosis over NPC passage to the nuclear release. The outlined studies on living human cells demonstrated that NLS-NCs successfully target the nucleus (Figure 4.2) while exerting minimal cytotoxicity (Figure 4.12) even 48 h after cellular application. On this basis, various small molecular entities could be encapsulated within the NCs making them superior for the development of new polymeric therapy forms. *En route*, a follow up could assess the pharmacokinetics of our NLS-NCs loaded with chemotherapeutics in various animal models. Such endeavor requires a controlled, spatiotemporal cargo release which shall be part of the next outlook section.

5.2 Outlook: Opening of nuclear targeting NCs

As identified before by ultrastructural BioEM investigations, NLS-NCs remain intact while bypassing the NPCs selectivity barrier for their nuclear internalization. Such superior structural integrity is prerequisite for the delivery of cargo compounds that are encapsulated within the NC cavities and is essential to protect those compounds from premature degradation. The therapeutic activity of nuclei imported drugs is however limited for those entities that are kept entrapped in the NC structure.

Thus, there is a demand for the development of stimuli-responsive NLS-NCs that can release their specific cargo at desired location. For this reason, NLS-NCs were made amenable to spatiotemporal light-triggered drug release. A strategy was developed to photothermally force NCs opening by the means of an encapsulated chemical stimulus. Specifically, this undertaking employs dcFLCCS with high 530 nm laser powers to induce and simultaneously track the photothermal NC rupture. First results demonstrate that NC opening is controlled by the presence of the chemical stimulus and by the power of the applied laser light. Experimental details and generated results are however removed from the Thesis with recommendation of UNITECTRA (University of Basel) and Prof. Lim to review whether this invention contains patentable intellectual property.

The potential of NLS-NCs for applications in nuclear cargo deliver and the spatiotemporal release of therapeutic entities has yet been realized. Next steps could therefore comprise publishing results in a patent or research article and to further optimize the existing NLS-NC platform for the development of novel bio-medical therapy forms.

Appendix

6 Appendix

6.1 Experimental part

6.1.1 Theoretical background static light scattering

Laser light scattering spectroscopy is a technique that measures the time dependent thermal fluctuation behaviour of particles in fluid systems. Due to discrepancies in the refractive indices between the dispersant n_0 and the dispersed particles n, the particles motion can be visualized as temporal scattered light intensities. More specifically, static light scattering (SLS) measures the angular dependency of scattered light as described in the famous Zimm-equation

$$\frac{K\,\omega}{R_{ex}} = \frac{1}{M_w}\left(1 + \frac{R_g^2}{3}q^2\right)(1 + 2\bar{B}_2\omega). \quad \text{(A1)}$$

It is based on the absolute time-averaged scattering intensity that relates in $K\omega/R_{ex}$ the concentration of the polymersome dispersion ω to the Rayleigh excess ratio R_{ex} that corrects for the scattering signal contribution of the pure solvent. K is an optical constant factor

$$K = \frac{4\pi^2 n_0^2}{N_A\lambda^4}\left(\frac{dn}{dc}\right)^2 \quad \text{(A2)}$$

that includes sample specific optical parameters as the refractive index increment *dn/dc* as well as the refractive index of the dispersant. It further contains a device specific optical parameter, here the wavelength of the incident laser beam in vacuo λ. The entire term is normalized to one mole *via* the Avogadro constant N_A. According to the Zimm-equation, the intensity is related to the angular dependent scattering vector q

$$q = \frac{4\pi n_0}{\lambda}\sin\left(\frac{\theta}{2}\right) \quad \text{(A3)}$$

where θ is the angle between the incident light and the scattering light.

From equation A1 it becomes obvious that the weight average molecular mass M_w of the studied particles can be directly obtained from R_{ex} / $K\omega$ at θ = 0

and $\omega = 0$. However, the particles scattering intensity in their absence (when the concentration ω is 0) and the particles forward scattering (when the laser beam at $\theta = 0$ is directly opposing the detector) is only theoretically predictable. The particles scattering intensities are therefore measured at finite ω and θ which allows constructing the Zimm-plot. To do so, $K\omega/R_{ex}$ is plotted as a function of $(q^2 + c\omega)$ where *c* declares an arbitrary factor to separate the angular dependent curves from different concentrations. From the double extrapolation to $\omega = 0$ (equation A4) and $q = 0$ (*i.e.* $\theta = 0$, equation A5), single particle properties as the molecular weight M_w, the radius of gyration R_g and the second viral coefficient B_2 can be determined.

$$\frac{K\,\omega}{R_{ex}} = \frac{1}{M_w} + \frac{R_g^2 . q^2}{3\,M_w} \tag{A4}$$

$$\frac{K\,\omega}{R_{ex}} = \frac{1}{M_w} + \frac{2\bar{B}_2\omega}{M_w} \tag{A5}$$

The molar mass M_w is obtained based on the ordinates intercept of the extrapolated functions of equation A4 and equation A5 from $\frac{1}{M_w}$ (ideally at the same point), whereas the slope of equation A4 is a function of the radius of gyration R_g and the slope of equation A5 a function of the second viral coefficient B_2.

For particles with very high molecular weight, the ordinate intercept values for extrapolated $\omega = 0$ and $\theta = 0$ becomes very small and increases the associated fitting and extrapolation error. Consequently, the error of the evaluated particle properties becomes larger as well. This limitation intrinsic to the Zimm-plot was first treated by Berry, who simply conducted an axis transformation by applying a square root to the Zimm-relation. Thus, the correspondingly modified Zimm-function writes

$$\sqrt{\frac{K\,\omega}{R_{ex}}} = \sqrt{\frac{1}{M_w}\left(1 + \frac{R_g^2}{3}q^2\right)(1 + 2\bar{B}_2\omega)}. \tag{A6}$$

The extrapolated $\omega = 0$ and $q = 0$ are now given by

$$\sqrt{\frac{K\,\omega}{R_{ex}}} = \sqrt{\frac{1}{M_w} + \frac{R_g^2\,q^2}{3\,M_w}} \text{ and} \tag{A7}$$

$$\sqrt{\frac{K\,\omega}{R_{ex}}} = \sqrt{\frac{1}{M_w} + \frac{2\bar{B}_2\omega}{3\,M_w}}. \tag{A8}$$

and yield the molecular mass from the intercepts $\sqrt{\frac{1}{M_w}}$. As the Berry method increases the plots accuracy, it is often employed for LS analysis where particles with radii > 50 nm are studied [202].

6.1.2 Lifetime correction protocol in FCCS measurements

Fluorescence cross—correlation spectroscopy (FCCS) is a very powerful technique that allows studying molecular interactions, such as binding-, cleavage-events or molecular co-localizations based on the molecules dynamics in solution. The accuracy in FCCS measurements however suffers tremendously from false-positive and false negative cross-correlation artefact, that can arise from inter-channel cross-talk between the studied fluorophores or respectively a lack of overlaying detection volumes [150]. Fluorescence lifetime cross-correlation spectroscopy (FLCCS) is essentially a combination of conventional FCCS that uses time-correlated single photon counting (TCSPC) to eliminate false-correlated or false-uncorrelated signals. Hence, in this Thesis work, lifetime correction was used as integral part to all FCCS measurements and was conducted in the following described manner:

I. Fluorescence intensity fluctuation time traces $F_{uncorrected}(t)$ were recorded in the 530 (red) and the 640 (far-red) channel, and the initial auto-correlation *AC* and cross-correlation *CC* curves constructed with SymPhoTime 64 software.

II. Parallel to $F_{uncorrected}(t)$, TCSPC was used to generate photon arrival time histograms, which were plotted and fitted with SymPhoTime64 as well. The simplest case is a first-order exponential tail fit function

$$[S_1] = [S_1]_0 \exp\left(-\frac{t}{\tau_L}\right) \quad \text{(A9)}$$

that relates the time evolution of a singlet electronic exited state $[S_1]$ to its initial population $[S_1]_0$ and characteristic lifetime τ_L [203]. For multi-component fluorescent lifetime spectra, an *n*-exponential model function is applied

$$I(t) = I_{baseline} + \sum_{i=0}^{n-1} A_i exp\left(-\frac{t-t_0}{\tau_{L,i}}\right) \quad \text{(A10)}$$

to deconvolute the sum *I(t)* of multiple exponential decays and their respective fluorescence lifetimes $\tau_{L,i}$. Here, t_0 denotes the variable zero-time shift, $I_{baseline}$ is the correction factor for background signal (*e.g.* afterpulsing or dark counts) and the amplitude A_i is weighting of the intensity fraction of component i to the overall decay amplitude at given time *t*.

III. Contrary to (I.), where each detected photon contributes equally to $F_{uncorrected}(t)$, lifetime spectra are employed to weight the contribution of each photon to a lifetime corrected intensity fluctuation time trace $F(t)$ depending on their arrival time. The lifetime corrected auto-correlation $G_{AC}(\tau)$ and cross-correlation $G_{CC}(\tau)$ functions than simply write as

$$G_{AC}(\tau) = \frac{\langle \delta F(t) \cdot \delta F(t+\tau) \rangle}{\langle F(t) \rangle^2} \quad \text{(A11)}$$

$$G_{CC}(\tau) = \frac{\langle \delta F_{530}(t) \cdot \delta F_{640}(t+\tau) \rangle}{\langle F_{530} \rangle \langle F_{640} \rangle}. \quad \text{(A12)}$$

In the described context, angled brackets are denoting for the time averaged intensity over the entire acquisition time.

6.1.3 NLS-NC co-encapsulation with RR and Bodipy

FCCS measurements that were conducted to specify NLS-NC co-encapsulation with two cargo compounds (RR and Bodipy) were essentially lifetime corrected to ensure high result accuracy. To start with, fluorophore specific lifetime decays that were needed for lifetime corrections were recorded for polymersomes that carried only one of the two payloads, either RR or Bodipy. Therefore, the RR carrying NLS-NCs were prepared as described in Thesis section 2.3. `Empty` – thus only PBS encapsulating – polymersomes were manufactured in similar way however here pure PBS used for rehydration. Membrane labelling of the preformed polymersomes was achieved by adding 200 nM Bodipy to a 0.5 mg/ml polymersome dispersion. In brief, the so prepared two NC dispersions were analyzed for underlying TCSPC radiative decays and fit with equation A9 or equation A10 for characteristic lifetimes τ. Simultaneously, ACs were recorded, lifetime corrected and fit with the one component model equation 2.1. All data were evaluated for the polymersomes hydrodynamic radii using equation 2.2.

With the above described protocol, it was investigated how the fluorescence lifetime changes with its surrounding environment (in solution *vs*. polymersome associated, Figure 6.1 A and B) and how the incorporation of dye molecules into polymersomes structure changes the overall diffusional behavior (Figure 6.1 C and D). Importantly, encapsulated RR diffuses substantially slower than RR dissolved in PBS. Corresponding diffusion constants of D = 7.6 ± 3.3 $\mu m^2/s$ (R_h = 31.9 ± 18.4 nm) and respectively D = 455 ± 21 $\mu m^2/s$ (R_h = 0.51 ± 0.02 nm) were found. In the same manner, the mobility of Bodipy decreases from D = 359 ± 25 $\mu m^2/s$ (with R_h = 0.81 ± 0.06 nm) whilst dissolved in PBS to D = 2.00 ± 0.11 $\mu m^2/s$ (R_h = 23.04 ± 1.27 nm) once associated to the polymersome membrane.

Altogether, the recorded TCSPC decays and the measured FLCS curves demonstrated separately the incorporation of either RR or Bodipy into polymersome structure.

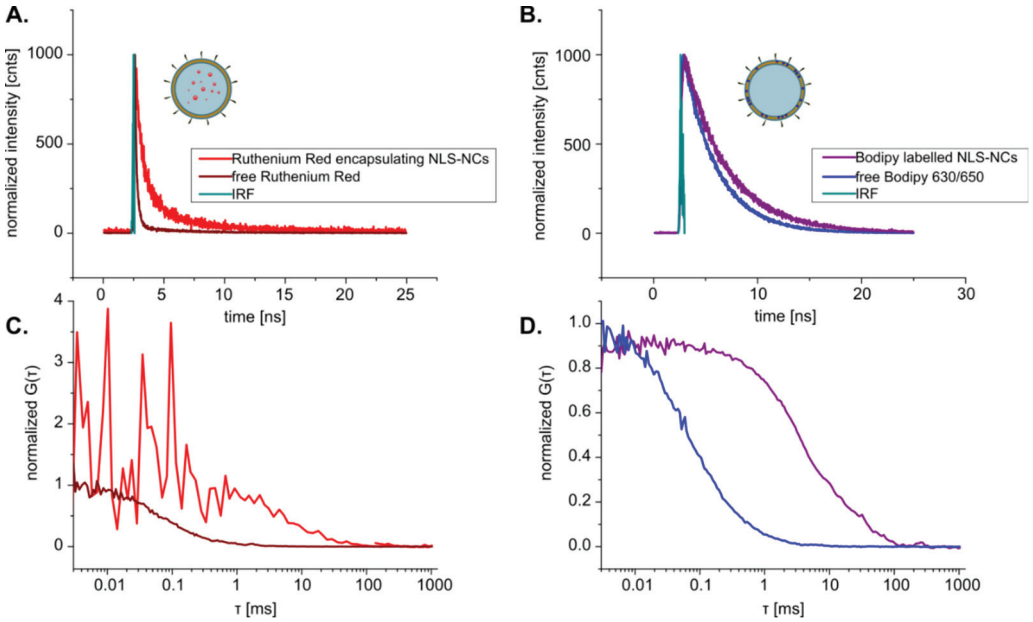

Figure 6.1 Time resolved fluorescence spectroscopy was used to verify the incorporation of either RR or Bodipy into NLS-NCs. First, lifetime decays were recorded for **A.** RR encapsulating NLS-NCs in channel 530 and **B.** Bodipy labelled NLS-NCs in channel 640. The normalized lifetime spectra are plotted together with the respective free dyes and show each a significant shift towards longer exponential decay times. The green graphs in A. and B. are displaying the instrument response function (IRF) of the used measurement system. Besides the apparent shift in lifetime, dye encapsulation into polymersomes leads to a shift towards longer correlation times to see on the lifetime corrected ACs of **C.** RR in NLS-NCs as compared to free RR and **D.** Bodipy encapsulating NLS-NCs against free Bodipy.

Table 6.1 Diffusional behavior and TCSPC lifetime characteristics of RR and Bodipy free in solution *vs*. polymersome encapsulated.

Time Resolved Fluorescence Spectroscopy		**FLCS Diffusion Behavior**			**TCSPC Fluorophore Lifetimes**	
		D [μm²/s]	A_{rel} [-]	R_h [nm]	τ [ns]	A_{rel} [-]
Channel 530	free Ruthenium Red	455 ± 21	1	0.5 ± 0.0	3.90 ± 0.13 0.21 ± 0.01	0.088 ± 0.002 0.912 ± 0.002
	Ruthenium Red encapsulating NLS-NCs	7.6 ± 3.3	1	31.9 ± 18.4	3.60 ± 0.55 0.53 ± 0.04	0.192 ± 0.025 0.808 ± 0.025
Channel 640	free Bodipy	359 ± 25	1	0.8 ± 0.1	3.98 ± 0.04	1
	Bodipy labelled NLS-NCs	2.0 ± 0.1	1	23.0 ± 1.3	4.11 ± 0.01	1

Furthermore, measuring either RR or Bodipy encapsulating polymersomes in dcFLCCS mode allows estimating the efficacy and reliability of the applied method itself. After lifetime correction, no signal is expected for only RR encapsulating polymersomes in the 640 channel and *vice versa* no signal is expected for only Bodipy encapsulating polymersomes in the 530 channel. Again, the lifetimes for RR encapsulating polymersomes in Figure 6.1 A and for Bodipy encapsulating polymersomes in Figure 6.1 B were used to lifetime correct polymersome samples that encapsulate only RR or only Bodipy. A typical late AC decay for 36.7 ± 6.4 nm (from D_{530} = 6.3 ± 1.1 $\mu m^2/s$) large objects is apparent for RR encapsulating polymersomes (Figure 6.2 B). After and even before lifetime correction, no signal is detected in channel 640 and hence the two channels do not interact *via* parasitic cross-talk. It is assumed that the signals between the two channels do not cross-correlate. In channel 530 however, RR exhibits strong triplet blinking in the sub-μs range which becomes even more apparent after signal correction. In case of the studied Bodipy labelled polymersomes, the typical late decaying AC was found in channel 640 and is associated to a hydrodynamic radius of 42.0 ± 2.3 nm (from D_{640} = 5.5 ± 0.3 $\mu m^2/s$). Before lifetime correction, another faster diffusing component is observed in channel 530, which partially cross-correlates with the Bodipy signal in channel 640 (Figure 6.2 C) Yet correction against the RR lifetime in channel 530 almost entirely subtracted all detected signal such that the degree of cross-correlated signal approaches zero.

The lifetime correction in combination with a time-gated detection assured that parasitic signals coming from either correlated bleed through, or un-correlated background do not bias the cross-correlation. The detected signal cross-correlation between channel 530 and 640 is originated by co-encapsulation of RR and Bodipy within one and the same polymersome structure (Figure 6.2 A).

This example impressively shows how accurate signal sorting based on TCSPC arrival time decays proceeds and implies in turn that in this set of experiments, all lifetime corrected signals can be reliably related to the fluorophore of interest.

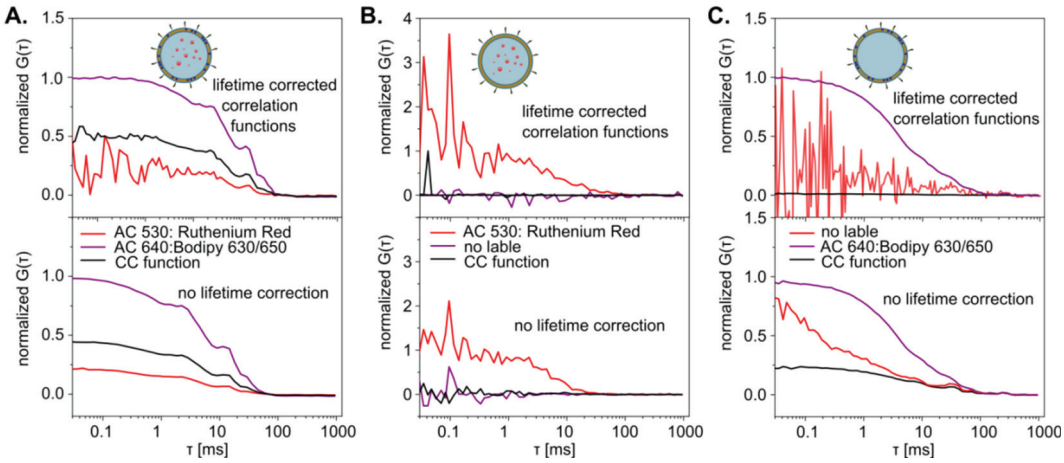

Figure 6.2 Lifetime corrected AC and CC functions (upper panel) imply co-encapsulation of Ruthenium Red and Bodipy 630/650 in the same NLS-NC. FLCCS date are opposed to the uncorrected raw data (bottom panel) for polymer vesicles that **A.** co-encapsulate Ruthenium Red and Bodipy 630/650, **B.** Ruthenium Red only and **C.** Bodipy 630/650 only.

6.1.4 UV/VIS-absorption spectrum of RR

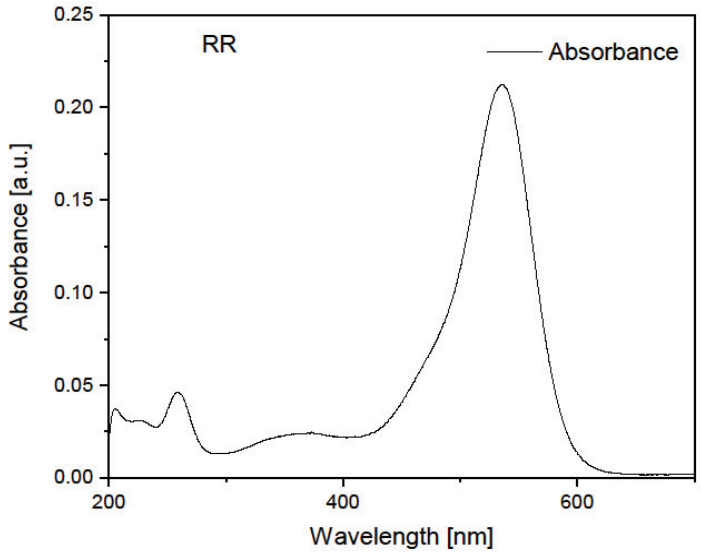

Figure 6.3 UV/VIS-absorption spectrum of RR in PBS with a λ_{max} at visible 536 nm.

6.2 References

1. Discher, D.E. and A.J.S. Eisenberg, *Polymer vesicles.* 2002. **297**(5583): p. 967-973.
2. Bermudez, H., D. Hammer, and D. Discher, *Effect of bilayer thickness on membrane bending rigidity.* Langmuir, 2004. **20**(3): p. 540-543.
3. Vujica, S., et al., *Nucleocytoplasmic transport: a paradigm for molecular logistics in artificial systems.* CHIMIA International Journal for Chemistry, 2016. **70**(6): p. 413-417.
4. Mikhalevich, V., et al., *Bio-inspired Polymer Membranes*, in *Bio-inspired Polymers*. 2016, Royal Society of Chemistry. p. 221-258.
5. Wente, S.R. and M.P. Rout, *The nuclear pore complex and nuclear transport.* Cold Spring Harbor perspectives in biology, 2010. **2**(10): p. a000562.
6. Blobel, G., *Protein targeting (Nobel lecture).* Chembiochem, 2000. **1**(2): p. 86-102.
7. Kabachinski, G. and T.U. Schwartz, *The nuclear pore complex–structure and function at a glance.* J Cell Sci, 2015. **128**(3): p. 423-429.
8. Fahrenkrog, B. and U. Aebi, *The nuclear pore complex: nucleocytoplasmic transport and beyond.* Nature Reviews Molecular Cell Biology, 2003. **4**(10): p. 757.
9. Tran, E.J. and S.R. Wente, *Dynamic nuclear pore complexes: life on the edge.* Cell, 2006. **125**(6): p. 1041-1053.
10. Frenkiel-Krispin, D., et al., *Structural analysis of a metazoan nuclear pore complex reveals a fused concentric ring architecture.* Journal of molecular biology, 2010. **395**(3): p. 578-586.
11. Hoelz, A., E.W. Debler, and G. Blobel, *The structure of the nuclear pore complex.* Annual review of biochemistry, 2011. **80**: p. 613-643.
12. Stewart, M., *Molecular mechanism of the nuclear protein import cycle.* Nature reviews Molecular cell biology, 2007. **8**(3): p. 195.
13. Paine, P.L., L.C. Moore, and S.B. Horowitz, *Nuclear envelope permeability.* Nature, 1975. **254**(5496): p. 109.
14. Bayliss, R., T. Littlewood, and M. Stewart, *Structural basis for the interaction between FxFG nucleoporin repeats and importin-β in nuclear trafficking.* Cell, 2000. **102**(1): p. 99-108.
15. Bednenko, J., G. Cingolani, and L. Gerace, *Importin β contains a COOH-terminal nucleoporin binding region important for nuclear transport.* J Cell Biol, 2003. **162**(3): p. 391-401.
16. Ma, J. and W. Yang, *Three-dimensional distribution of transient interactions in the nuclear pore complex obtained from single-molecule snapshots.* Proceedings of the National Academy of Sciences, 2010. **107**(16): p. 7305-7310.

17. Ribbeck, K. and D. Görlich, *Kinetic analysis of translocation through nuclear pore complexes.* The EMBO journal, 2001. **20**(6): p. 1320-1330.
18. Siebrasse, J.P. and R. Peters, *Rapid translocation of NTF2 through the nuclear pore of isolated nuclei and nuclear envelopes.* EMBO reports, 2002. **3**(9): p. 887-892.
19. Xu, D., A. Farmer, and Y.M. Chook, *Recognition of nuclear targeting signals by Karyopherin-β proteins.* Current opinion in structural biology, 2010. **20**(6): p. 782-790.
20. Boulikas, T., *Putative nuclear localization signals (NLS) in protein transcription factors.* Journal of cellular biochemistry, 1994. **55**(1): p. 32-58.
21. Kopito, R.B. and M. Elbaum, *Reversibility in nucleocytoplasmic transport.* Proceedings of the National Academy of Sciences, 2007. **104**(31): p. 12743-12748.
22. Yang, W., J. Gelles, and S.M. Musser, *Imaging of single-molecule translocation through nuclear pore complexes.* Proceedings of the National Academy of Sciences, 2004. **101**(35): p. 12887-12892.
23. Yang, W. and S.M. Musser, *Nuclear import time and transport efficiency depend on importin β concentration.* The Journal of cell biology, 2006. **174**(7): p. 951-961.
24. Schwoebel, E.D., et al., *Ran-dependent signal-mediated nuclear import does not require GTP hydrolysis by Ran.* Journal of Biological Chemistry, 1998. **273**(52): p. 35170-35175.
25. Mehlin, H., B. Daneholt, and U. Skoglund, *Translocation of a specific premessenger ribonucleoprotein particle through the nuclear pore studied with electron microscope tomography.* Cell, 1992. **69**(4): p. 605-613.
26. Mosammaparast, N. and L.F. Pemberton, *Karyopherins: from nuclear-transport mediators to nuclear-function regulators.* Trends in cell biology, 2004. **14**(10): p. 547-556.
27. Vetter, I.R., et al., *Structural view of the Ran–importin β interaction at 2.3 Å resolution.* Cell, 1999. **97**(5): p. 635-646.
28. Cingolani, G., et al., *Structure of importin-β bound to the IBB domain of importin-α.* Nature, 1999. **399**(6733): p. 221.
29. Macara, I.G., *Transport into and out of the nucleus.* Microbiol. Mol. Biol. Rev., 2001. **65**(4): p. 570-594.
30. Weis, K., *Regulating access to the genome: nucleocytoplasmic transport throughout the cell cycle.* Cell, 2003. **112**(4): p. 441-451.
31. Conti, E., et al., *Crystallographic analysis of the recognition of a nuclear localization signal by the nuclear import factor karyopherin α.* Cell, 1998. **94**(2): p. 193-204.
32. Cingolani, G., et al., *Molecular basis for the recognition of a nonclassical nuclear localization signal by importin β.* Molecular cell, 2002. **10**(6): p. 1345-1353.

33. Lee, S.J., et al., *The structure of importin-ß bound to SREBP-2: nuclear import of a transcription factor.* Science, 2003. **302**(5650): p. 1571-1575.
34. Christie, M., et al., *Structural biology and regulation of protein import into the nucleus.* Journal of molecular biology, 2016. **428**(10): p. 2060-2090.
35. Kapinos, L.E., et al., *Karyopherins regulate nuclear pore complex barrier and transport function.* J Cell Biol, 2017. **216**(11): p. 3609-3624.
36. Falces, J., et al., *Recognition of nucleoplasmin by its nuclear transport receptor importin α/β: insights into a complete import complex.* Biochemistry, 2010. **49**(45): p. 9756-9769.
37. Conti, E., C.W. Müller, and M. Stewart, *Karyopherin flexibility in nucleocytoplasmic transport.* Current opinion in structural biology, 2006. **16**(2): p. 237-244.
38. Fukuhara, N., et al., *Conformational variability of nucleo-cytoplasmic transport factors.* Journal of Biological Chemistry, 2004. **279**(3): p. 2176-2181.
39. Terry, L.J., E.B. Shows, and S.R. Wente, *Crossing the nuclear envelope: hierarchical regulation of nucleocytoplasmic transport.* Science, 2007. **318**(5855): p. 1412-1416.
40. Maul, G.G. and L. Deaven, *Quantitative determination of nuclear pore complexes in cycling cells with differing DNA content.* The Journal of cell biology, 1977. **73**(3): p. 748-760.
41. Sakiyama, Y., et al., *Spatiotemporal dynamics of the nuclear pore complex transport barrier resolved by high-speed atomic force microscopy.* Nature nanotechnology, 2016. **11**(8): p. 719.
42. Reichelt, R., et al., *Correlation between structure and mass distribution of the nuclear pore complex and of distinct pore complex components.* The Journal of cell biology, 1990. **110**(4): p. 883-894.
43. Elad, N., et al., *Structural analysis of the nuclear pore complex by integrated approaches.* Current opinion in structural biology, 2009. **19**(2): p. 226-232.
44. Stoffler, D., et al., *Cryo-electron tomography provides novel insights into nuclear pore architecture: implications for nucleocytoplasmic transport.* Journal of molecular biology, 2003. **328**(1): p. 119-130.
45. Rout, M.P., et al., *The yeast nuclear pore complex: composition, architecture, and transport mechanism.* The Journal of cell biology, 2000. **148**(4): p. 635-652.
46. Cronshaw, J.M., et al., *Proteomic analysis of the mammalian nuclear pore complex.* The Journal of cell biology, 2002. **158**(5): p. 915-927.
47. Akey, C.W. and M. Radermacher, *Architecture of the Xenopus nuclear pore complex revealed by three-dimensional cryo-electron microscopy.* The Journal of Cell Biology, 1993. **122**(1): p. 1-19.
48. Eibauer, M., et al., *Structure and gating of the nuclear pore complex.* Nature communications, 2015. **6**: p. 7532.
49. Grossman, E., O. Medalia, and M. Zwerger, *Functional architecture of the nuclear pore complex.* Annual review of biophysics, 2012. **41**: p. 557-584.

50. Terry, L.J. and S.R. Wente, *Flexible gates: dynamic topologies and functions for FG nucleoporins in nucleocytoplasmic transport.* Eukaryotic cell, 2009. **8**(12): p. 1814-1827.
51. Hülsmann, B.B., A.A. Labokha, and D. Görlich, *The permeability of reconstituted nuclear pores provides direct evidence for the selective phase model.* Cell, 2012. **150**(4): p. 738-751.
52. Frey, S. and D. Görlich, *A saturated FG-repeat hydrogel can reproduce the permeability properties of nuclear pore complexes.* Cell, 2007. **130**(3): p. 512-523.
53. Lim, R.Y., et al., *Flexible phenylalanine-glycine nucleoporins as entropic barriers to nucleocytoplasmic transport.* Proceedings of the National Academy of Sciences, 2006. **103**(25): p. 9512-9517.
54. Yamada, J., et al., *A bimodal distribution of two distinct categories of intrinsically disordered structures with separate functions in FG nucleoporins.* Molecular & Cellular Proteomics, 2010. **9**(10): p. 2205-2224.
55. Isgro, T.A. and K. Schulten, *Binding dynamics of isolated nucleoporin repeat regions to importin-β.* Structure, 2005. **13**(12): p. 1869-1879.
56. Liu, S.M. and M. Stewart, *Structural basis for the high-affinity binding of nucleoporin Nup1p to the Saccharomyces cerevisiae importin-β homologue, Kap95p.* Journal of molecular biology, 2005. **349**(3): p. 515-525.
57. Mammen, M., S.K. Choi, and G.M. Whitesides, *Polyvalent interactions in biological systems: implications for design and use of multivalent ligands and inhibitors.* Angewandte Chemie International Edition, 1998. **37**(20): p. 2754-2794.
58. Lowe, A.R., et al., *Selectivity mechanism of the nuclear pore complex characterized by single cargo tracking.* Nature, 2010. **467**(7315): p. 600.
59. Riddick, G. and I.G. Macara, *A systems analysis of importin-α–β mediated nuclear protein import.* The Journal of cell biology, 2005. **168**(7): p. 1027-1038.
60. Lim, R.Y., et al., *Nanomechanical basis of selective gating by the nuclear pore complex.* Science, 2007. **318**(5850): p. 640-643.
61. Peters, R., *Translocation through the nuclear pore complex: selectivity and speed by reduction-of-dimensionality.* Traffic, 2005. **6**(5): p. 421-427.
62. Rout, M.P., et al., *Virtual gating and nuclear transport: the hole picture.* Trends in cell biology, 2003. **13**(12): p. 622-628.
63. Beck, M., et al., *Nuclear pore complex structure and dynamics revealed by cryoelectron tomography.* Science, 2004. **306**(5700): p. 1387-1390.
64. Akey, C.W., *Visualization of transport-related configurations of the nuclear pore transporter.* Biophysical journal, 1990. **58**(2): p. 341-355.
65. Stoffler, D., et al., *Calcium-mediated structural changes of native nuclear pore complexes monitored by time-lapse atomic force microscopy.* Journal of molecular biology, 1999. **287**(4): p. 741-752.

66. Grünwald, D., R.H. Singer, and M. Rout, *Nuclear export dynamics of RNA–protein complexes.* Nature, 2011. **475**(7356): p. 333.
67. Schleicher, K.D., et al., *Selective transport control on molecular velcro made from intrinsically disordered proteins.* Nature nanotechnology, 2014. **9**(7): p. 525.
68. Görlich, D., et al., *Identification of different roles for RanGDP and RanGTP in nuclear protein import.* 1996. **15**(20): p. 5584-5594.
69. Matsuura, Y. and M. Stewart, *Nup50/Npap60 function in nuclear protein import complex disassembly and importin recycling.* The EMBO journal, 2005. **24**(21): p. 3681-3689.
70. Nachury, M.V. and K. Weis, *The direction of transport through the nuclear pore can be inverted.* Proceedings of the National Academy of Sciences, 1999. **96**(17): p. 9622-9627.
71. Izaurralde, E., et al., *The asymmetric distribution of the constituents of the Ran system is essential for transport into and out of the nucleus.* The EMBO journal, 1997. **16**(21): p. 6535-6547.
72. Kutay, U., et al., *Export of importin α from the nucleus is mediated by a specific nuclear transport factor.* Cell, 1997. **90**(6): p. 1061-1071.
73. Matsuura, Y. and M. Stewart, *Structural basis for the assembly of a nuclear export complex.* Nature, 2004. **432**(7019): p. 872.
74. Klebe, C., et al., *Interaction of the nuclear GTP-binding protein Ran with its regulatory proteins RCC1 and RanGAP1.* Biochemistry, 1995. **34**(2): p. 639-647.
75. Bischoff, F.R. and D. Görlich, *RanBP1 is crucial for the release of RanGTP from importin β-related nuclear transport factors.* FEBS letters, 1997. **419**(2-3): p. 249-254.
76. Ribbeck, K., et al., *NTF2 mediates nuclear import of Ran.* The EMBO journal, 1998. **17**(22): p. 6587-6598.
77. Bayliss, R., et al., *Interaction between NTF2 and xFxFG-containing nucleoporins is required to mediate nuclear import of RanGDP.* Journal of molecular biology, 1999. **293**(3): p. 579-593.
78. Renault, L., et al., *Structural basis for guanine nucleotide exchange on Ran by the regulator of chromosome condensation (RCC1).* Cell, 2001. **105**(2): p. 245-255.
79. Kalab, P., K. Weis, and R. Heald, *Visualization of a Ran-GTP gradient in interphase and mitotic Xenopus egg extracts.* Science, 2002. **295**(5564): p. 2452-2456.
80. Whittaker, G.R., M. Kann, and A. Helenius, *Viral entry into the nucleus.* Annual review of cell and developmental biology, 2000. **16**(1): p. 627-651.
81. Rowe, W.P., et al., *Isolation of a cytopathogenic agent from human adenoids undergoing spontaneous degeneration in tissue culture.* Proceedings of the Society for Experimental Biology and Medicine, 1953. **84**(3): p. 570-573.

82. Escriou, V., et al., *NLS bioconjugates for targeting therapeutic genes to the nucleus.* Advanced drug delivery reviews, 2003. **55**(2): p. 295-306.
83. Trotman, L.C., et al., *Import of adenovirus DNA involves the nuclear pore complex receptor CAN/Nup214 and histone H1.* Nature cell biology, 2001. **3**(12): p. 1092.
84. Panté, N. and M.J.M.b.o.t.c. Kann, *Nuclear pore complex is able to transport macromolecules with diameters of~ 39 nm.* 2002. **13**(2): p. 425-434.
85. Goff, S.P., *Intracellular trafficking of retroviral genomes during the early phase of infection: viral exploitation of cellular pathways.* The Journal of Gene Medicine: A cross-disciplinary journal for research on the science of gene transfer and its clinical applications, 2001. **3**(6): p. 517-528.
86. Lemoine, N.R. and R. Vile, *Understanding gene therapy*. 1999: BIOS scientific publishers.
87. Panno, J., *Gene therapy: treating disease by repairing genes*. 2005: Infobase Publishing.
88. Ganta, S., et al., *A review of stimuli-responsive nanocarriers for drug and gene delivery.* Journal of controlled release, 2008. **126**(3): p. 187-204.
89. Mura, S., J. Nicolas, and P. Couvreur, *Stimuli-responsive nanocarriers for drug delivery.* Nature materials, 2013. **12**(11): p. 991.
90. Danhier, F., O. Feron, and V. Préat, *To exploit the tumor microenvironment: passive and active tumor targeting of nanocarriers for anti-cancer drug delivery.* Journal of controlled release, 2010. **148**(2): p. 135-146.
91. Lim, S.B., A. Banerjee, and H. Önyüksel, *Improvement of drug safety by the use of lipid-based nanocarriers.* Journal of controlled release, 2012. **163**(1): p. 34-45.
92. Song, W., et al., *Polypeptide-based combination of paclitaxel and cisplatin for enhanced chemotherapy efficacy and reduced side-effects.* Acta biomaterialia, 2014. **10**(3): p. 1392-1402.
93. Hillaireau, H. and P. Couvreur, *Nanocarriers' entry into the cell: relevance to drug delivery.* Cellular and molecular life sciences, 2009. **66**(17): p. 2873-2896.
94. Tammam, S.N., H.M. Azzazy, and A.J.J.o.C.R. Lamprecht, *How successful is nuclear targeting by nanocarriers?* 2016. **229**: p. 140-153.
95. Bareford, L.M. and P.W. Swaan, *Endocytic mechanisms for targeted drug delivery.* Advanced drug delivery reviews, 2007. **59**(8): p. 748-758.
96. Huotari, J. and A. Helenius, *Endosome maturation.* The EMBO journal, 2011. **30**(17): p. 3481-3500.
97. Varkouhi, A.K., et al., *Endosomal escape pathways for delivery of biologicals.* Journal of Controlled Release, 2011. **151**(3): p. 220-228.
98. Richard, I., et al., *Ionization behavior of chitosan and chitosan–DNA polyplexes indicate that chitosan has a similar capability to induce a proton-sponge effect as PEI.* Biomacromolecules, 2013. **14**(6): p. 1732-1740.

99. Kim, H.J., et al., *Introduction of stearoyl moieties into a biocompatible cationic polyaspartamide derivative, PAsp (DET), with endosomal escaping function for enhanced siRNA-mediated gene knockdown.* Journal of controlled release, 2010. **145**(2): p. 141-148.
100. Gujrati, M., et al., *Multifunctional cationic lipid-based nanoparticles facilitate endosomal escape and reduction-triggered cytosolic siRNA release.* Molecular pharmaceutics, 2014. **11**(8): p. 2734-2744.
101. Jayakumar, M.K.G., et al., *Near-infrared-light-based nano-platform boosts endosomal escape and controls gene knockdown in vivo.* ACS nano, 2014. **8**(5): p. 4848-4858.
102. Jeschke, M., et al., *Possibilities of non-viral gene transfer to improve cutaneous wound healing.* Current gene therapy, 2001. **1**(3): p. 267-278.
103. Zhang, H., A. Mitin, and S.V. Vinogradov, *Efficient transfection of blood–brain barrier endothelial cells by lipoplexes and polyplexes in the presence of nuclear targeting NLS-PEG-acridine conjugates.* Bioconjugate chemistry, 2008. **20**(1): p. 120-128.
104. Aronsohn, A. and J. Hughes, *Nuclear localization signal peptides enhance cationic liposome-mediated gene therapy.* Journal of drug targeting, 1998. **5**(3): p. 163-169.
105. Tammam, S.N., et al., *Chitosan nanoparticles for nuclear targeting: the effect of nanoparticle size and nuclear localization sequence density.* Molecular pharmaceutics, 2015. **12**(12): p. 4277-4289.
106. Anajafi, T., et al., *Nuclear localizing peptide-conjugated, redox-sensitive polymersomes for delivering curcumin and doxorubicin to pancreatic cancer microtumors.* Molecular pharmaceutics, 2017. **14**(6): p. 1916-1928.
107. Hill, J.P., et al., *Self-assembly: from amphiphiles to chromophores and beyond.* Molecules, 2014. **19**(6): p. 8589-8609.
108. Engelman, D.M., *Membranes are more mosaic than fluid.* Nature (London, U. K.), 2005. **438**(7068): p. 578-580.
109. van Meer, G., D.R. Voelker, and G.W. Feigenson, *Membrane lipids: where they are and how they behave.* Nat. Rev. Mol. Cell Biol., 2008. **9**(2): p. 112-124.
110. Tabassum, N. and A. Feroz, *Ion Channels and their Modulation.* Journal of Applied Pharmaceutical Science, 2011. **1**(1): p. 20-25.
111. Letchford, K. and H. Burt, *A review of the formation and classification of amphiphilic block copolymer nanoparticulate structures: micelles, nanospheres, nanocapsules and polymersomes.* Eur. J. Pharm. Biopharm., 2007. **65**(3): p. 259-269.
112. Klok, H.-A. and S. Lecommandoux, *Supramolecular materials via block copolymer self-assembly.* Adv. Mater. , 2001. **13**(16): p. 1217-1229.
113. Kowal, J., et al., *Planar Biomimetic Membranes Based on Amphiphilic Block Copolymers.* ACS Macro Letters, 2014. **3**(1): p. 59-63.

114. LoPresti, C., et al., *Polymersomes: nature inspired nanometer sized compartments.* Journal of Materials Chemistry, 2009. **19**(22): p. 3576-3590.
115. Gunkel-Grabole, G., et al., *Polymeric 3D nano-architectures for transport and delivery of therapeutically relevant biomacromolecules.* Biomater. Sci., 2015. **3**(1): p. 25-40.
116. Broz, P., et al., *Nano imaging technologies: polymer vesicles loaded with precipitated gadolinium nanoparticles: a novel target-specific contrast agent for magnetic resonance imaging.* European Journal of Nanomedicine, 2009. **2**(2): p. 43-48.
117. Renggli, K., et al., *Selective and Responsive Nanoreactors.* Adv. Funct. Mater., 2011. **21**(7): p. 1241-1259.
118. Dobrunz, D., et al., *Polymer nanoreactors with dual functionality: simultaneous detoxification of peroxynitrite and oxygen transport.* Langmuir, 2012. **28**(45): p. 15889-15899.
119. Axthelm, F., et al., *Antioxidant Nanoreactor Based on Superoxide Dismutase Encapsulated in Superoxide-Permeable Vesicles.* J. Phys. Chem. B, 2008. **112**(28): p. 8211-8217.
120. Baumann, P., et al., *Light-responsive polymer nanoreactors: a source of reactive oxygen species on demand.* Nanoscale, 2013. **5**(1): p. 217-224.
121. Balasubramanian, V., et al., *A surprising system: polymeric nanoreactors containing a mimic with dual-enzyme activity.* Soft Matter, 2011. **7**(12): p. 5595-5603.
122. Onaca, O., et al., *SOD Antioxidant Nanoreactors: influence of Block Copolymer Composition on the Nanoreactor Efficiency.* Macromol. Biosci., 2010. **10**(5): p. 531-538.
123. Ben-Haim, N., et al., *Cell-Specific Integration of Artificial Organelles Based on Functionalized Polymer Vesicles.* Nano Lett., 2008. **8**(5): p. 1368-1373.
124. Aranda-Espinoza, H., et al., *Electromechanical limits of polymersomes.* Physical review letters, 2001. **87**(20): p. 208301.
125. Pan, L., et al., *Nuclear-targeted drug delivery of TAT peptide-conjugated monodisperse mesoporous silica nanoparticles.* Journal of the American Chemical Society, 2012. **134**(13): p. 5722-5725.
126. Panté, N. and M. Kann, *Nuclear pore complex is able to transport macromolecules with diameters of~ 39 nm.* Molecular biology of the cell, 2002. **13**(2): p. 425-434.
127. Dominska, M. and D.M. Dykxhoorn, *Breaking down the barriers: siRNA delivery and endosome escape.* J Cell Sci, 2010. **123**(8): p. 1183-1189.
128. Torchilin, V.P., *Recent approaches to intracellular delivery of drugs and DNA and organelle targeting.* Annu. Rev. Biomed. Eng., 2006. **8**: p. 343-375.
129. Tammam, S.N., H.M. Azzazy, and A. Lamprecht, *How successful is nuclear targeting by nanocarriers?* Journal of Controlled Release, 2016. **229**: p. 140-153.

130. Petros, R.A. and J.M. DeSimone, *Strategies in the design of nanoparticles for therapeutic applications.* Nature reviews Drug discovery, 2010. **9**(8): p. 615.
131. Maity, A.R. and D. Stepensky, *Nuclear and perinuclear targeting efficiency of quantum dots depends on density of peptidic targeting residues on their surface.* Journal of Controlled Release, 2017. **257**: p. 32-39.
132. Tammam, S.N., H.M. Azzazy, and A. Lamprecht, *The effect of nanoparticle size and NLS density on nuclear targeting in cancer and normal cells; impaired nuclear import and aberrant nanoparticle intracellular trafficking in glioma.* Journal of Controlled Release, 2017. **253**: p. 30-36.
133. T. Hirt, R.C.B., D. Lohmann, and W. Meier, PCT Int. Appl, 39 pp. ((Novartis, Switzerland; Novartis-Erfindungen Verwaltungsgesellschaft) Wo, 1999), 1999.
134. Brož, P., et al., *Cell targeting by a generic receptor-targeted polymer nanocontainer platform.* Journal of Controlled Release, 2005. **102**(2): p. 475-488.
135. Duncan, R., *The dawning era of polymer therapeutics.* Nature reviews Drug discovery, 2003. **2**(5): p. 347.
136. Egli, S., et al., *Functionalization of block copolymer vesicle surfaces.* Polymers, 2011. **3**(1): p. 252-280.
137. Nardin, C., et al., *Polymerized ABA triblock copolymer vesicles.* Langmuir, 2000. **16**(3): p. 1035-1041.
138. Discher, D.E. and A. Eisenberg, *Polymer vesicles.* Science, 2002. **297**(5583): p. 967-973.
139. Nardin, C., et al., *Nanoreactors based on (polymerized) ABA-triblock copolymer vesicles.* ChemComm, 2000(15): p. 1433-1434.
140. Neubert, B.J. and B.B. Snider, *Synthesis of (±)-phloeodictine A1.* Organic letters, 2003. **5**(5): p. 765-768.
141. Gandini, A., A.J. Silvestre, and D. Coelho, *Reversible click chemistry at the service of macromolecular materials. 2. Thermoreversible polymers based on the Diels-Alder reaction of an A-B furan/maleimide monomer.* Journal of Polymer Science Part A: Polymer Chemistry, 2010. **48**(9): p. 2053-2056.
142. Neises, B. and W. Steglich, *Simple method for the esterification of carboxylic acids.* Angewandte Chemie International Edition in English, 1978. **17**(7): p. 522-524.
143. Mantovani, G., et al., *Design and synthesis of N-maleimido-functionalized hydrophilic polymers via copper-mediated living radical polymerization: a suitable alternative to PEGylation chemistry.* Journal of the American Chemical Society, 2005. **127**(9): p. 2966-2973.
144. Walde, P. and K. Morigaki, *Formation and transformation of fatty acid/soap vesicles.* Self-assembly, 2003: p. 443-453.
145. Comes, P. and W.W. Franke, *Composition, structure and function of HeLa cell nuclear envelope.* Zeitschrift für Zellforschung und Mikroskopische Anatomie, 1970. **107**(2): p. 240-248.

146. Tachibana, R., et al., *Intracellular regulation of macromolecules using pH-sensitive liposomes and nuclear localization signal: qualitative and quantitative evaluation of intracellular trafficking.* Biochemical and biophysical research communications, 1998. **251**(2): p. 538-544.
147. Itel, F., et al., *Molecular organization and dynamics in polymersome membranes: A lateral diffusion study.* Macromolecules, 2014. **47**(21): p. 7588-7596.
148. Murphy, R.M., *Static and dynamic light scattering of biological macromolecules: what can we learn?* Current opinion in biotechnology, 1997. **8**(1): p. 25-30.
149. Stauch, O., et al., *Structure of artificial cytoskeleton containing liposomes in aqueous solution studied by static and dynamic light scattering.* Biomacromolecules, 2002. **3**(3): p. 565-578.
150. Bacia, K. and P. Schwille, *Practical guidelines for dual-color fluorescence cross-correlation spectroscopy.* Nature protocols, 2007. **2**(11): p. 2842.
151. Enderlein, J. and I. Gregor, *Using fluorescence lifetime for discriminating detector afterpulsing in fluorescence-correlation spectroscopy.* Review of Scientific Instruments, 2005. **76**(3): p. 033102.
152. Petrov, E. and P. Schwille, *State of the art and novel trends in fluorescence correlation spectroscopy*, in *Standardization and quality assurance in fluorescence measurements II*. 2008, Springer. p. 145-197.
153. Love, L.C. and L. Shaver, *Time correlated single photon technique: Fluorescence lifetime measurements.* Analytical Chemistry, 1976. **48**(4): p. 364A-371a.
154. Qin, W., et al., *Photophysical properties of BODIPY-derived hydroxyaryl fluorescent pH probes in solution.* ChemPhysChem, 2005. **6**(11): p. 2343-2351.
155. Dinu, I.A., et al., *Engineered non-toxic cationic nanocarriers with photo-triggered slow-release properties.* Polymer Chemistry, 2016. **7**(20): p. 3451-3464.
156. Qiu, L.Y. and Y.H. Bae, *Self-assembled polyethylenimine-graft-poly (ε-caprolactone) micelles as potential dual carriers of genes and anticancer drugs.* Biomaterials, 2007. **28**(28): p. 4132-4142.
157. Müller, C., et al., *Precise measurement of diffusion by multi-color dual-focus fluorescence correlation spectroscopy.* EPL (Europhysics Letters), 2008. **83**(4): p. 46001.
158. Paulillo, S.M., et al., *Nucleoporin domain topology is linked to the transport status of the nuclear pore complex.* Journal of molecular biology, 2005. **351**(4): p. 784-798.
159. Schwarz-Herion, K., et al., *Domain topology of the p62 complex within the 3-D architecture of the nuclear pore complex.* Journal of molecular biology, 2007. **370**(4): p. 796-806.

160. Fahrenkrog, B., et al., *Domain-specific antibodies reveal multiple-site topology of Nup153 within the nuclear pore complex.* Journal of structural biology, 2002. **140**(1-3): p. 254-267.
161. Catimel, B., et al., *Biophysical characterization of interactions involving importin-alpha during nuclear import.* J. Biol. Chem., 2001. **276**(36): p. 34189-34198.
162. Schwille, P., J. Korlach, and W.W. Webb, *Fluorescence correlation spectroscopy with single-molecule sensitivity on cell and model membranes.* Cytometry: The Journal of the International Society for Analytical Cytology, 1999. **36**(3): p. 176-182.
163. Weiss, S., *Fluorescence spectroscopy of single biomolecules.* Science, 1999. **283**(5408): p. 1676-1683.
164. Magde, D., E. Elson, and W.W. Webb, *Thermodynamic fluctuations in a reacting system—measurement by fluorescence correlation spectroscopy.* Physical Review Letters, 1972. **29**(11): p. 705.
165. Eigen, M. and R. Rigler, *Sorting single molecules: application to diagnostics and evolutionary biotechnology.* Proceedings of the National Academy of Sciences, 1994. **91**(13): p. 5740-5747.
166. Schwille, P., F.-J. Meyer-Almes, and R. Rigler, *Dual-color fluorescence cross-correlation spectroscopy for multicomponent diffusional analysis in solution.* Biophysical journal, 1997. **72**(4): p. 1878-1886.
167. Melo, A.M., M. Prieto, and A. Coutinho, *The effect of variable liposome brightness on quantifying lipid–protein interactions using fluorescence correlation spectroscopy.* Biochimica et Biophysica Acta (BBA)-Biomembranes, 2011. **1808**(10): p. 2559-2568.
168. Rusu, L., et al., *Fluorescence correlation spectroscopy studies of peptide and protein binding to phospholipid vesicles.* Biophysical journal, 2004. **87**(2): p. 1044-1053.
169. Rigler, P. and W. Meier, *Encapsulation of fluorescent molecules by functionalized polymeric nanocontainers: investigation by confocal fluorescence imaging and fluorescence correlation spectroscopy.* Journal of the American chemical society, 2006. **128**(1): p. 367-373.
170. Najer, A., et al., *Analysis of Molecular Parameters Determining the Antimalarial Activity of Polymer-Based Nanomimics.* Macromolecular rapid communications, 2015. **36**(21): p. 1923-1928.
171. Bacia, K., S.A. Kim, and P. Schwille, *Fluorescence cross-correlation spectroscopy in living cells.* Nature methods, 2006. **3**(2): p. 83.
172. Rüttinger, S., et al., *On the resolution capabilities and limits of fluorescence lifetime correlation spectroscopy (FLCS) measurements.* Journal of fluorescence, 2010. **20**(1): p. 105-114.
173. Dertinger, T. and S. Rüttinger, *Advanced FCS: an introduction to fluorescence lifetime correlation spectroscopy and dual-focus FCS*, in *Advanced Photon Counting*. 2014, Springer. p. 89-109.

174. Lakowicz, J.R., *Principles of fluorescence spectroscopy*. 2013: Springer Science & Business Media.
175. Kruger, D., et al., *Measuring Protein Binding to Lipid Vesicles by Fluorescence Cross-Correlation Spectroscopy.* Biophysical Journal, 2017. **113**(6): p. 1311-1320.
176. Cooper, A., *Biophysical chemistry*. 2nd ed. 2011, Cambridge, United Kingdom: The Royal Society of Chemistry.
177. Kapinos, L.E., et al., *Karyopherin-centric control of nuclear pores based on molecular occupancy and kinetic analysis of multivalent binding with FG nucleoporins.* Biophysical journal, 2014. **106**(8): p. 1751-1762.
178. Kowalczyk, S.W., et al., *Single-molecule transport across an individual biomimetic nuclear pore complex.* Nature nanotechnology, 2011. **6**(7): p. 433.
179. Schoch, R.L., L.E. Kapinos, and R.Y. Lim, *Nuclear transport receptor binding avidity triggers a self-healing collapse transition in FG-nucleoporin molecular brushes.* Proceedings of the National Academy of Sciences, 2012. **109**(42): p. 16911-16916.
180. Xu, C., et al., *Monodisperse magnetite nanoparticles coupled with nuclear localization signal peptide for cell-nucleus targeting.* Chemistry–An Asian Journal, 2008. **3**(3): p. 548-552.
181. Nitin, N., et al., *Tat peptide is capable of importing large nanoparticles across nuclear membrane in digitonin permeabilized cells.* Annals of biomedical engineering, 2009. **37**(10): p. 2018-2027.
182. Grandinetti, G., A.E. Smith, and T.M. Reineke, *Membrane and nuclear permeabilization by polymeric pDNA vehicles: efficient method for gene delivery or mechanism of cytotoxicity?* Molecular pharmaceutics, 2012. **9**(3): p. 523-538.
183. Larsen, J.D., N.L. Ross, and M.O. Sullivan, *Requirements for the nuclear entry of polyplexes and nanoparticles during mitosis.* The journal of gene medicine, 2012. **14**(9-10): p. 580-589.
184. Breunig, M., S. Bauer, and A. Göpferich, *Polymers and nanoparticles: intelligent tools for intracellular targeting?* European Journal of Pharmaceutics and Biopharmaceutics, 2008. **68**(1): p. 112-128.
185. Dworetzky, S.I., R.E. Lanford, and C.M. Feldherr, *The effects of variations in the number and sequence of targeting signals on nuclear uptake.* The Journal of cell biology, 1988. **107**(4): p. 1279-1287.
186. Baumann, P., et al., *Cellular trojan horse based polymer nanoreactors with light-sensitive activity.* J. Phys. Chem. B, 2014. **118**(31): p. 9361-9370.
187. Magidson, V. and A. Khodjakov, *Circumventing photodamage in live-cell microscopy*, in *Methods in cell biology*. 2013, Elsevier. p. 545-560.
188. Musinova, Y.R., et al., *Nucleolar localization/retention signal is responsible for transient accumulation of histone H2B in the nucleolus through electrostatic interactions.* Biochimica et Biophysica Acta (BBA)-Molecular Cell Research, 2011. **1813**(1): p. 27-38.

189. Kang, B., M.A. Mackey, and M.A. El-Sayed, *Nuclear targeting of gold nanoparticles in cancer cells induces DNA damage, causing cytokinesis arrest and apoptosis.* Journal of the American Chemical Society, 2010. **132**(5): p. 1517-1519.
190. Bernhard, W., *A new staining procedure for electron microscopical cytology.* Journal of ultrastructure research, 1969. **27**(3-4): p. 250-265.
191. Bermudez, H., D.A. Hammer, and D.E. Discher, *Effect of bilayer thickness on membrane bending rigidity.* Langmuir, 2004. **20**(3): p. 540-543.
192. Görlich, D., et al., *Two different subunits of importin cooperate to recognize nuclear localization signals and bind them to the nuclear envelope.* Current Biology, 1995. **5**(4): p. 383-392.
193. Moroianu, J., G. Blobel, and A. Radu, *Previously identified protein of uncertain function is karyopherin alpha and together with karyopherin beta docks import substrate at nuclear pore complexes.* Proceedings of the National Academy of Sciences, 1995. **92**(6): p. 2008-2011.
194. Radu, A., G. Blobel, and M.S. Moore, *Identification of a protein complex that is required for nuclear protein import and mediates docking of import substrate to distinct nucleoporins.* Proceedings of the National Academy of Sciences, 1995. **92**(5): p. 1769-1773.
195. Adam, S.A., R.S. Marr, and L. Gerace, *Nuclear protein import in permeabilized mammalian cells requires soluble cytoplasmic factors.* J. Cell Biol., 1990. **111**(3): p. 807-816.
196. Cassany, A. and L. Gerace, *Reconstitution of nuclear import in permeabilized cells*, in *The Nucleus*. 2008, Springer. p. 181-205.
197. Fiskum, G., et al., *The cytoskeleton of digitonin-treated rat hepatocytes.* Proceedings of the National Academy of Sciences, 1980. **77**(6): p. 3430-3434.
198. Martin, R.M., et al., *Principles of protein targeting to the nucleolus.* Nucleus, 2015. **6**(4): p. 314-325.
199. Popken, P., et al., *Size-dependent leak of soluble and membrane proteins through the yeast nuclear pore complex.* Molecular biology of the cell, 2015. **26**(7): p. 1386-1394.
200. Bernhard, W.J.J.o.u.r., *A new staining procedure for electron microscopical cytology.* 1969. **27**(3-4): p. 250-265.
201. Catimel, B., et al., *Biophysical characterization of interactions involving importin-alpha during nuclear import.* Journal of Biological Chemistry, 2001. **276**(36): p. 34189-34198.
202. Andersson, M., B. Wittgren, and K.-G. Wahlund, *Accuracy in multiangle light scattering measurements for molar mass and radius estimations. Model calculations and experiments.* Analytical Chemistry, 2003. **75**(16): p. 4279-4291.
203. Chorvat Jr, D. and A. Chorvatova, *Multi-wavelength fluorescence lifetime spectroscopy: a new approach to the study of endogenous fluorescence in living cells and tissues.* Laser Physics Letters, 2008. **6**(3): p. 175.

6.3 List of Abbreviations

AC	Auto-correlation
BioEM	Electron microscopy of thin sectioned cells
BSA	Bovine Serum Albumine
CAS	Cellular Apoptoses Susceptibility
CC	Cross-Correlation
CPM	Counts Per Molecule
CR	Count Rate
cryo-EM	Cryogenic Electron Microscopy
DA	Diels-Alder
DCC	Dicyclohexylcarbodiimide
DCU	Dicyclohexylurea
DLS	Dynamic Light Scattering
DMAP	Dimethylaminopyridine
DNA	Deoxyribonucleic Acid
DTT	Dithiothreitol
EDTA	Ethylenediaminetetraacetic Acid
EGTA	Ethylene Glycol-bis(2-aminoethylether)-*N*,*N*,*N*'*N*'-tetraacetic Acid
ER	Endoplasmic Reticulum
EtOH	Ethanol
FBS	Fetal Bovine Serum
FCCS	Fluorescence Cross-Correlation Spectroscopy
FCS	Fluorescence Correlation Spectroscopy
FG	Phenylalanine-Glycine
FLCCS	Fluorescence Lifetime Cross-Correlation Spectroscopy
dcFLCCS	Dual-color FLCCS
FLCS	Fluorescence Lifetime Correlation Spectroscopy
FM	Fluorescence Microscopy

FMal	Furan Protected Maleimide
GDP	Guanosine Diphosphate
GLFG	Glycine-Leucine-Phenylalanine-Glycine
GPC	Gel Permeation Chromatography
GST	Glutathione-*S*-Transferase
GTP	Guanosine Triphosphate
HEAT	Helical Structure in Huntingtin, Elongation Factor 3, Protein Phosphatase 2A, and Yeast Kinase TOR1
HEPES	Hydroxyethyl-Piperazineethanesulfonic Acid
Kap	Karyopherin
IBB	Importinβ Binding Domain
IPTG	Isopropyl-*β-D*-Thiogalactopyranosid
MeOH	Methanol
MOXA	Methyloxazoline
NHS	*N*-Hydroxysuccinimide
NC	Nanocarrier
Blank NC	Non-Functionalized NC
Mal – NC	Maleimide Functionalized NC
NLS – NC	Nuclear Localization Sequence Functionalized NC
SAMSA – NC	*S*-(AcetylMercapto)Succinoyl) Amino) Fluorescein Functional NC
NCT	Nucleocytoplasmic Transport
NE	Nuclear Envelope
NES	Nuclear Export Sequence
Ni-NTA	Nickel Nitrilotriacetic Acid
NLS	Nuclear Localization Sequence
biNLS	Bipartite NLS
NMR	Nuclear Magnetic Resonance
NP	Nanoparticle
NPC	Nuclear Pore Complex

NTF2	Nuclear Transport Factor 2
NTR	Nuclear Transport Receptor
Nup	Nucleoporin
PBS	Phosphate Buffered Saline
PDI	Polydispersity Index
PDMS	Polydimethylsiloxan
PLA	Polylactic Acid
PMOXA	Polymethyloxazoline
PMSF	Phenylmethanesulfonyl Fluoride
PEG	Polyethylene Glycol
PET	Polyethylene Terephthalate
pH	Potential of Hydrogen
PIE	Pulse Interleaved Excitation
Ras	Rat sarcoma
Ran	Ras-related Nuclear Protein
RanGAP	RanGTPase Activating Protein
RanGDP	Guanosine Diphosphate On-Bound Ran Protein
RanGEF	Ran Guanine Nucleotide Exchange Factor
RanGTP	Guanosine Triphosphate On-Bound Ran Protein
RCA	Relative Correlation Amplitude
RNA	Ribonucleic Acid
rRNA	Ribosomal RNA
RNP	Ribonucleoprotein Particles
ROI	Region of Interest
ROS	Reactive Oxygen Species
RR	Ruthenium Red
SEC	Size Exclusion Chromatography
SLS	Static Light Scattering
SMF	Single Molecule Fluorescence

SNR	Signal to Noise Ratio
SPAD	Single Photon Avalanche Detector
SPR	Surface Plasmon Resonance
SREBP2	Sterol Regulatory Element-Binding Protein 2
TCSPC	Time-Correlated Single Photon Counting
TEA	Triethylamine
TEM	Transmission Electron Microscopy
TfsA	Triflic Acid Anhydride
TB	Transport Buffer
UA	Uranyl Acetate
WT	Wild Type